ALBA

Generalitat de Catalunya
Departament d'Empresa i Coneixement

GOBIERNO DE ESPAÑA
MINISTERIO DE CIENCIA, INNOVACIÓN Y UNIVERSIDADES

ALBA Synchrotron - Carrer de la Llum 2-26
08290 Cerdanyola del Vallès, Barcelona, Spain - Tel: +34 93 592 43 00 - www.albasynchrotron.es

2017 ACTIVITY REPORT ALBA

ALBA

2017
ACTIVITY REPORT

ALBA

2017

ACTIVITY REPORT

Generalitat de Catalunya
Departament d'Empresa
i Coneixement

GOBIERNO DE ESPAÑA
MINISTERIO DE CIENCIA, INNOVACIÓN Y UNIVERSIDADES

ALBA Synchrotron
Carrer de la Llum 2-26
08290 Cerdanyola del Vallès (Barcelona)
Spain
Tel. +34 93 592 4300

Editors: Salvador Ferrer and Ana Belén Martínez

We'd like to thank the contributors who have participated in this publication:
Stefano Agrestini, Marta Ávila, Ramon Barnadas, Amilcar Bedoya-Pinto, Alfonso Caballero, Joan Casas, Carles Colldelram, Ana Cuesta, Fei Du, Daniel Errandonea, Salvador Ferrer, David Fernández, Ignasi Fina, Michael Foerster, Gastón García, Miguel Ángel García-Aranda, Maria José García, Victor Garrido, Qiang Fu, Pierluigi Gargiani, Judith Juanhuix, Elena Junquera, Sergey Kapishnikov, Anna Laromaine, Paqui López Fagúndez, Arturo Martínez Arias, Josep Nicolás, Victor de la Peña, Francis Pérez, Montse Pont, Laurent Rubatat, Ángela Salom, Alejandro Sánchez, David Santamaría-Pérez, Massimo Tallarida, Dino Tonti, Núria Valls, Antoni Villaverde.

Graphic design: Lucas Wainer

Printing: JM Gràfic

By printing this document with CyclusPrint and Cocoon 60 Silk papers, it's been saved:

4,251 litres of water

385 kWh of energy

218 kg of wood

Sources : Water and energy savings are based on a comparison between a recycled paper manufactured at Arjowiggins Graphic mills versus an equivalent virgin fibre paper according to the latest European BREF data available (virgin fibre paper manufactured in a non-integrated paper mill). CO_2 emission savings is the difference between the emissions produced at an Arjowiggins Graphic mill for a specific recycled paper compared to the manufacture of an equivalent virgin fibre paper. Carbon footprint data evaluated by Labelia Conseil in accordance with the Bilan Carbone® methodology. Results are obtained according to technical information and subject to modification.

CONTENTS

FOREWORD

Dear reader,

In this foreword I have the challenging task of summarizing in few lines a year of activity at our facility. Let me just highlight few facts.

For the first time we have been operating eight beamlines during the whole calendar year. The availability of the accelerator systems, which has set another annual record, up to 98.3%, together with the beamline optimization and evolution, which allow to carry on experiments using shorter times, has increased the total number of researcher visits well over 1700, including a significant increase of our industrial customers.

We have set another step in the growth of the facility, the starting of the construction of a new beamline, NOTOS. NOTOS is one of the Phase III beamlines, originally meant for instrument development. It has been decided to enlarge its scope by adding Powder Diffraction and EXAFS capabilities thanks to the collaboration of the Spanish CRG beamline at the European Synchrotron Radiation Facility (ESRF). The availability of this instrumentation, that will be dismissed after the ESRF upgrade, will highly improve the performance of NOTOS. The beamline design has been reviewed during this year, and the plan to host the first users in 2020.

ALBA Synchrotron, as one of the components of the Spanish unique scientific and technical infrastructures (ICTS) map, is periodically presenting to the stakeholders a four-year Strategy Plan. During this year we were requested to submit the one which spans from 2017 to 2020. The document consists of two phases: one regarding the overview of the facility activities and results during the previous period, 2013-2016, submitted in October 2017; the second phase, to be prepared once the first is positively evaluated, and submitted during 2018. In this plan we present the priority strategic lines, which set the growth of the facility in terms of new beamlines, within the economic boundaries approved by the stakeholders, together with our plans for increasing innovation capacities, for a stronger internationalization, for a continuous engagement in terms of training and outreach activities.

And when mentioning internationalization, I want to highlight the results of the association during 2017 of the Iranian Light Source Facility. ILSF researchers were visiting our beamlines carrying out up to 10 experiments, thanks to a special call dedicated to the Iranian institutions, to which more than 50 proposals were submitted.

Maintaining the high attention to all safety aspects in our facility, ALBA's new Prevention Plan procedure has been approved, better adapted to the simultaneous activities of operation and new beamlines construction.

Finally, the involvement in the LEAPS Association, from its foundation and first shaping of its strategy and vision, has been an enriching exercise of communication and opening to the world, which I'm sure will fruitfully improve ALBA capacities in serving the society.

Wishing you a pleasant reading,

Caterina Biscari
Director

THE ALBA SYNCHROTRON

ALBA is the Spanish 3rd generation synchrotron light source, located in Cerdanyola del Vallès, near Barcelona, and constitutes the largest scientific infrastructure in the country. The facility consists of the accelerator systems providing a 3 GeV electron beam and several experimental beamlines, with photon energies currently ranging from infrared up to hard X-rays of tens of keV. Different synchrotron radiation techniques are available including diffraction, spectroscopies and imaging.

The ALBA project was approved in 2003 and funded in equal parts by the Spanish and Catalan governments. It is managed by CELLS (Consortium for the Construction, Equipment and Exploitation of the Synchrotron Light Source).

ALBA was built on a green field next to the Universitat Autònoma de Barcelona and several research centres in the Bellaterra campus. The construction began in 2006, after a few years dedicated to its design and to the training of a new team of experts, coming from Spain and abroad. The building and the services were ready by 2009, when the accelerator installation started. The whole accelerator was ready and commissioned by 2011, and the seven first beamlines were installed and commissioned in 2011-12. First official users were hosted in 2012, and in February 2013 all the Phase I beamlines were operational. In October 2016 the first Phase II beamline, MIRAS, hosted the first academic users.

The accelerators

The accelerator system consists of a linear accelerator (linac) - where electrons reach 100 MeV-, a low-emittance, full-energy booster - where electrons are accelerated to 3GeV-, and the storage ring - where electrons are injected in top-up operation mode-. The booster (250 m of circumference) and the storage ring (269 m) are both hosted in the same tunnel. The lattice is optimized for low emittance with high photon flux density, with a nominal current of 250 mA. There is a large number of straight sections (24) available, despite the relatively short circumference, thanks to the very compact lattice design, which incorporates quadrupolar field component in the dipoles.

The vacuum chamber has up to 34 windows for light extraction. Thirteen of them are presently used (2 for accelerator diagnostics, 8 for operational beamlines and 3 for beamlines under construction), and the others witness to the large potentiality of ALBA for the future.

The beamlines

ALBA currently has eight beamlines dedicated to different scientific fields, mainly physics, chemistry, life sciences, materials science, cultural heritage, biology and nanotechnology. Four of the current beamlines have two experimental endstations. Three additional beamlines are in construction and one more under design.

PORT	BEAMLINE	ENDSTATIONS	EXPERIMENTAL TECHNIQUES	SCIENTIFIC APPLICATIONS
1	MIRAS	1	Infrared microspectroscopy	Life sciences, food sciences, materials science, cultural heritage
4	MSPD	2	High-resolution powder diffraction Microdiffraction including high pressure	Structure of materials Time resolved diffraction Quantitative phase analysis
9	MISTRAL	1	Soft X-ray full-field transmission X-ray microscope. Optimized on the 'water window'	Cryogenic tomography of biological objects Spatially resolved spectroscopy
11	NCD	1	High-resolution small and high-angle X-ray scattering/diffraction	Structure and phase transformations of biological fibres, polymers, solutions Time resolved X-ray studies
13	XALOC	1	X-ray diffraction from crystals of biological macromolecules	Macromolecular crystallography, with particular emphasis on large unit cell crystals
22	CLÆSS	2	EXAFS, XANES, Quick-EXAFS, XES	Materials science, catalysis, environmental sciences, electronic structures
24	CIRCE	2	Photoemission microscopy (PEEM) Near-atmospheric-pressure photo-emission (NAPP)	Nano-science and magnetic domain imaging (PEEM) Surface chemistry (NAPP)
29	BOREAS	2	Circular magnetic dichroism Resonant magnetic diffraction	Magnetism, surface magnetism and magnetic structures
20	LOREA	1	Angle-resolved photoemission spectroscopy	Advanced materials, band structure determination
6	XAIRA	1	Microfocus beamline for macromolecular crystallography	Macromolecular crystallography, with particular emphasis on small unit cell crystals
16	NOTOS	2	X-ray absorption and powder diffraction Metrology and instrumentation development	Materials science Chemistry Instrumentation Metrology

ALBA IN BRIEF…

- User operations started in 2012
- 3 GeV 150 mA Top-Up operations with a current variation lower than 1%
- 5900h of operation with 4650h user time - 98% availability
- 21 M€ operation budget in 2017
- Proposals have increased from about 200 in 2012 to almost 400 in 2017. Average overboooking factor: 2
- User affiliation: 65% national, 30% European, 5% non-European
- Eight beamlines in operation, three under construction, one under design and three pending approval

- **serves a large community of users:** about 6000 researcher visits and 1000 experiments have been recorded to date
- **has contributed to the rapid increase in the Spanish synchrotron light user community** by one order of magnitude following the project's approval, **while attracting competitive international users**, which today account for more than one third of the total; **generates an ever-increasing output of scientific publications**, with a high average impact factor (18% of publications with IF>7)
- guides the **development of the industrial user community**
- provides an **effective outreach program** towards society with more than 7000 visitors per year
- has established **a student training program** for university and dual vocational training students
- contributes to **fostering high technology companies**
- serves as **one of the nodes of the international network of photon sources** and maintains fruitful collaborations with other Spanish research facilities

2017 SCIENTIFIC ADVISORY COMMITTEE

The ALBA Scientific Advisory Committee (SAC) is a board of internationally renowned experts in the field of synchrotron radiation, which participates in the strategic scientific management of the ALBA Synchrotron with the aim of ensuring the quality and relevance of the research developed at ALBA. The 24th meeting of the SAC was held on the 3rd and 4th July 2017. The 25th meeting of the SAC was held on the 14th and 15th December 2017. These were its members in the last meeting:

IAN ROBINSON, CHAIR

Full professor at the London Centre for Nanotechnology

WIM BRAS

Project leader of DUBBLE CRG-BL at the European Synchrotron Radiation Facility (ESRF)

ANDREAS JANKOWIAK

Director of the Institute of Accelerator Physics at the Helmholtz Zentrum Berlin

VALERIE BRIOIS

ROCK beamline responsible at Soleil Synchrotron

MARTÍN MARTÍNEZ RIPOLL

Research Professor at the Institute of Physical Chemistry "Rocasolano", Department of Crystallography

PEDRO FERNANDES-TAVARES

Project Leader for the Storage Rings at Max-IV Laboratory, Lund (Sweden)

AMINA TALEB-IBRAHIMI

Director for Matter Sciences at Soleil Synchrotron, Gif-sur-Yvette (France)

MARCO STAMPANONI

Paul Scherrer Institut & Swiss Federal Institute of Technology Zürich

OLIVER SEECK

Group leader of the "PETRA III experiments" group at DESY in Hamburg

TRINITAT PRADELL

Full professor at the Polytechnic University of Catalonia, Department of Physics and Nuclear Engineering

2017 GOVERNING BODIES

The Governing Council of the ALBA Synchrotron is the main decision-making body and usually meets twice a year. Its responsibilities are to ensure and supervise the performance of the ALBA Synchrotron. The Governing Council delegates powers to the Executive Commission for managing the human and financial resources of the facility. The composition of the governance during 2017 follows.

GOVERNING COUNCIL	
Chairperson	**CARMEN VELA OLMO** Secretary of State for Research, Development and Innovation. MINECO
Vice Chairperson	**JORDI BAIGET I CANTONS** (January-June 2017) **SANTI VILA I VICENTE** (July-October 2017) Minister of Business and Knowledge (Government of Catalonia)
Members	**JUAN MARÍA VÁZQUEZ ROJAS** Secretary-General for Science and Innovation. MINECO **JOSÉ IGNACIO DONCEL MORALES** Undersecretary-General for Large Scientific and Technical Facilities. MINECO **EMILIO LORA-TAMAYO D'OCÓN** President of the National Research Councill (CSIC) **ARCADI NAVARRO I CUARTIELLAS** Secretary for Universities and Research.Government of Catalonia **FRANCESC RAMON SUBIRADA CURCÓ** Director-General for Research. Government of Catalonia **MARGARITA ARBOIX ARZO** Rector of the Autonomous University of Barcelona (UAB)
Secretary	**MARTA JÁUREGUI GÓMEZ** State Lawyer
Vice Secretary	**XAVIER URIÓS I APARISI** Lawyer of the Government of Catalonia
Guests	**CATERINA BISCARI** Director of the CELLS

EXECUTIVE COMMISSION	
Chairperson	**ARCADI NAVARRO I CUARTIELLAS** Secretary for Universities and Research.Government of Catalonia
Vice Chairperson	**JUAN MARÍA VÁZQUEZ ROJAS** Secretary-General of Science and Innovation. MINECO
Members	**JOSÉ IGNACIO DONCEL MORALES** Undersecretary-General for Large Scientific and Technical Facilities. MINECO **FRANCESC RAMON SUBIRADA CURCÓ** Director-General for Research. Government of Catalonia
Secretary	**BERTA BERNAD SORJÚS** Lawyer of the Government of Catalonia
Vice Secretary	**MARTA JÁUREGUI GÓMEZ** State Lawyer
Guests	**CATERINA BISCARI** Director of the CELLS

ALBA STRATEGIC PLAN

During 2017 ALBA, together will all other Spanish unique scientific and technical infrastructures (ICTS) has been involved in the process of elaborating a strategic plan. ALBA prepared and got positively evaluated two strategic plans previous to this one, for the periods 2010-14 and 2013-16 respectively. The next one applies to the period 2017-20. The first part of the plan, focused on the reporting about the results from the previous period (2013-16) in terms of performance and achievements, was formally presented in October 2017. Once it is evaluated, the second part, in this case focused on the plans for the period 2017-20 shall be formally presented for evaluation by external experts and eventual approval already during 2018.

The strategic plan follows a standard structure for all ICTS facilities and it contains the key directions to be followed as well as plans for investment, with emphasis on prioritization. Keeping at a top priority the full exploitation of the existing infrastructures with highly demanding performance standards, the plan also includes a vigorous investment program for new beamlines, essential to profit the opportunities that ALBA offers to the scientific and industrial communities with its capacity, still not fully used. Continuous evolution of the existing beamlines and complementary utilities, such as data management capabilities are fully considered. Last but not least, the plan contemplates exploring and actively promoting synergetic actions with the surrounding scientific environment, such as the possibility of locating at ALBA an advanced electron microscopy center in collaboration with other institutions and the elaboration of a study for a future upgrade to the ALBA storage ring lattice, aimed at a future stage of the facility operative lifecycle.

PART OF THE LEAGUE OF EUROPEAN ACCELERATOR-BASED PHOTON SOURCES (LEAPS).

The ALBA Synchrotron is one of the 16 organisations representing 19 light sources facilities across Europe that form the LEAPS initiative. LEAPS is an unprecedented scientific collaboration that aims to offer a step change in European cooperation, through a common vision of enabling scientific excellence solving global challenges, and boosting European competitiveness and integration. This will be achieved through a common sustainable strategy developed in coordination with all stakeholders, including national policy makers, user communities and the European Commission.

LEAPS, chaired by Helmut Dosch (DESY) and vice-chaired by Caterina Biscari (ALBA), was officially launched in Brussels on November 2017 in the presence of Robert-Jan Smits, Director General for Research and Innovation (RTD) at the European Commission, and Giorgio Rossi, Chair of the European Strategy Forum on Research Infrastructures (ESFRI), as well as other national political representatives.

Several actions are planned in the coming years within the LEAPS collaboration to meet the objectives of the initiative.

www.leaps-initiative.eu

LEAPS brochure: https://www.leaps-initiative.eu/news/leaps_brochure/

Launching event in Brussels for presenting the LEAPS Initiave.

Directors of the facilities that signed the collaboration agreement of LEAPS.

BEAMLINES IN CONSTRUCTION

Massimo Tallarida, Judith Juanhuix
ALBA Synchrotron

LOREA

In 2017 the insertion device has been installed inside the tunnel. The insertion device, an undulator with a period of 125 mm, will deliver the synchrotron light for LOREA in the energy range of 10-1000 eV with full polarization control.

Another important step for LOREA was the installation, also inside the tunnel, of the front end. Here the synchrotron light goes through acceptance slits before being delivered inside the experimental hall, to absorb the radiation that will not be used by the beamline.

The optical hutch, which will host the first mirror (M1) of the beamline, has been installed in the experimental hall. The intense radiation that will impinge on the M1 mirror will generate scattered and Compton radiation that has to be shielded with an optical hutch with highly absorbing metallic walls.

On the beamline side, the optical part has been definitively released with a change in the orientation of one focusing mirror (the vertical focusing mirror, VFM), now pointing down in order to decrease the final height of the beam at the sample position.

The main optical and mechanical parts of the beamline (the so-called "backbone") have been chosen, and are being purchased (in 2018). The monochromator, also part of the backbone, will be instead developed as an in-house project, and is proceeding within the schedule.

The end-station, the system where the experiment will take place, is on the way to be purchased, as well.

XAIRA

The construction of the future XAIRA microfocus beamline fulfills a long-standing request from the scientific community, and is currently one of the major investments at ALBA. XAIRA aims at providing a stable, high-flux X-ray beam with a micrometric size and a wavelength of around 1 Å (12 keV photon energy) to perform macromolecular crystallography (MX) experiments and resolve the structure of the macromolecules involved in any relevant biological function at near-atomic resolution. The scientific case of XAIRA focuses on projects in which the macromolecular crystals only grow in micrometric sizes, possess a reduced diffracting power or require complex data collection strategies.

The XAIRA beamline is also intended to cope with native phasing methods, which allow resolving the structures of macromolecules by exploiting the anomalous scattering of light elements, like S, naturally occurring in macromolecular crystals. To this aim, the beamline is also capable of reaching 3 Å photon wavelength (4 keV photon energy), for which the anomalous signal from micron-sized crystals is optimal.

The new beamline will complement the existing XALOC MX beamline, which was conceived to tackle a broader, general range of crystallographic cases. The XAIRA beamline instruments close to the storage ring are currently being manufactured. The beamline optics is designed and being specified for procurement and the design of the end-station and the sample environment has already started.

UNIÓN EUROPEA
Fondo Europeo
de Desarrollo Regional
"Una manera de hacer Europa"

BL06-XAIRA is co-funded by the European Regional Development Fund (ERDF) within the Framework of the Smart Growth Operative Programme 2014-2020.

The NOTOS beamline at ALBA

G. García, J. Nicolas, S. Ferrer, M. A. G. Aranda
ALBA synchrotron

Approved in 2017, NOTOS is the 11th beamline of ALBA. Currently in the design phase and rapidly moving into construction, it aims at complementing the already outstanding capabilities of ALBA with X-ray diffraction and absorption techniques, while providing an additional tool for instrumentation development and testing, in collaboration with external institutions. Strongly coordinated with the Spanish strategy for photon-based science, NOTOS will profit from the reorganization of the Spanish beamline at the ESRF SpLine, which after the machine upgrade EBS, will keep just one branch at ESRF. BM25A will be merged with the NOTOS project. A very aggressive schedule has been elaborated, targeting to have users at this new beamline already in the spring of 2020.

NOTOS in context

NOTOS is the second phase-3 beamline approved at ALBA. After the construction of ALBA with a set of seven user beamlines (the so-called phase-1), and the approval of two more (the so-called phase-2, one of them presently in operation, whereas the second one, LOREA, is under construction), the expansion of ALBA has been planned systematically for the upcoming years in a phase-3 program, involving several new beamlines. After the approval of XAIRA, a microfocus protein crystallography instrument aimed at enabling ALBA to face cutting-edge scientific challenges in the field of Structural Biology, as already mentioned, NOTOS comes up as a newly approved beamline and will therefore be the 11th beamline of ALBA. It will provide and will provide academic and industry users with tools complementary to the ones already available, optimizing the investment and the exploitation of the facility's capacity, which allows hosting more than 20 beamlines.

Main design features and fields of application of the beamline

NOTOS will be devoted to X-ray absorption and diffraction techniques, with applications in fields such as Chemistry, Catalysis and Materials Science. ALBA already has two beamlines specialized in these techniques: CLÆSS (X-ray absorption/emission) and MSPD (powder diffraction at high resolution or under high-pressure conditions). NOTOS will help accommodate the high oversubscription present in these techniques in a cost-effective way. Additionally, it will have a particularity that is not common: the samples and their environments will have a single location at the beamline that will allow to perform XAS sequentially and diffraction experiments under the same environmental conditions. This is a feature with important scientific consequences since it will allow a close correlation between both XAS and diffraction in the very same experimental conditions as gas environment and temperature.

In addition to this, a fraction of 20-30% of NOTOS beamtime is planned to be devoted to X-ray metrology and industrial development and innovation through targeted collaborations. The beamline will incorporate very flexible tools in order to test and improve optical components requiring high-precision mechanics, X-ray detectors or other types of advanced instrumentation. The beamline is therefore intended to become a key player for technology transfer, ideal for feasibility studies or proof-of-concept projects in collaboration with science-driven industry. This beamline, when operative, could also host technological developments related to the LEAPS European strategy.

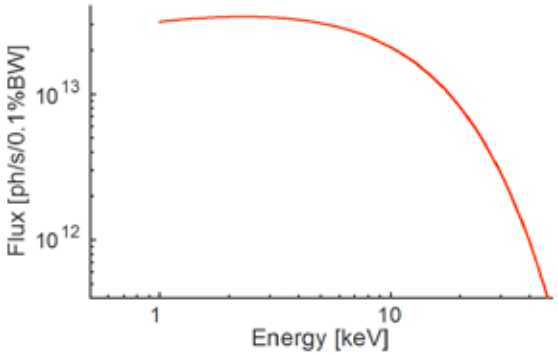

Figure 1: Flux emitted by the ALBA bending magnet, considering a current of 250 mA, and a horizontal acceptance of 2 mrad.

In order to best exploit synergies, the Spanish Ministry of Economy, Industry and Competitiveness (MINECO) decided to transfer one of the branches presently operating at BM25, the Spanish beamline at the ESRF, to ALBA. The BM25A branch is actually performing absorption/powder diffraction experiments and will serve as a basis to incorporate these techniques to NOTOS. The other branch, BM25B, will stay at the ESRF.

Photons for NOTOS will be generated by a bending magnet of the ALBA storage ring, providing spectrum and flux well adapted to the scientific case of the beamline, as shown in Fig. 1. The optics layout will be very similar to the one presently existing at BM25, involving a double crystal monochromator and X-ray mirrors among other elements. Downstream of the monochromator, two different endstations will be built: first, an endstation devoted to metrology and instrument testing and development, wherein the beam will be focused to within 90 x 90 μm^2 (see Figure 2). The second endstation, combining absorption and powder diffraction techniques, will be located four meters downstream from the previous one and it will incorporate proper sample environment and detectors.

The photon energy range intended at the present design stage is 4-30 keV.

Schedule and outlook

NOTOS is undergoing intensive design effort by ALBA staff, in close coordination with our colleagues at BM25. The integration of instruments coming from a previously existing beamline is indeed a challenge, which will be solved successfully through an intensive collaboration of both parties involved. Components which need to be manufactured anew, such as the front end, have entered the procurement phase at the end of 2017. The appropriate equipment will be transferred from BM25A to ALBA by the end of 2018, once the long ESRF upgrade shutdown starts. Then, integration and installation should proceed during 2019, followed by commissioning and receiving the first users within the first half of 2020. The schedule is really tight, but we believe it can be fulfilled. A challenging project, as the Souther wind Νότος used to be (and still is today) for sailors heading to a safe and successful harbor illuminated by (synchrotron) light.

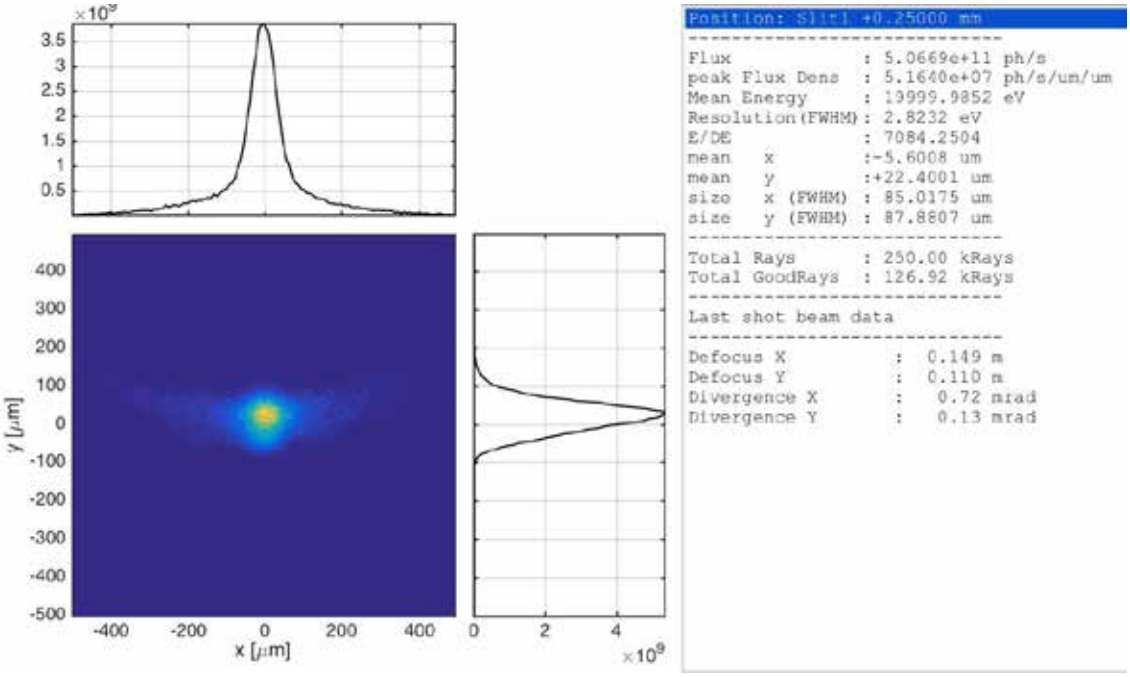

Figure 2: Simulated beam profile at the metrology endstation, where beam dimensions are calculated to be 85x88 μm^2 FWHM. At the position of the XAS/powder diffraction station the dimensions will be in the mm range along the horizontal direction and close to 300 μm in the vertical one.

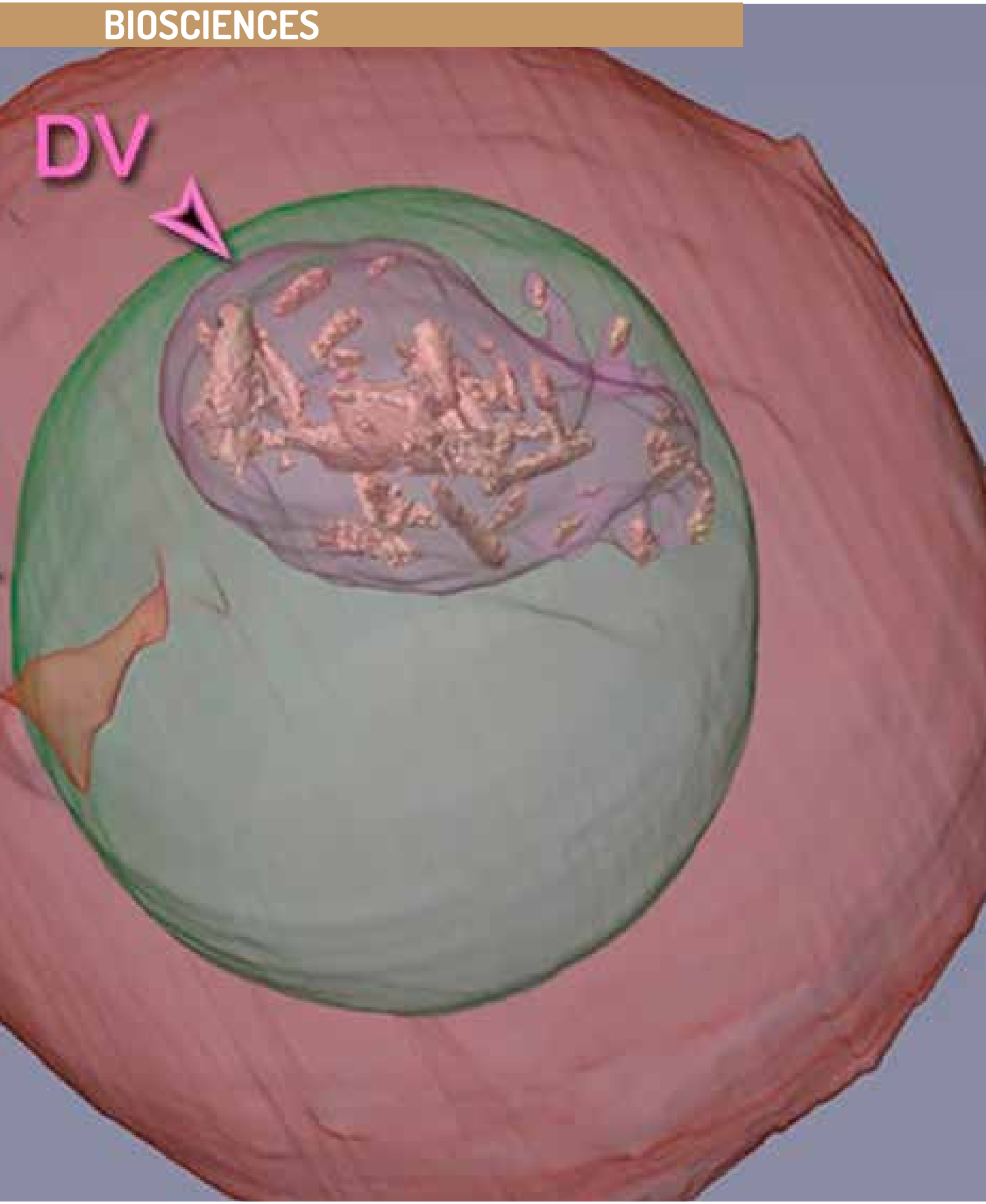

Courtesy of Sergey Kapishnikov.

Correlative soft X-ray cryo tomography and X-ray fluorescence microscopy reveal the process of heme detoxification in malaria parasites

Unraveling heme detoxification in the malaria parasite by *in-situ* correlative X-ray fluorescence microscopy and soft X-ray tomography *Scientific Reports* 7, 7610 (2017)

Biochemistry of malaria parasite infected red blood cells by X-ray microscopy *Scientific Reports* 7, 802 (2017)

Sergey Kapishnikov*[1], Eva Pereiro[2], Daniel Grolimund[3], Yang Yang[4], Peter Cloetens[4], Florence Awamu Ndonglack[5], Kai Matuschewski[5], James G. McNally[6], Gerd Schneider[6,7], Leslie Leiserowitz[8], Jens Als-Nielsen[1]

A combination of soft X-ray cryo-tomography and X-ray fluorescence was developed to study the process of heme crystallization in the malaria parasite *Plasmodium falciparum*.

Emerging resistance of malaria parasites to current drug treatments highlights the importance of developing new or improving current drug treatments [1]. After invading human red blood cells the parasites consume hemoglobin in order to grow and multiply. Large quantities of heme are released in the process of hemoglobin degradation which takes place in the parasitic digestive vacuole. Heme is highly reactive due to its iron atom and is toxic to the parasite. The parasite detoxifies heme by turning it into inert hemozoin crystals. Hemozoin crystallization is central to the parasite survival and as such it is an attractive antimalarial target. How hemozoin crystals form *in-vivo* is presently unclear, however existing models predict different crystallization rates. The aim of this work was to investigate the mechanism of hemozoin formation *in-vivo* with the aim of identifying promising drug targets.

In order to measure the *in-vivo* rate of heme crystallization, authors have developed a correlative X-ray microscopy approach that involves soft X-ray cryo-tomography (SXT) and X-ray fluorescence cryo-microscopy (XF). This combination of microscopy tools enables quantitative measurement of chemical element distribution and concentration in different cellular compartments relative to the three-dimensional cellular structure in *quasi-in-vivo* state achieved by rapid freezing.

Red blood cells infected with the malaria parasite (iRBC) were vitrified by high pressure freezing and maintained under cryogenic conditions through all experimental stages. The vitrified samples were not subject to chemical fixation, staining, embedding or sectioning. Due to significant endurance of cryogenic samples to X-ray radiation, the vitrified cells scanned by two or more high resolution X-ray microscopy tools did not exhibit any noticeable beam damage.

Three-dimensional (3D) maps of cellular structure of iRBCs were obtained by SXT at MISTRAL, ALBA and at U41-TXM, BESSY-II. The positions of the mapped cells on the sample grids were marked on large overview scans done with a built-in light microscope (see Figure 3 A) followed by multiple X-ray transmission projections arranged in mosaics covering large areas of the grid (Figure 3 B). This enabled quick location of the same cells during XF scans.

Two-dimensional (2D) maps of chemical element distribution within the same cells were first collected at microXAS, SLS [2]. Following the establishment of a cryogenic sample environment at ID16A, ESRF, maps of element distributions within iRBC were recorded at 30-50 nm resolutions[3]. The iron fluorescence signal measured at microXAS was converted into the absolute number of iron atoms using the amount of 1.08×10^9 iron atoms in a red blood cell arising from a very consistent number of hemoglobin molecules found in a human red blood cell[2]. X-ray fluorescence maps obtained at ID16A were converted into absolute numbers of elements by a rigorous analysis of the detected signal and the experimental setup as described in [3].

Two-dimensional maps of chemical elements were converted into concentrations within specific cellular compartments by combining 3D volumetric information of the cellular structure, starting from the outermost compartments down to the inner ones, as described in detail in [2,3]. This approach decoupled fluorescence signals arriving from overlapping cellular compartments. Mutual alignment of X-ray absorption tomograms and X-ray fluorescence maps was required for this analysis. Rough alignment was done by matching orientation of the sample holder grids imaged by light microscopes built into SXT (Figure 3 A) and XF (Figure 3 D) beamlines. Fine alignment was done by registering and aligning distinct features in iRBCs, such as hemozoin-packed digestive vacuoles, DV (see Figure 3 C,E,F).

The quantity of iron measured by XF in hemozoin crystals at different life stages of the malaria parasite corresponded to an approximate crystal growth rate of 10000 heme monomers per second. This rate closely matches the *in-vitro* rate of hemozoin formation by a protein known as heme detoxification protein[4]. Considerable amounts of non-crystalline heme in the digestive vacuole were also found. Analysis of 510-520 eV X-ray absorption coefficients in the digestive vacuole suggests that this non-crystalline heme is likely contained in a large amount of hemoglobin taken by the parasite but not yet digested.

The rate of hemozoin crystallization together with the large amount of hemoglobin found in the digestive vacuole led us to propose an assembly line model for heme detoxification in the parasitic digestive vacuole: heme monomers liberated from hemoglobin are dimerized via the heme detoxification protein (HDP) and the dimers crystallize into hemozoin. According to this model, the rates of heme monomer release, heme dimerization and hemozoin formation must closely match, suggesting the existence of a feedback mechanism between hemoglobin digestion and heme dimerization.

Thus, three targets for drug development become apparent: inhibition of HDP, a subject of ongoing studies, inhibition of hemozoin crystallization, which would slow heme detoxification, and inhibition of the feedback mechanism, which would result in an uncontrolled release of heme from the hemoglobin ingested by the parasite, causing damage to the parasite.

In conclusion, our correlative X-ray cryo-microscopy method establishes a new approach for the measurement of element-specific concentrations within intact cellular ultrastructure at high spatial resolutions of ~50 nm or better. This, in turn, provides a *quasi-in-vivo* platform for investigation of heme metabolism and potential antimalarial drug targets in *Plasmodium falciparum.*

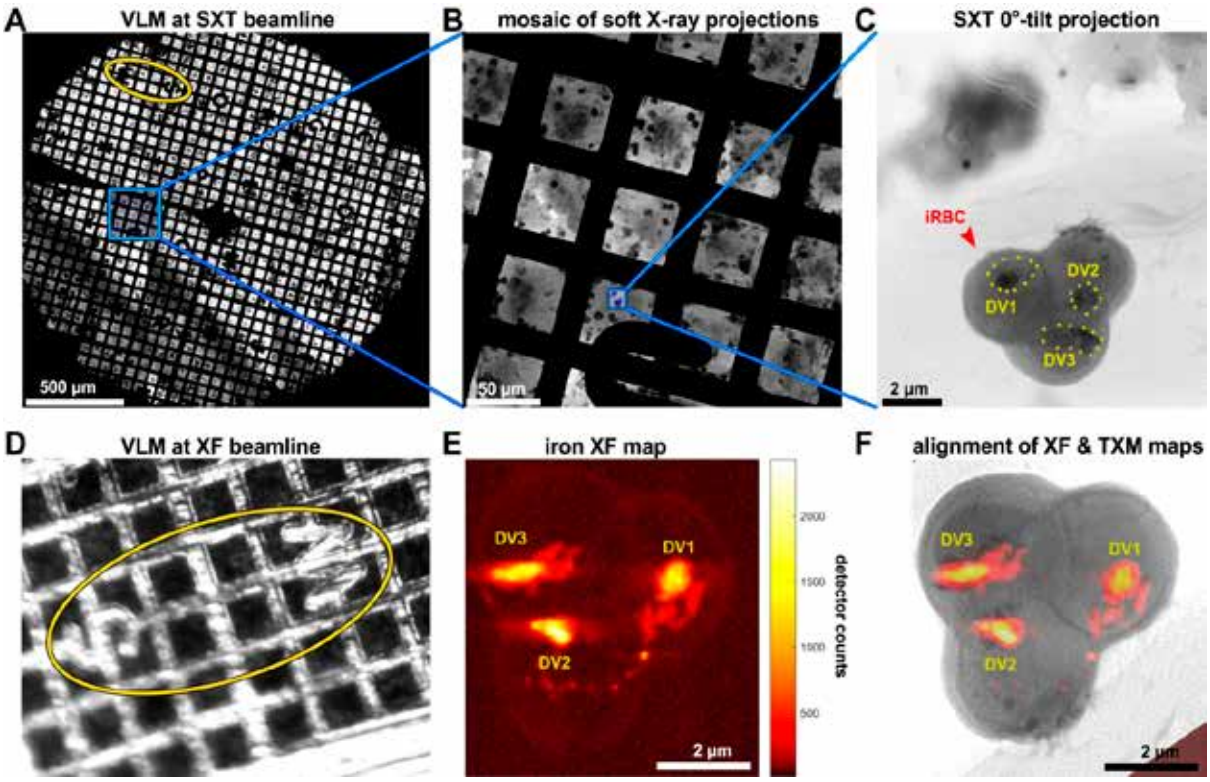

Figure 3: Correlative soft X-ray cryo tomography (SXT) and X-ray fluorescence (XF) of a *Plasmodium falciparum* infected red blood cell (iRBC). (A) Sample grid orientation captured by a light microscope (VLM) image built into the SXT setup at the MISTRAL beamline, ALBA. (B) 20×20 mosaic of soft X-ray projections covering the grid area of ~250×250 µm^2. (C) Red blood cell infected with three malaria parasites, each with a hemozoin-packed digestive vacuole labelled DV1-3. (D) VLM image of the grid orientation at ID16A beamline at ESRF, used for rough alignment. (E) Iron X-ray fluorescence (XF) map of the same iRBC (F) Mutual alignment of SXT and iron XF maps.

ACKNOWLEDGEMENTS

This work was supported by the Carlsberg Foundation grant CF15-0644, EMBO Long-Term Fellowship ALTF 461-2013, BiostructX and DanScatt.

OTHER REFERENCES

1. Antony, H. A. & Parija, S. C. Antimalarial drug resistance: An overview. *Tropical parasitology* **6**, 30-41 (2016).

2. Kapishnikov, S., Grolimund, D., Schneider, G., Pereiro, E., McNally, J. G., Als-Nielsen, J. & Leiserowitz, L. Unraveling heme detoxification in the malaria parasite by *in situ* correlative X-ray fluorescence microscopy and soft X-ray tomography. *Scientific Reports* **7**, 7610 (2017).

3. Kapishnikov, S., Leiserowitz, L., Yang, Y., Cloetens, P., Pereiro, E., Awamu Ndonglack, F., Matuschewski, K. & Als-Nielsen, J. Biochemistry of malaria parasite infected red blood cells by X-ray microscopy. *Scientific Reports* **7**, 802 (2017).

4. Jani, D., Nagarkatti, R., Beatty, W., Angel, R., Slebodnick, C., Andersen, J., Kumar, S. & Rathore, D. HDP—A Novel Heme Detoxification Protein from the Malaria Parasite. *PLoS Pathog.* **4**, e1000053 (2008).

AFFILIATION:

1. Niels Bohr Institute, University of Copenhagen, Universitetsparken 5, DK-2100, Copenhagen Ø, Denmark.
2. ALBA Synchrotron, 08290, Cerdanyola del Valles, Barcelona, Spain.
3. Paul Scherrer Institute, 5232, Villigen, PSI, Switzerland.
4. European Synchrotron Radiation Facility (ESRF), 71 avenue des Martyrs, 38000, Grenoble, France.
5. Molecular Parasitology, Institute of Biology, Humboldt University, Philippstr. 13, 10115, Berlin, Germany.
6. Soft Matter and Functional Materials, Helmholtz-Zentrum Berlin, Albert-Einstein-Str. 15, 12489, Berlin, Germany.
7. Institute of Physics, Humboldt University, Newton str. 15, 12489, Berlin.
8. Department of Materials and Interfaces, Weizmann Institute of Science, Rehovot, 76100, Israel.

Functional and architectonic heterogeneity of protein-only recombinant nanoparticles

Intrinsic functional and architectonic heterogeneity of tumor-targeted protein nanoparticles. *Nanoscale*, 9, 6427-6435 (2017)

Mireia Pesarrodona [1,2,3], Eva Crosas [4], Rafael Cubarsi [5], Alejandro Sánchez-Chardi [6], Paolo Saccardo [1,2,3], Ugutz Unzueta [3,7], Fabian Rueda [1,2,3], Laura Sanchez-García [1,2,3], Naroa Serna [1,2,3], Ramón Mangues [3,7], Neus Ferrer-Miralles [1,2,3], Esther Vázquez [1,2,3], Antonio Villaverde [*,1,2,3]

This study explores the architecture and function of protein-only recombinant nanoparticles by a diversity of analytic approaches, including SAXS, showing a spectrum of structural and functional variants with promising properties as drug delivery systems.

Self-assembling proteins produced in microbial cells are of increasing interest as building blocks of nanoscale biomaterials useful for diverse applications in biomedicine [1-13]. This is essentially because of their biocompatibility, lack of intrinsic toxicity and biodegradability, in addition to a green and scalable biological fabrication. Also, the protein functions can be tailored by simple genetic engineering and conventional methods from applied microbiology. A diversity of analytic approaches, particularly field-emission scanning electron microscopy (FESEM) and small-angle X-ray scattering (SAXS) have been applied to evaluate how the biological production might influence the structure, geometry and biological activities of recombinant, tumor-targeted protein nanoparticles based on GFP. These promising materials of study have been developed through a single platform based on the application of architectonic peptide tags to induce the self-assembly of multifunctional protein building blocks into nanoparticles. Indeed, the recombinant production of these materials results in a spectrum of conformational and functional variants of protein oligomers, with relative proportions determined by features of the producing strain. Some of these subpopulations show optimal properties regarding the use and performance of the material as a nanoscale drug delivery system.

Two *de novo* designed self-assembling protein nanoparticles, namely A5G27-GFP-H6 [14] and T22-GFP-H6 [15], produced by different E. coli strains, were explored by dynamic light scattering (DLS), upon immobilized metal affinity chromatography (IMAC) purification followed by size-exclusion chromatography (SEC), to identify potential isoforms. These materials are expected to be formed by around 10 monomers each, but the potential intrinsic variability in the products of the self-assembling process had not been investigated. These analyses revealed an important variability of the protein assemblies regarding the solvent-exposure of the carboxy histidine tails and the particle size, which includes oligomers with different number of building blocks. In a next step, protein subpopulations resulting from SEC were submitted to fluorimetry, DLS, small-angle X-ray scattering (SAXS), transmission electron microscopy (TEM), and field-emission scanning electron microscopy (FESEM) to characterize the GFP

fluorescence emission and the shape and size of individual oligomer species at ultrastructural level. These materials were also evaluated regarding their capacity to internalize target cells overexpressing the relevant receptor, by flow cytometry. A mathematical modelling was finally implemented to associate shape and geometry with the biological properties of the protein-only nanoparticles, mainly referring to fluorescence emission and cell penetrability, which are often observed as inversely related. In some nanoparticle populations, the amino-terminal segment of the building blocks appears as more solvent-exposed, which accounts for a better cell binding and receptor-mediated endosomal penetration.

The data obtained from this wide set of experimental approaches can be summarized around the concept that protein nanoparticles built by the combination of a cationic, cell targeting peptide at the amino terminal end of a recombinant GFP, and a histidine rich domain at the C-terminus, occur as a wide spectrum of oligomerization forms (see some examples in Figure 4). Such variability had been so far eclipsed by the pooled analysis of the recombinant material through more standard one-sided procedures. However, the major oligomeric states of these nanoparticles are highly coincident when comparing constructs harbouring unrelated amino-terminal cationic peptides such as A5G27 and T22 (targeted to different tumoral markers, namely CD44 and CXCR4, respectively), revealing a high consistence and very regular patterns in GFP oligomerization based on this simple platform.

Protein-only nanoparticles, based on self-assembling principles, are promising materials with important applicability in biomedicine as drug delivery systems and as imaging agents [16, 17]. How these supramolecular structures derived from controlled oligomerization behave, in terms of structural and functional robustness, is still a poorly explored issue. The analysis of the geometry and capacity for specific cell penetrability has been explored here, using as a model two related recombinant protein nanoparticles (sizing between 10 nm and 50 nm) but targeted to the tumoral markers CXCR4 and CD44 respectively. This particular oligomerization platform, based on cationic and histidine rich end terminal tails, is especially appealing regarding simplicity and biomedical potential. The obtained data indicate that despite the conformational spectrum of variant materials, there is a high regularity and structural and functional robustness of the produced oligomers, irrespective of the producing bacterial strain, that allows a high intrinsic cell penetrability and specificity in the receptor-dependent uptake.

OTHER REFERENCES

1. Corchero, J.L., et al., *Recombinant protein materials for bioengineering and nanomedicine.* Nanomedicine (Lond), 2014. **9**(18): p. 2817-28.

2. Li, D., et al., *Structure-Based Design of Functional Amyloid Materials.* Journal of the American Chemical Society, 2014. **136**(52): p. 18044-18051.

3. Lua, L.H., et al., *Bioengineering virus-like particles as vaccines.* Biotechnol Bioeng, 2014. **111**(3): p. 425-40.

4. Molino, N.M. and S.W. Wang, *Caged protein nanoparticles for drug delivery.* Curr Opin Biotechnol, 2014. **28**: p. 75-82.

5. Loo, Y., et al., *Self-Assembled Proteins and Peptides as Scaffolds for Tissue Regeneration.* Adv Healthc Mater, 2015. **4**(16): p. 2557-86.

6. Kumar, V.A., B.K. Wang, and S.M. Kanahara, *Rational design of fiber forming supramolecular structures.* Experimental Biology and Medicine, 2016. **241**(9): p. 899-908.

7. Yeates, T.O., Y. Liu, and J. Laniado, *The design of symmetric protein nanomaterials comes of age in theory and practice.* Curr Opin Struct Biol, 2016. **39**: p. 134-143.

8. Yeates, T.O., *Geometric Principles for Designing Highly Symmetric Self-Assembling Protein Nanomaterials.* Annu Rev Biophys, 2017.

9. Sutherland T.D. Rapson T.D., H.M.G., Church J.S., *Recombinant Structural Proteins and Their Use in Future Materials.* , in *Fibrous Proteins: Structures and Mechanisms.* , S.J. Parry D., Editor. 2017, Springer: Cham.

10. Kobayashi, N. and R. Arai, *Design and construction of self-assembling supramolecular protein complexes using artificial and fusion proteins as nanoscale building blocks.* Curr Opin Biotechnol, 2017. **46**: p. 57-65.

11. Guttenplan, A.P.M., et al., *Nanoscale click-reactive scaffolds from peptide self-assembly.* J Nanobiotechnology, 2017. **15**(1): p. 70.

12. Wei, G., et al., *Self-assembling peptide and protein amyloids: from structure to tailored function in nanotechnology.* Chem Soc Rev, 2017. **46**(15): p. 4661-4708.

13. Sutherland, T.D., M.G. Huson, and T.D. Rapson, *Rational design of new materials using recombinant structural proteins: Current state and future challenges.* J Struct Biol, 2018. **201**(1): p. 76-83.

14. Pesarrodona, M., et al., *Intracellular targeting of CD44+ cells with self-assembling, protein only nanoparticles.* Int J Pharm, 2014. **473**(1-2): p. 286-95.

15. Unzueta, U., et al., *Intracellular CXCR4(+) cell targeting with T22-empowered protein-only nanoparticles.* Int J Nanomedicine, 2012. **7**: p. 4533-44.

16. Unzueta, U., et al., *Towards protein-based viral mimetics for cancer therapies.* Trends Biotechnol, 2015. **33**(5): p. 253-8.

17. Serna, N., et al., *Protein-Based Therapeutic Killing for Cancer Therapies.* Trends Biotechnol, 2017.

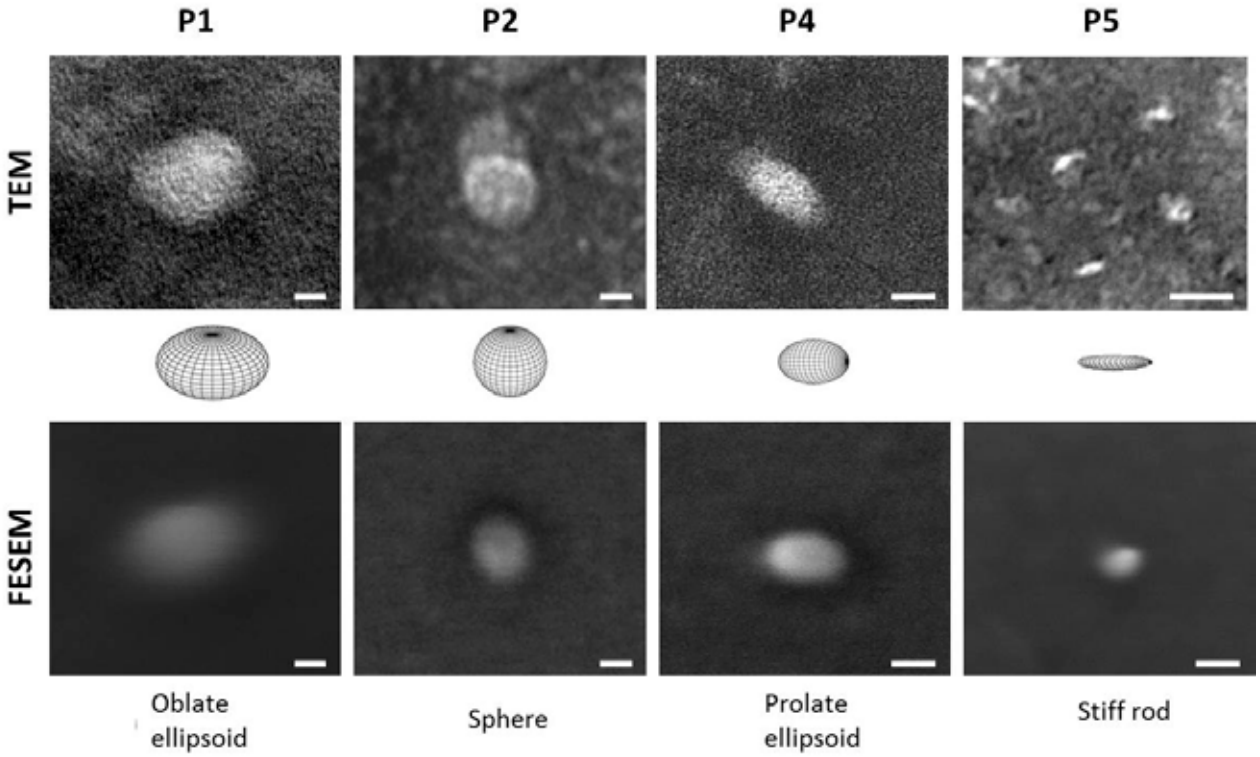

Figure 4: Ultrastructural characterization of morphometry (size and shape) of the different populations of GFP oligomers. TEM and FESEM images show representative T22-GFP-H6 oligomers produced in *E. coli*, classified by their occurrence in SEC peaks. Bar sizes represent 10 nm. Shapes within the panels correspond to the expected particle form based on the Rg/Rh ratio (Rg and Rh data obtained by SAXS and DLS respectively).

AFFILIATION:
1. Institute of Biotechnology and Biomedicine, Autonomous University of Barcelona, Bellaterra, 08193 Cerdanyola del Vallès, Spain.
2. Department of Genetics and Microbiology, Autonomous University of Barcelona, Bellaterra, 08193 Cerdanyola del Vallès, Spain.
3. CIBER of Bioengineering, Biomaterials and Nanomedicine, Bellaterra, 08193 Cerdanyola del Vallès, Spain.
4. ALBA Synchrotron, Carrer de la llum, 2-26, 08290 Cerdanyola del Vallès, Barcelona, Spain.
5. Department of Mathematics, Campus Diagonal Sud, Edifici U, Polytechnic University of Catalonia, Carrer de Pau Gargallo, 5, 08028 Barcelona, Spain.
6. Microscopy Service, Autonomous University of Barcelona, Bellaterra 08193 Cerdanyola del Vallès, Barcelona, Spain.
7. Biomedical Research Institute Sant Pau (IIB-Sant Pau) and Josep Carreras Leukemia Research Institute, Hospital de la Santa Creu I Sant Pau, 08025 Barcelona, Spain.

Structure determination of polycationic amphiphilic cyclodextrin-pDNA nanocomplexes, a new generation of nonviral carriers in gene therapy

Biophysics and protein corona analysis of Janus cyclodextrin-DNA nanocomplexes. Efficient cellular transfection on cancer cells. *Biochimica et Biophysica Acta (BBA) (1861)* 1737-1749 (2017)

María Martínez-Negro,[1] Emilio Aicart[1] and Elena Junquera*,[1]

The structure of paCD-pDNA CDplexes, obtained by SAXS, is known to play a key role on the transfection process, affecting its efficiency.

The key of gene therapy is the use of nucleic acids to cure inherent and acquired diseases at a molecular level. In order to effectively restore healthy cell functioning, two different strategies are used: the introduction (by means of a plasmid DNA) and expression of a copy of the affected or missing gene into the cells, or the insertion of a small interfering RNA (siRNA) to silence the expression of an abnormal gene responsible for the cell disorder. However, nucleic acids are easily degraded by nucleases in biological fluids, and their membrane-crossing abilities and cellular uptake are seriously limited by their negative charge, inherently large size, and rigidity. Formulation with appropriate delivery systems is thus essential for nucleic acids to overcome the physiological barriers, reach the target in a fully functional form and carry out the designed therapeutic function. Polycationic amphiphilic cyclodextrins (paCDs) have been found to be optimal nanocarriers due to their self-assembling properties and biomimetic cell-membranes-crossing aptitudes. In the presence of nucleic acids, they spontaneously form well-defined supramolecular complexes (CDplexes) whose structures are known to clearly affect their efficiency as transfecting agents. Small angle X-ray scattering (SAXS) is the technique of choice to determine these structures.

Preparation of CDplexes. Appropriate amounts of each polycationic amphiphilic CDs (paCDs), were dissolved in HEPES 20 mM, pH = 7.4, and homogenized with the help of sonication. Deionized water was used in the preparation of solutions. The paCDs thus prepared were left to rest during at least 20 minutes before mixing with pDNA to form the CDplexes. A stock solution of pDNA was prepared one day before the mixing with paCDs. The appropriate amount of cyclodextrin solution was added into a glass capillary, purchased from Hilgenberg with an outside diameter of 1.5 mm and wall thickness of 0.01 mm. After centrifuged at 4800 rpm (RCF or g-force value of 1900) for 2 min, the required amount of pDNA solution was added to obtain the desired paCDs/pDNA charge ratios, and the mixture was centrifuged again for 15 min at 4800 rpm. A solid CDplex pellet was formed at the bottom of the capillary. In all the samples, the pDNA concentrations were 10 μg/capillary. Finally, the capillaries were flame sealed.

Small-angle X-ray scattering. SAXS experiments were carried out on the beamline NCD at ALBA Synchrotron. The incident beam had an energy of 12.6 KeV

(λ = 0.995 Å). The machine is run in multibunch mode with a filling pattern consisting in 10 trains, 64 ns long and a gap of 24 ns between the trains. The scattered X-ray was detected on CCD detector Quantum 210r (4096 x 4096 pixels highest achievable resolution - pixel size 51 microns), converted to one-dimensional scattering by radial averaging, and represented as a function of the momentum transfer vector q (= $4\pi\sin\theta/\lambda$), in which θ is half the scattering angle and λ is the wavelength of the incident X-ray beam. The sample-to-detector distance was maintained at 1.4 m. Measurements on each sample, placed in a sealed capillary, were collected over 5 to 20 s each. SAXS experiments were run at different effective charge ratios (ρ_{eff}) between paCDs and the pDNA in the CDplexes.

Small-angle X-ray scattering (SAXS) experiments have been carried out to analyze the effectiveness of paCDs as nonviral gene vectors. The three molecular vectors named ADM70, ADM105 and PBO234 show a multitail lipophilic domain formed by fourteen hexanoyl groups and differing in the architecture of the multivalent cationic cluster. The complexes are constituted by each one of these paCDs and a plasmid DNA encoding the green fluorescent protein (pEGFP-C3). The experiments have been carried out at different effective charge ratios (ρ_{eff}) between the paCD and pDNA in the CDplexes. The diffractograms shown in Figure 5 provide information about the structure of ADM70-pDNA CDplex, as an example. As can be observed, the three peaks index well to a lamellar lyotropic liquid crystal phase (L_α), with the interlayer distance (d) directly related to the q factor $(d = 2\pi n / q_{hkl})$. This structure, represented in Figure 6, could be explained as alternating bilayers of paCDs (d_m) and an aqueous monolayer where the plasmid pDNA is allocated (d_w). Transfection and cell viability studies were done with HeLa and MCF7 cells in the presence of serum. The CDplexes herein studied show high transfection levels combined with high cell viability, better even than those obtained by the universal control Lipofectamine2000.

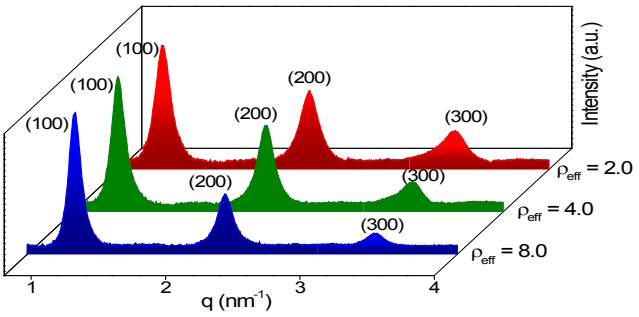

Figure 5: SAXS diffractograms of ADM70-pDNA CDplex at different effective charge ratios (ρ_{eff}). Notice that the observed peaks index well to a lamellar L_α structure.

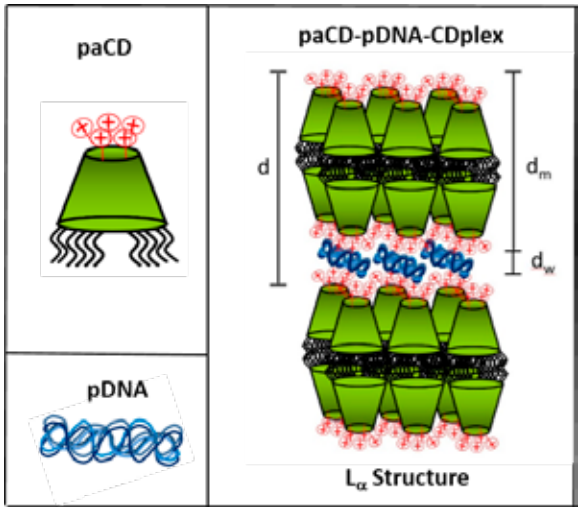

Figure 6: Schematic drawing of a paCD, the plasmid pDNA, and the multilamellar lyotropic liquid crystal phase (L_α) of the paCD-pDNA CDplexes with the structural parameters d, d_m and d_w

ACKNOWLEDGEMENTS

Authors thanks MINECO of Spain (contract number CTQ2015-65972-R) and University Complutense of Madrid (Spain) (project no. UCMA05-33-010) for financial support. SAXS experiments were performed at NCD beamline at ALBA Synchrotron Light Facility with the collaboration of ALBA staff.

AFFILIATION:

1. Group of Colloidal and Supramolecular Chemistry, Department of Physical Chemistry I, Faculty of Sciences, Complutense University of Madrid, 28040 Madrid, Spain.

Detection by micro-FTIR microscopy of the interaction of metallosurfactant aggregates with cells

Low-toxicity metallosomes for biomedical applications by self-assembly of organometallic metallosurfactants and phospholipids. *Chemical Communications* 53, 8455-8458 (2017)

M. Marín-García,[1] N. Benseny-Cases,[2] M. Camacho,[3] J. Suades,*[4] and R. Barnadas-Rodríguez*[1]

The study was carried out to check the ability of supramolecular aggregates constituted by metallosurfactants and phospholipids to act as an efficient drug delivery system. After cell incubation, metallosurfactants were localized in the cells, using micro-FTIR microscopy coupled to synchrotron radiation.

Surfactants (molecules that have water soluble and oil soluble parts) that contain a metal atom in their structure are named metallosurfactants (MTS). They have aggregation properties and are able to form supramolecular aggregates (micelles, vesicles, etc.). The presence of the metal makes possible to use these aggregates in a broad range of applications such as catalysis, optoelectronics and biomedicine. The authors have reported a new organometallic MTS (Fig. 7a and 7b) wherein the metallic fragment is in the hydrophobic part of the molecule and when mixed with soy phosphatidylcholine (SPC) –the main constituent of biological membranes– lead to different types of supramolecular aggregates. Thus, vesicles, micelles, bicelles and rods can be obtained by modulating the mol ratio of the components. Most of these structures are stable upon dilution and, furthermore, due to the fact that the metal atom (Mo) is linked to several CO, they release CO under UVA or visible irradiation. This is an important fact since it has been shown that the local delivery of CO has important potential uses in medicine. It has anti-inflammatory properties and its beneficial effects have been studied in vascular disorders and also in digestive inflammation processes. Thus MTS/SPC aggregates become good candidates to achieve a local delivery of CO upon irradiation.

Authors aimed to study the effect of two type of mixed aggregates of SPC and MTS with CO releasing properties on fibroblasts cell cultures. MTS/SPC suspensions were obtained using MTS with one (PCO) or two chains (TCO) and n = 1 (Fig. 7a and 7b respectively) by hydration of a homogeneous dry thin film of both substances, subsequent addition of aqueous medium and finally vortexing. Under these conditions the system spontaneously generates the most stable aggregates formed by intimate mixing of these substances. Depending on the SPC to MTS molar ratio, vesicles or micelles were obtained (Fig. 8). Toxicity of vesicles and micelles was checked using human dermal fibroblasts cultures and the results showed that only mixed MTS/SPC vesicles were non-toxic at the highest concentration checked, 1000 μM.

Both mixed liposomes and micelles have been shown to be CO releasing structures using the myoglobin assay and FTIR spectrometry. Using the infrared technique, authors monitored the evolution of the CO bands of the mixed aggregates under UVA and visible light. These bands are located between 2040-1820 cm^{-1}(Fig. 9), a region where there is no biomolecules absorption and therefore they can be monitored when the MTS are in a biological medium. This absorption window allows to detect the MTS into the cells

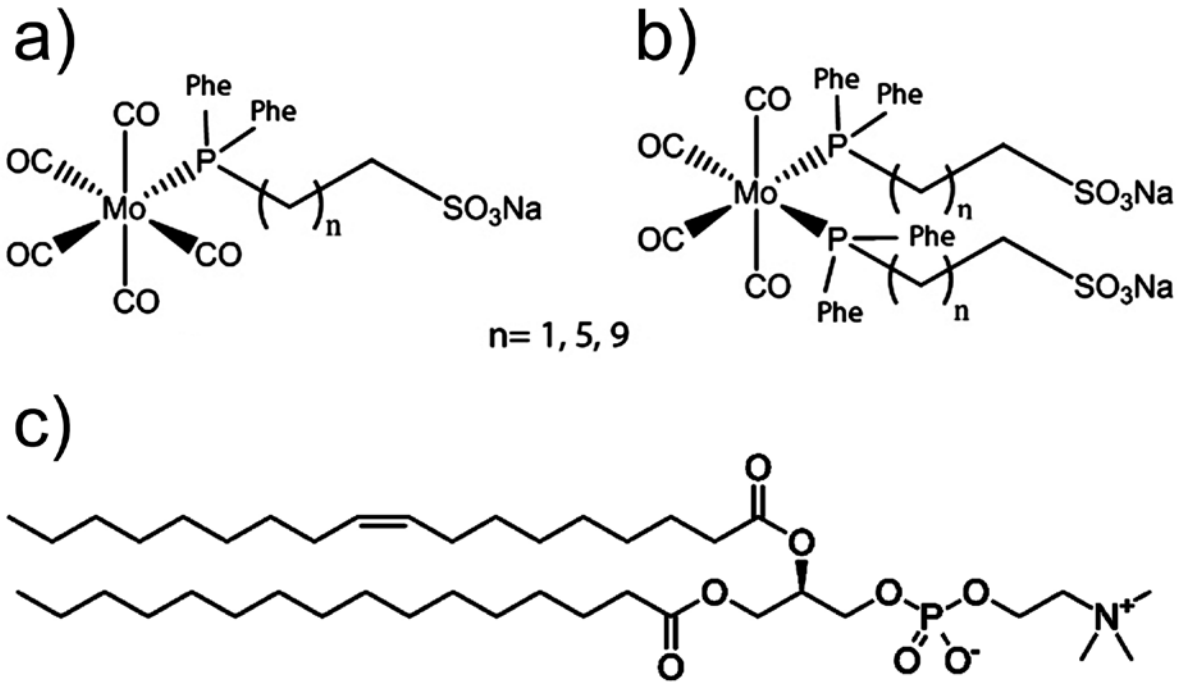

Figure 7: Structures of metallosurfactants which contain a) 5 CO (PCO) or b) 4 CO (TCO) groups, and of c) phosphatidylcholine.

by IR-microscopy using synchrotron radiation. A high intensity infrared beam was necessary to detect with high signal-to-noise ratio the absorbance of the CO groups of the CORMs and to get a higher spatial resolution in order to locate these groups in the cells.

For the IR-microscopy experiments, cells were incubated with the aggregated systems (vesicles or micelles) at two final concentrations of CORM (250 µM and 1000 µM) for 12 hours. After the incubation, the cells were rinsed and fixed with paraformaldehyde to be analyzed.

FTIR absorbance spectra were acquired from several individual cells with the IR microscope using the 36x optics with SR illumination and single channel MCT detector in the mid-IR range 4000 - 500 cm^{-1}, at a spectral resolution of 4 cm^{-1} co-adding a minimum of 256 scans (~ 40 sec per spectrum). An aperture of 10 microns was used with a step size of 6 microns for oversampling.

The MTS characteristic CO vibration band was detected in the cells incubated with both PCO and TCO at 1000 µM when forming vesicles or micelles. Fig. 9 shows the results for the TCO/SPC vesicles normalized to the total protein content of the samples (amide I band at 1650 cm^{-1}), providing evidence of the MTS presence in the cells.

In conclusion, authors demonstrated that the simple mixing of metallosurfactants and soy phosphatidylcholine leads to the formation of stable aggregated systems. Their physical characteristic can be modulated by the molar ratio of the components so that vesicles or micelles can be easily obtained. These structures contain metal atoms in their membranes, are stable upon dilution and release CO upon UVA or visible irradiation, which makes them feasible to act as a local CO delivery system. Both types of aggregates are able to interact with cells, as has been observed by micro-FTIR spectroscopy using synchrotron radiation.

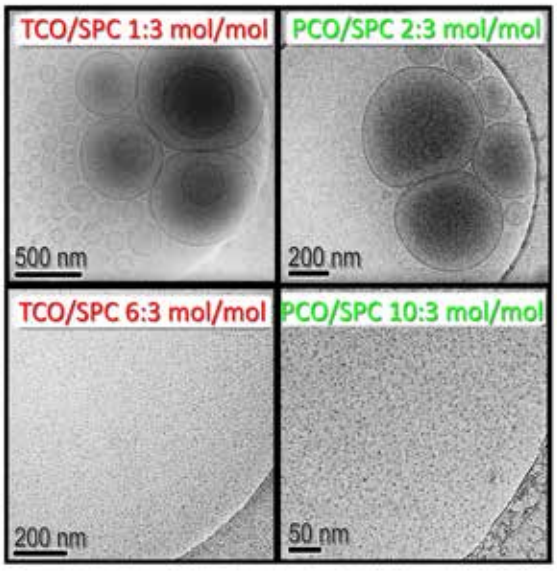

Figure 8: Cryo-TEM images of mixed systems of MTS and SPC. Depending on the mol ratio of the component vesicles (upper images) or micelles (lower images) can be obtained.

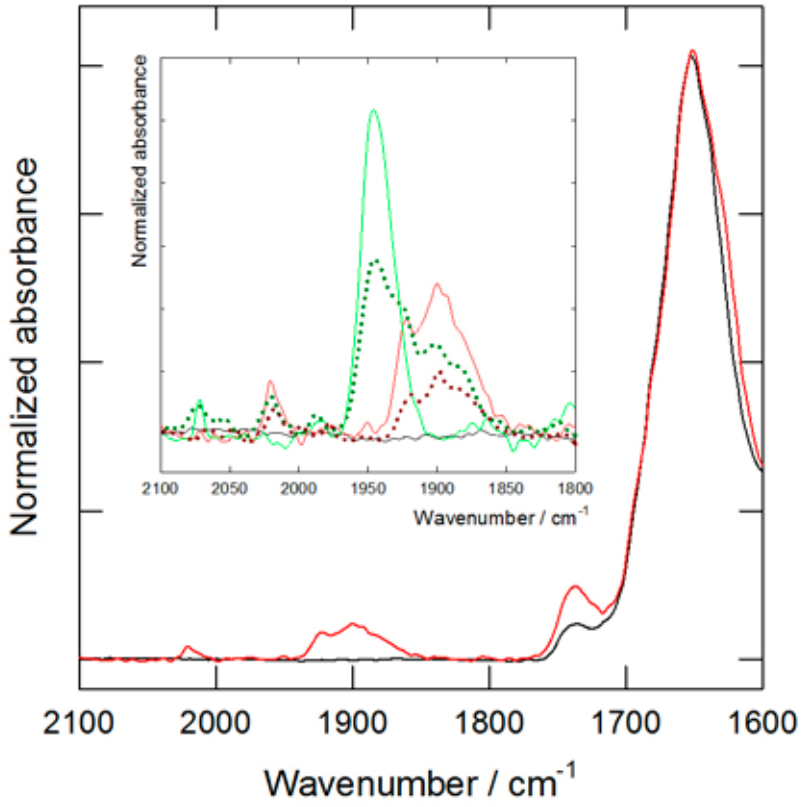

Figure 9: Micro-FTIR spectra (normalized to the protein content of the samples using the amide I band at 1650 cm-1) of fixed cell cultures of fibroblasts after incubation with a cell culture medium (black) or TCO/SPC 1000 : 3000 mM/mM vesicles (red) for 12 h. Inset: Details of the CO absorption range for cultures incubated with TCO/SPC 1000 : 3000 mM/mM vesicles (red); TCO/SPC 1000 : 500 mM/mM micelles (dotted dark red); PCO/SPC 1000 : 3000 mM/mM vesicles (green); and PCO/SPC 1000 : 300 mM/mM micelles (dotted dark green).

ACKNOWLEDGEMENTS

This work was supported by ALBA synchrotron, Spanish MINECO-ERDF grants (BIO2015-67358-C2-2-P and CTQ2015-70371-REDT) and by the Government of Catalonia (2014SGR-423).

OTHER REFERENCES

1. R. Motterlini, L. E. Otterbein, Nat. Rev. Drug. Discov., **2010**, 9(9), 728-743.

2. C. Kautz, P. C. Kunz, C. Janiak, Dalton Trans., **2016**, 45, 18045-18063;

3. U. Hasegawa, A. J. van der Vlies, E. Simeoni, Ch. Wandrey, J. A. Hubbell, J. Am. Chem. Soc., **2010**, 132, 18273-18280.

4. G. J. L. Bernardes and S. García-Gallego, Angew. Chem. Int. Ed., **2014**, 53, 9712-9721.

5. Parera, E; Comelles, F.; Barnadas, R.; Suades, J. *Langmuir*, **2010**, *26*, 743-751.

6. E. Parera, F. Comelles, R. Barnadas J. Suades, Chem. Commun., **2011**, 47, 4460-4462;

7. E. Parera, M. Marín-García, R. Pons, F. Comelles, J. Suades, R. Barnadas-Rodríguez, Organometallics, **2016**, 35, 484-493.

AFFILIATION:

1. Biophysics Unit/Center for Biophysical Studies, Department of Biochemistry and Molecular Biology, Faculty of Medicine, Universitat Autònoma de Barcelona, Avda. de Can Domènech, 08193 Cerdanyola, Spain.

2. ALBA Synchrotron, Carrer de la Llum 2-26, 08290 Cerdanyola, Spain

3. Laboratory of Angiology, Vascular Biology and Inflammation / Institute of Biomedical Research, Hospital de la Santa Creu i de Sant Pau, Universitat Autònoma de Barcelona, Sant Antoni Maria Claret, 167, 08025 Barcelona, Spain

4. Department of Chemistry, Edifici C, Universitat Autònoma de Barcelona, 08193 Cerdanyola, Spain.

Iron oxide nanoparticles stress the cells

Toxicogenomics of iron oxide nanoparticles in the nematode *C. elegans*. *Nanotoxicology* **11**, 5 (2017)

L. Gonzalez-Moragas [1], Si-Ming Yu [2], N. Benseny-Cases[3], S. Stürzenbaum [4], A. Roig [1] and A. Laromaine *[1]

Authors present a study on the toxicity of iron oxide nanoparticles based on the analysis of specific genetic markers linked to nanotoxicity in the *C. elegans* organisms. The study suggests that nanoparticles can be captured by intestinal cells in their interior, interact with cell lipids and activate cellular mechanisms of oxidative stress.

Nanoparticles present unique properties and offer very promising possibilities in medicine but their use must be safe and tested. *Caenorhabditis elegans (C. elegans)* are 1-mm-long nematodes used as a model organism for genetic studies, given that they have its whole genome sequenced. The advantageous characteristics of this worm, such as its transparency, short life cycle (4-5 days), short life (2-3 weeks), ease of operation and low cost of maintenance, among others, have been used by the authors to evaluate the use of nanoparticles for applications in medicine.

In this work, researchers exposed the model organism *C. elegans* to 6-nm superparamagnetic iron oxide nanoparticles (SPIONs) to study the molecular pathways affected by these nanoparticles. The data gathered show that some nanoparticles cross the intestinal barrier of *C. elegans* in processes involving a cell membrane protein, clathrin. In addition, differences in the gene expression were observed depending on the type of nanoparticles to which the worms were exposed.

In order to measure the degree of lipid oxidation, Fourier-transform infrared (FTIR) microspectroscopy analysis was performed at the MIRAS beamline of the ALBA Synchrotron to investigate the role of oxidative stress in SPION toxicity. Results showed that the band at 1741 cm^{-1}, corresponding to carbonyl groups (product of lipid oxidation reaction), was more intense in the spectra of SPION treated *C. elegans* than in untreated

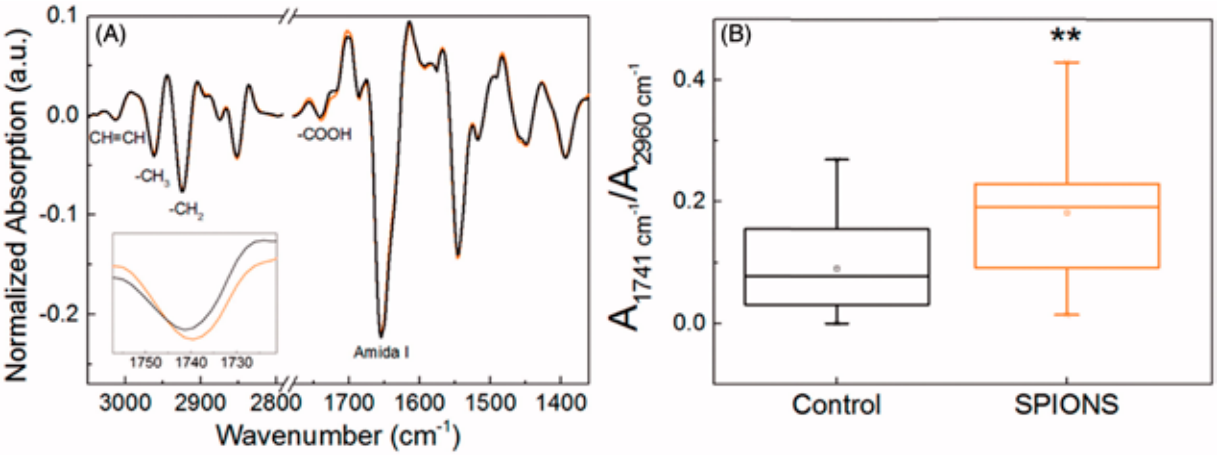

Figure 10: (A) Derivative of the mean FT-IR spectra of control (black) and SPION-treated (orange) C. elegans. The inset shows a zoom-in of the 1741 cm-1 band. (B) Box plot of the lipid oxidation ratio (1741 cm^{-1}/2960 cm^{-1}) of all spectra, for control and SPION-treated animals **p < .01.

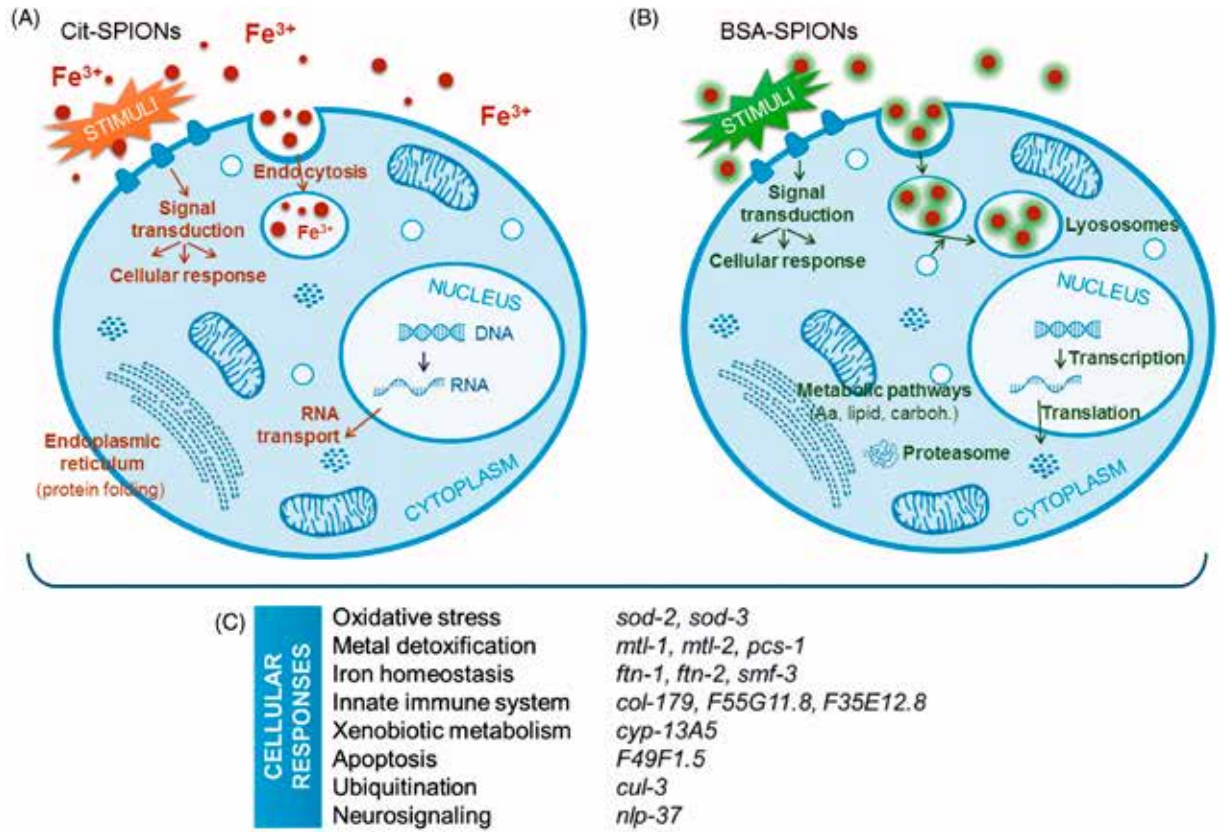

Figure 11: Pathways affected by (A) Cit-SPIONs and (B) BSA-SPIONs, identified in the pathway enrichment test. After Cit-SPIONs, oxidative dissolution could occur, while the BSA coating would prevent ion release from BSA-SPIONs. (C) Cellular responses investigated by qPCR in SPION-treated worms.

animals. This band, normalized by total lipid (CH_3 groups), showed significant differences between untreated and treated animals ($p<.01$), indicating that lipid oxidation is induced by SPION treatment.

Studies like this demonstrate that by identifying the molecular mechanisms responsible for biological responses observed after exposure to nanoparticles, it is possible to understand and predict their behavior, and optimize their design to achieve low toxicity and safer nanomaterials for humans.

ACKNOWLEDGEMENTS

Victor Fuentes is acknowledged for his collaboration in the synthesis of gold nanoparticles. Acknowledgement is also given for the core funding from the King's College London and the access and support of the King's Genomic Centre. This research was partially funded by the Spanish Ministry of Economy and Competitiveness and co-funded by European Social Funds through project MAT2015-64442-R, the 'Severo Ochoa' Program for Centers of Excellence in R&D (SEV- 2015- 0496), the Ramon y Cajal program (AL, RyC-2010-06082) and the FPU program (LGM, FPU12/05549). SY acknowledges Chinese Fundamental Research Funds for the Central Universities (21616306), the Government of Catalonia (2014SGR213), People Program of the European Commission (grant agreement no. 303630, co-funded by the European Social Fund) and the COST Action GENIE (Action No. BM1408-A).

AFFILIATION:

1. Group of Nanoparticles and Nanocomposites, Institute of Materials Science of Barcelona (ICMAB-CSIC), UAB Campus, Bellaterra, Spain
2. Key Laboratory of Biomaterials of Guangdong Higher Education Institutes, Department of Biomedical Engineering, Jinan University, Guangzhou 510632, China.
3. ALBA Synchrotron, Carrer de la Llum 2-26, 08290 Cerdanyola, Spain
4. Faculty of Life Sciences and Medicine, Analytical and Environmental Sciences division, King's College London, UK

SCIENTIFIC RESULTS

ENERGY-RELATED MATERIALS

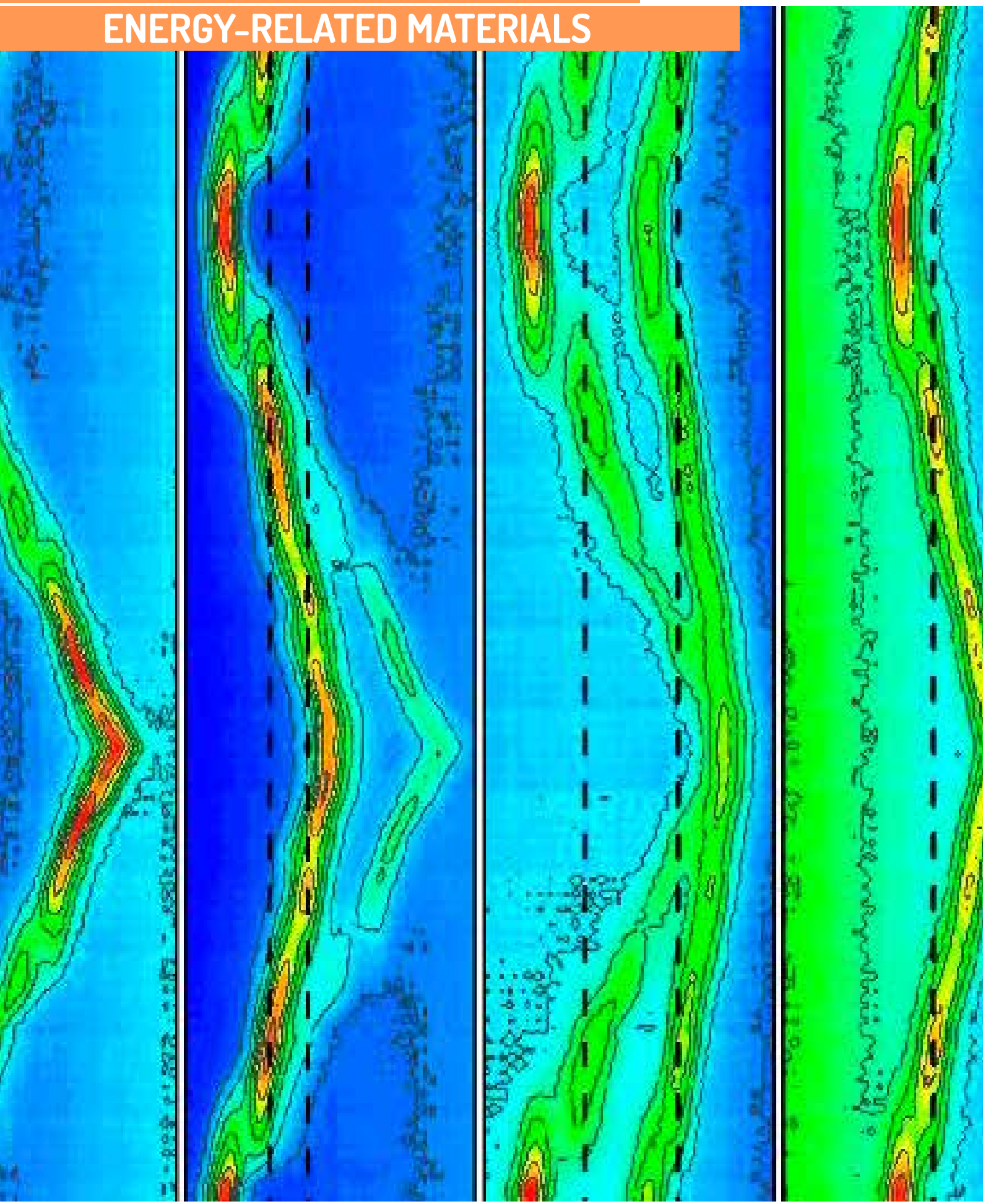

Courtesy of Dr. Fei Du.

A study of single-ion triblock copolymer electrolytes based on poly(ethylene oxide) and methacrylic sulfonamide segments

Single-ion triblock copolymer electrolytes based on poly(ethylene oxide) and methacrylic sulfonamide blocks for lithium metal batteries. *Journal of Power Sources* 364 191-199 (2017)

Luca Porcarelli,[1] M. Ali Aboudzadeh,[1] Laurent Rubatat,[*3] Jijeesh R. Nair,[2]Alexander S. Shaplov,[4,5] Claudio Gerbaldi,[2] David Mecerreyes[1]

A new family of single-ion conducting polymer electrolytes based on ABA triblock copolymers for application in solid-state batteries was synthesized and composition/morphology relationships were investigated with SAXS/WAXS measurements.

Polymer electrolytes are expected to replace liquid organic carbonates in the next generation of lithium batteries [1,2]. Additionally to enhanced safety and good mechanical properties, polymer electrolytes can display unique properties such as a lithium-ion transference number (t^+) approaching unity. This new class of materials – namely single-ion polymer electrolytes (SIPE) – may solve the major issue of salt concentration gradients limiting battery lifetime and performance. Sustained by this idea, the authors designed a triblock copolymer electrolyte having a polyethylene oxide central segment (PEO) and methacrylic sulfonamide side segments (PLiMTFSI). The prepared SIPE combined the good ion solvation characteristics of PEO with the single-ion properties of PLiMTFSI. The authors investigated the composition/morphology relationship of the copolymer using a combination of differential scanning calorimetry (DSC), small-angle and wide-angle X-ray scattering (SAXS-WAXS) in order to elucidate the effect on the ionic conductivity of the SIPE.

The authors prepared a series of PLiMTFSI–PEO–PLiMTFSI triblock copolymer using RAFT polymerization techniques. The length of the PLiMTFSI segments varied between 3 and 13 kDa whereas the length of the central PEO segment was 35 kDa for all samples. The chemical structure and weight composition of the copolymers is shown in Figure 12.

SAXS and WAXS spectra of the samples are shown in Figure 13a-b. Copolymers having 3 and 6 kDa PLiMTFSI blocks showed the characteristic signature of PEO crystallinity, as revealed by two major peaks at 13.6 and 16.5 nm^{-1} in the WAXS spectra [3]. The block copolymer self-assembly was mainly driven by PEO crystallization into lamellar crystallites, as suggested by the large range ordering observed on the 6 kDa sample with a second order peak. Increasing the molar mass of PLiMTFSI to 8 and 11 kDa changed dramatically both SAXS and WAXS spectra. The WAXS spectra reveal that the PEO crystallinity significantly decreases as compared to 3 and 6 kDa samples. A decrease in number and interaction of the scattering objects was observed, i.e. the PEO crystalline lamella; which leads to a transition from a structure to a form factor. To support this assertion and to estimate the lamellae thickness, a model disk form factor was plotted on

Figure 13a, with both minima corresponding well to the ones of the experimental curves. On Figure 13c-d, SAXS and WAXS scattering spectra of the 6 kDa PLiMTFSI copolymer are presented as a function of temperature from 25 to 70 ºC. Between 25 and 50 ºC the spectra were not significantly evolving, and a strong PEO crystallinity level associated with a lamellar morphology was present, as discussed previously. At 60 ºC there was significant decrease of crystallinity, which induced a drop in number and interaction of the scattering objects as shown by the SAXS spectrum evolving toward a form factor. At 70 ºC, the crystallinity fully disappeared and so did the larger length scale morphology. The X-ray diffraction results were supported by DSC results of Figure 14, showing that the degree of crystallinity decreased with the size of the PLiMTFSI segment (X_c = 51% to ~0%) and the glass transition temperature increased (T_g = – 55 °C to 7 °C).

Ionic conductivities (σ) of copolymers were measured via electrochemical impedance spectroscopy (EIS) and the results are plotted in Figure 15. All samples showed a sharp increase in σ above the PEO melting temperature. The steep increase was more pronounced for the samples presenting a lamellar morphology (3, 6 kDa PLiMTFSI segments), thus suggesting that PEO lamellae hinder lithium ions conduction in the SIPE. Moreover, σ passed through a maximum increasing the length of PLiMTFSI segments. This behavior was explained as a trade-off between the decreasing degree of crystallinity and the reduced backbone mobility, as a consequence of higher T_g [4].

In summary, this study demonstrated the composition/morphology relationship of PLiMTFSI–PEO–PLiMTFSI copolymer electrolytes. At room temperature, SAXS and WAXS spectra suggested self-assembly of the copolymers into lamellar morphology, whereas such morphology features disappeared at higher temperatures. X-ray scattering results were supported by DSC data. Finally, triblock copolymers were tested in lab-scale lithium metal cells at 70 ºC. Excellent specific capacity deliveries were measured, ranging from 153 mAh g^{-1} at C/10 to 99 mAh g^{-1} at C/2. In addition, lithium polymer cells demonstrated outstanding cycling stability during accelerated aging tests. The prepared SIPEs represents a promising advance towards the next generation of lithium batteries with solid-state electrolytes.

ACKNOWLEDGEMENTS

This work was supported by the Russian Foundation for Basic Research (project no. 14-29-04039_ofi_m) and by the European Commission (project no. 318873 «IONRUN»). L.P acknowledges financial support of the European Commission through project RENAISSANCE-ITN 289347. J.R.N. acknowledges financial support from the European Commission under the MARS-EV project (Grant agreement no. 609201). The authors acknowledge ALBA for the provision of synchrotron radiation facilities and thank M. Malfois for assistance in using beamline BL11-NCD.

OTHER REFERENCES

1. J.B. Goodenough, Y. Kim, Challenges for rechargeable Li batteries, Chem. Mat.**22** (2010) 587-603.

2. K. Xu, Electrolytes and interphases in Li-Ion batteries and beyond, Chem. Rev.**114** (2014) 11503-11618.

3. C.M. Burba, R. Frech, B. Grady, Stretched PEOeLiCF3SO3 films: polarized IR spectroscopy and X-ray diffraction, Electrochimica Acta **53** (2007) 1548-1555.

4. A.S. Shaplov, R. Marcilla, D. Mecerreyes, Recent advances in innovative polymer electrolytes based on poly(ionic liquid) s, Electrochimica Acta **175** (2015) 18-4.

AFFILIATION:

1. POLYMAT, University of the Basque Country (UPV/EHU), Joxe Mari Korta Center, Avenida Tolosa 72, 20018 Donostia-San Sebastian, Spain.

2. Department of Applied Science and Technology (DISAT), Politecnico di Torino, Corso Duca degli Abruzzi 24, 10129 Torino, Italy.

3. CNRS/UNIV Pau & Pays Adour, Institute of Analytical Sciences and Physical Chemistry for the Environment and the Materials, UMR5254, 64000 Pau, France.

4. A.N. Nesmeyanov Institute of Organoelement Compounds Russian Academy of Sciences (INEOS RAS), Vavilov str. 28, 119991 Moscow, Russia.

5. Luxembourg Institute of Science and Technology (LIST), 5 Avenue des Hauts-Fourneaux, L-4362 Esch-sur-Alzette, Luxembourg.

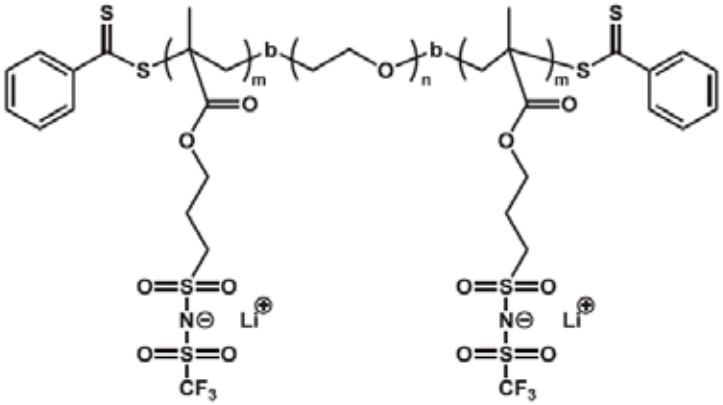

PLiMTFSI-PEO-PLiMTFSI
3k – 35k – 3k
6k – 35k – 6k
8k – 35k – 8k
11k – 35k – 11k
13k – 35k – 13k

Figure 12: Chemical structure and weight composition of PLiMTFSI-PEO-PLiMTFSI triblock copolymers electrolytes.

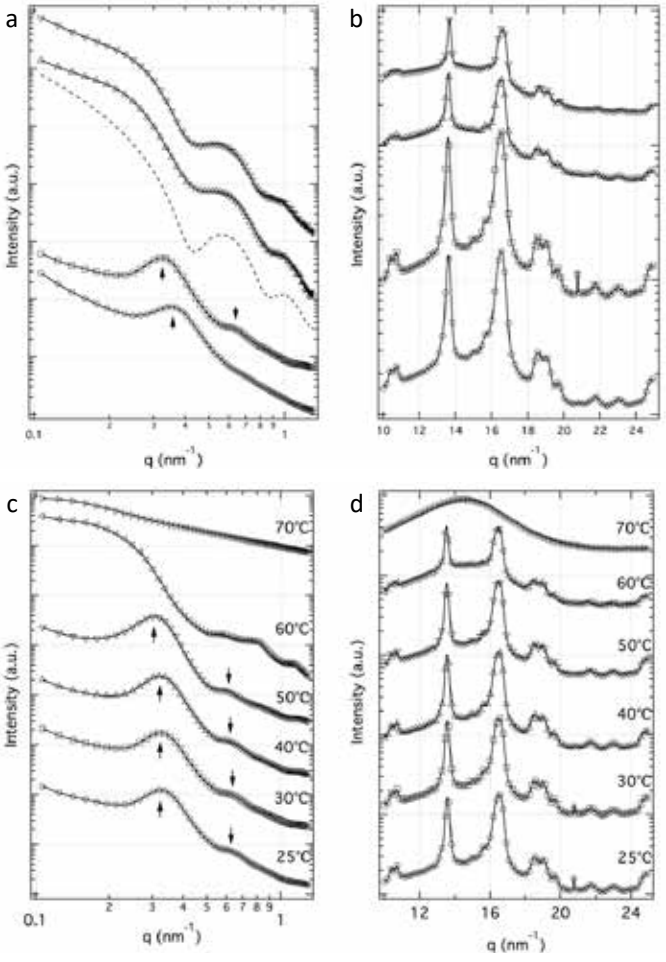

Figure 13: SAXS (a) and WAXS (b) scattering spectra measured at 25 °C on sample 3k-35k-3k (circles), 6k-35k-6k (squares), 8k-35k-8k (triangles up) and 11k-35k-11k (triangles down). The dash line curve corresponds to a disk form factor, with a 15 nm thickness and a large radius, 500 nm. SAXS (c) and WAXS (d) scattering spectra measured on sample 6k-35k-6k with increasing temperature: 25 °C (circles), 30 °C (squares), 40 °C (triangles up), 50 °C (triangles down), 60 °C (triangles left) and 70 °C (triangles right). The spectra are displayed in a log-log plot as a function of the scattering vector. For the sake of clarity, the spectra are shifted vertically and the intensity is an arbitrary unit.

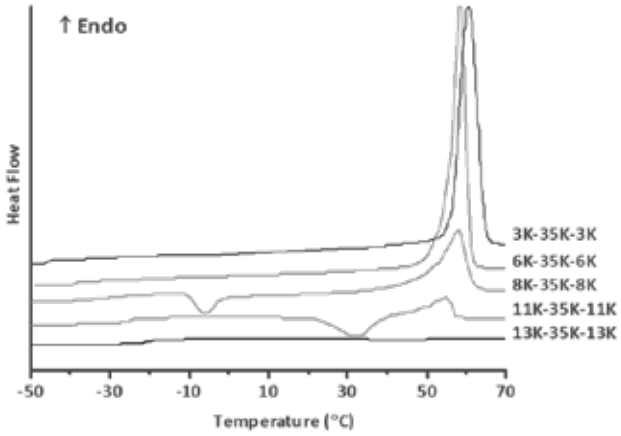

Figure 14: Differential scanning calorimetry traces of PLiMTFSI–PEO–PLiMTFSI triblock copolymers.

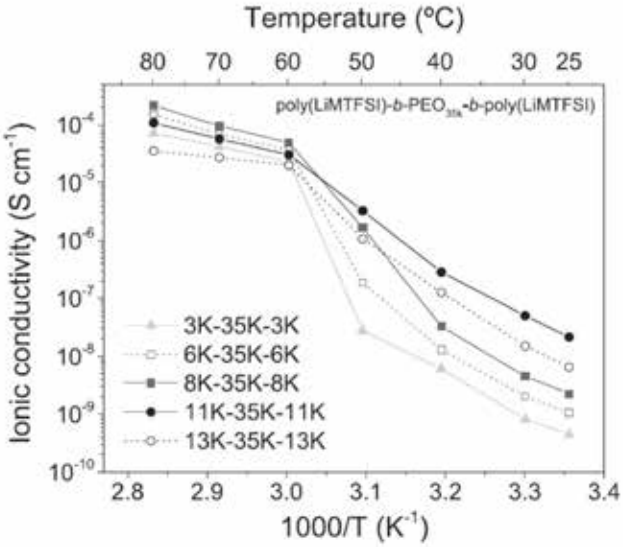

Figure 15: Arrhenius plot of ionic conductivity versus temperature for PLiMTFSI-PEO-PLiMTFSI electrolytes.

A New NASICON-Structured $Na_2VTi(PO_4)_3$@C Nanocomposite as the Bipolar Electrode Material for High-Performance Symmetric Sodium-Ion Batteries

Sodium vanadium titanium phosphate electrode for symmetric sodium-ion batteries with high power and long lifespan. ***Nature Communications*** **8**:15888 (2017)

Dongxue Wang[1], Xiaofei Bie[1], Qiang Fu[2], Ditty Dixon[2], Natalia Bramnik[2], Yong-Sheng Hu[3], Francois Fauth[4], Yingjin Wei[1], Helmut Ehrenberg[2], Gang Chen[1] and Fei Du[1]

The reaction mechanism of $Na_2VTi(PO_4)_3$ is identified through *in-situ* synchrotron and X-ray absorption spectrum and a high-performance symmetric battery based on $Na_2VTi(PO_4)_3$ highlights its potential application in smart grid.

Sodium-ion batteries operating at ambient temperature hold great promise for use in grid energy storage owing to their significant cost advantages. However, challenges remain in the development of suitable electrode materials to enable long lifespan and high-rate capability. Here, the authors report a Na super-ionic conductor structured electrode, sodium vanadium titanium phosphate, which delivers a high specific capacity of 147 mA h g^{-1} at a rate of 0.1C and an excellent capacity retention at high rates. A symmetric sodium-ion full cell demonstrates a superior rate capability with a specific capacity of about 49 mA h g^{-1} at 20 C rate and ultralong lifetime over 10,000 cycles. Furthermore, *in-situ* synchrotron diffraction and X-ray absorption spectroscopy measurements are carried out to unravel the sodium storage mechanism and the charge compensation behavior. The results suggest the potential application of symmetric battery for electrochemical energy storage owing to the superior rate capability and long cycle life.

Firstly, the stoichiometric amount of Na_2CO_3, NH_4VO_3, $(CH_3CH_3CHO)_4Ti$ and $NH_4H_2PO_4$ with a molar ratio of 1 : 1 : 1 : 3 was dissolved in 0.02 M aqueous citric acid [$HOC(COOH)(CH_2\text{-}COOH)_2$] solution. Then the solution was stirred at 80 °C for 12 h to get a precursor. The precursor was pre-treated at 350 °C for 5 hours, followed by sintering at 800 °C for 12 hours under nitrogen atmosphere to obtain the $Na_2VTi(PO_4)_3$@C nanocomposite. Raman spectroscopy was performed on a Renishaw inVia Raman microscope with Ar-ion laser excitation (λ= 514.5 nm). The content of carbon in the $Na_2VTi(PO_4)_3$@C nanocomposite was evaluated using a Mettler-Toledo CHN analyzer. A FEI Tecnai G2 type transmission electron microscope (TEM) was used to investigate morphology and microstructure. Synchrotron diffraction was performed at the powder diffraction beam line (MSPD) at ALBA, Barcelona, using synchrotron radiation with an energy of 30 KeV (λ= 0.413364 Å) and a MYTHEN 1D position-sensitive detector. *In-situ* XAS measurements were carried out at the P65 beamline at PETRA III (DESY, Hamburg). XAS spectra where recorded in quick-XAS (10 min/spectrum) mode in fluorescence geometry using a PIPS diode. Both Ti as well as V K edges where measured in one go. All the XAS spectra were processed using DEMETER software package. The electrochemical properties of the as-prepared $Na_2VTi(PO_4)_3$@C nanocomposite were examined by assembling coin-type half cells with sodium foil as the counter electrode. The electrodes were prepared by coating a slurry, in which the $Na_2VTi(PO_4)_3$@C active materials, Super P conductive and polyvinylidene fluoride

(PVDF) binders dissolved in Nmethylpyrrolidone (NMP) were mixed in a weight ratio of 7 : 2 : 1 on an aluminum foil current collector. The cathode loading mass is around 1.75 to 2.2 mg cm^{-2}. These electrode films were dried in a vacuum oven at 120 °C for 10 hours. After dividing the electrode film into square parts of 0.8×0.8 cm^2, coin cells were assembled in a glove box. The separators of the cells were a glass fiber filter (Whatman GF/C). The electrolyte was 1 M $NaClO_4$ dissolved in a solvent of ethylene carbonate (EC) and propylene carbonate (PC) (1: 1 v/v). Galvanostatic charge–discharge cycling was then performed on a Land-2001A (Wuhan, China) automatic battery tester. Cyclic voltammetry (CV) was performed on a VSP multichannel potentiostatic-galvanostatic system (Bio-Logic SAS, France). In symmetrical sodium-ion battery test, the battery was assembled into a coin-type full cell and was anode limited with as-prepared $Na_2VTi(PO_4)_3$@C as both cathode and anode. Cell balance was achieved by setting the electrode mass ratio of cathode/anode to 1.6 (the anode loading mass is around 1.75 to 2.2 mg cm^{-2}). 1C corresponds to 125 mA g^{-1}.

In summary, by optimizing transition metal ions of V^{3+} and Ti^{4+} with similar ionic radii and a substantial difference in redox potential, researchers designed and synthesized a NASICON-structured compound $Na_2VTi(PO_4)_3$. It has been found that this material exhibits successive working plateaus at 3.4 V and 2.1 V, corresponding to the redox couples of V^{3+}/V^{4+} and Ti^{4+}/Ti^{3+}, respectively. By taking advantage of this potential difference, a symmetric full cell using hybrid $Na_2VTi(PO_4)_3$@C electrodes was constructed, with manifest high-rate capacity and ultralong lifespan over 10,000 cycles. Moreover, *in-situ* synchrotron and XAS measurements were carried out to unveil the structural evolution and charge compensation mechanism. This study highlights the prospect of NASICON-type structure as a materials platform to improve the Na-ion storage performance for high-power and long-lived SIBs.

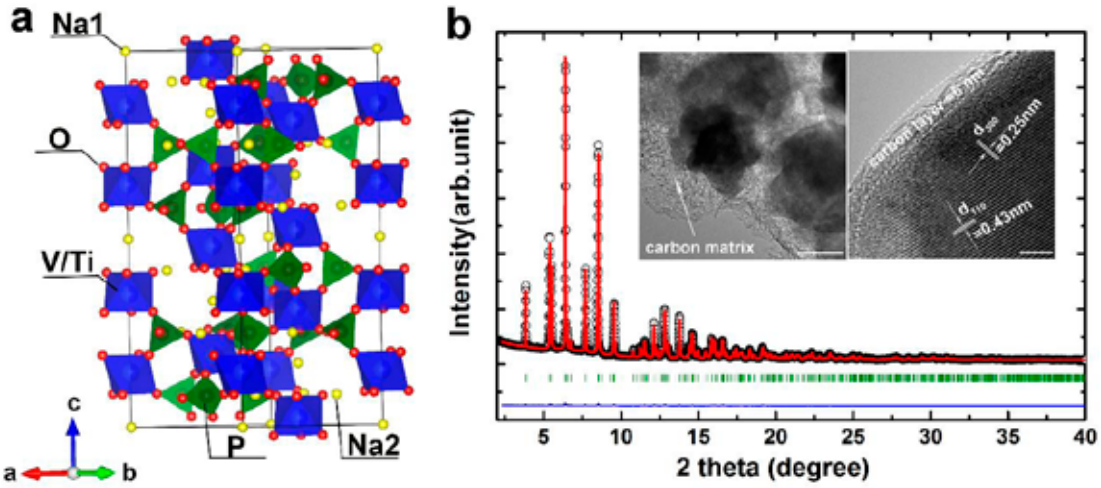

Figure 16: Structure of $Na_2VTi(PO_4)_3$: (a) Schematic crystal structure of $Na_2VTi(PO_4)_3$, and a, b and c represent different axes; (b) Rietveld refinement based on the synchrotron diffraction data. Black circle, red line and blue line represent the observed, calculated and difference patterns, respectively. The olive tick marks correspond to the Bragg reflections; the inset shows the TEM (scale bar is 100 nm) and HRTEM images (scale bar is 4 nm).

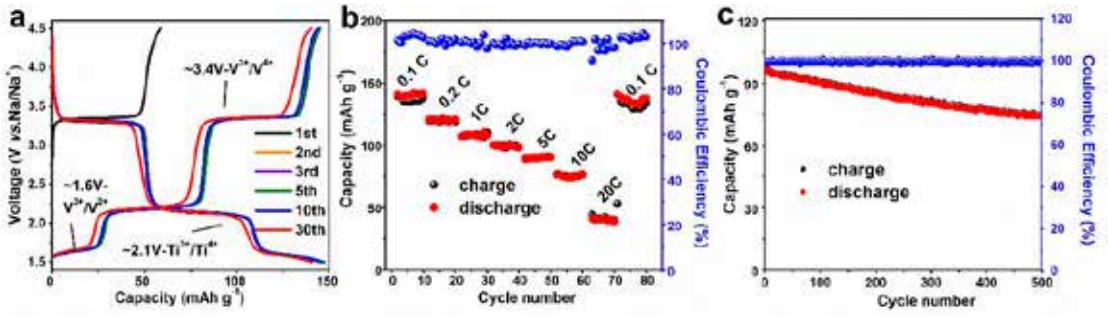

Figure 17: Sodium storage performance of $Na_2VTi(PO_4)_3$@C electrode: (a) the 1st, 2nd, 3rd, 5th, 10th, 30th galvanostatic charge-discharge profiles between 1.5 and 4, 5 V at a current density of 1 C (1 C corresponds to 125 mA g^{-1}); (b) Rate capability from 0.1 to 20 C; (c) Long-term cycle life over 500 cycles at 10 C rate.

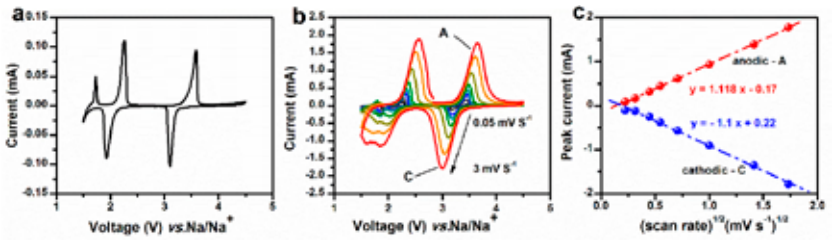

Figure 18: Kinetic properties of $Na_2VTi(PO_4)_3$@C electrode: (a) Cyclic voltammogram curve of the $Na_2VTi(PO_4)_3$@C nanocomposite at a scan rate of 0.05 mV s^{-1} between 1.5 and 4.5 V; (b) Cyclic voltammograms curves at different scanning rates; (c) The relationship between the peak current (*Ip*) and the square root of the scan rate ($v^{1/2}$) .

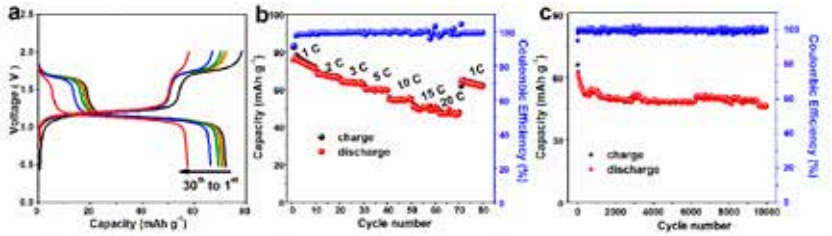

Figure 19: Electrochemical performance of the symmetric full cell: (a) Galvanostatic charge-discharge profiles between 0.5 and 2.0 V at a current density of 1 C; (b) Rate capability from 1 to 20 C; (c) Long-term cycle life over 10,000 cycles at a current rate of 10 C.

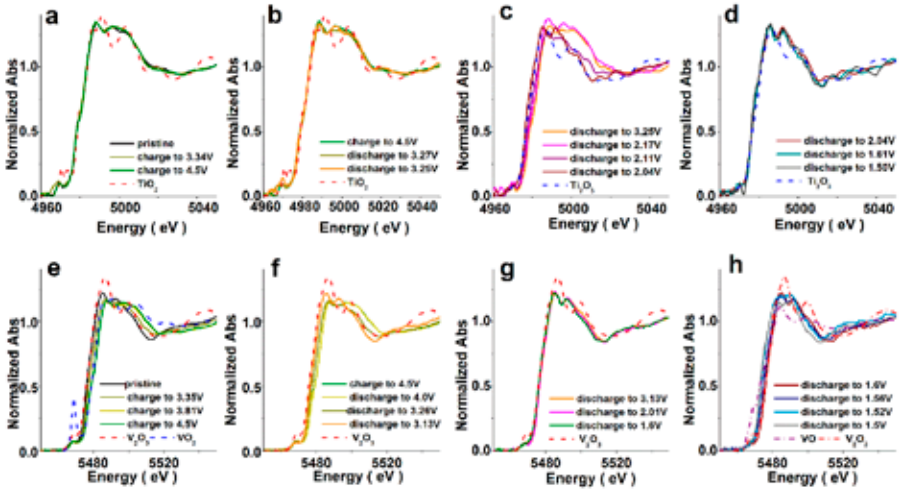

Figure 21: Charge compensation mechanism: *in-situ* X-ray absorption near-edge structure (XANES) for Ti K-edge (a to d) and V K-edge (e to h).

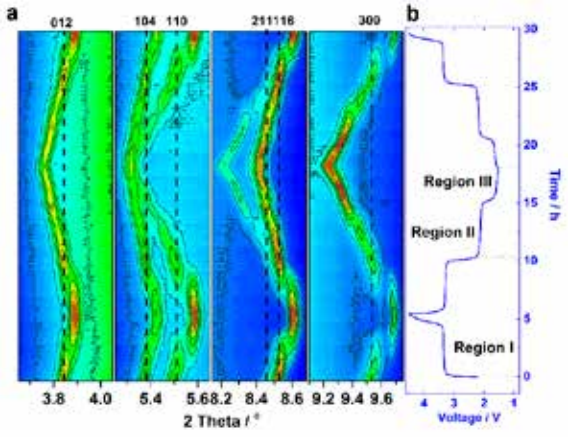

Figure 20: Structure evolution upon Na^+ extraction/insertion: (a) Contour maps of *in-situ* synchrotron XRD collected during the first charge-discharge and subsequent charge process of the Na/$Na_2VTi(PO_4)_3$@carbon cell under a current rate of C/10 in a voltage range between 1.5 and 4.5 V (b).

ACKNOWLEDGEMENTS

This work was supported by funding from "973" project (2015CB251103), National Nature Science Foundation of China (Grant Nos. 51472104 and 51572107) and the Thousand Talents Program (China). This work has benefited from BL04-MSPD beamline at ALBA Synchrotron and the collaboration with ALBA staff. Authors acknowledge DESY for beam time allocation and Edmund Welter as the beamline scientist at the P65 beamline at PETRA III in Hamburg for support. Authors also thank Prof. Yury Gogotsi, Prof. Yutaka Ueda and Dr. Angelina Sarapulova for helpful discussions. Dr. Cédric Tassel is gratefully acknowledged for his help in the Rietveld refinement analysis. Q.F. acknowledges a research scholarship from the Ministry of Science, Research and the Arts of Baden-Württemberg (MWK) in the frame of the competence network "Functional nanostructures".

AFFILIATION:

1. Key Laboratory of Physics and Technology for Advanced Batteries (Ministry of Education), State Key Laboratory of Superhard Materials, College of Physics, Jilin University, Changchun 130012, China.
2. Institute for Applied Materials (IAM), Karlsruhe Institute of Technology (KIT), D-76344 Eggenstein-Leopoldshafen, Germany.
3. Key Laboratory for Renewable Energy, Beijing Key Laboratory for New Energy Materials and Devices, Beijing National Laboratory for Condensed Matter Physics, Institute of Physics, Chinese Academy of Sciences, Beijing 100190, China.
4. ALBA Synchrotron, E-08290 Cerdanyola del Valles, Barcelona, Spain.

Visualizing Sodium-Oxygen battery discharge products using transmission X-ray microscopy

Architecture of Na-O2 battery deposits revealed by transmission X-ray microscopy.
***Nano Energy* 37 224–231 (2017)**

Imanol Landa-Medrano[1,2], Andrea Sorrentino[3], Lorenzo Stievano[4,5], Idoia Ruiz de Larramendi[1], Eva Pereiro[3], Luis Lezama[1], Teófilo Rojo[1,6], Dino Tonti[2]

The discharge products of Na-Oxygen batteries were analyzed by energy-dependent transmission X-ray microscopy at the Mistral beamline. The technique allows distinguishing at the nanoscale between different regions of the deposits formed, according to the quantity and the chemical state of the oxygen present.

The search for the next-generation batteries has recently focused on rechargeable metal-oxygen batteries, considered very attractive for their high theoretical energy densities (comparable to gasoline) for application in electrical vehicles. These batteries form oxides during the discharging process, which then –ideally- decompose into the metal ions and oxygen when charging. Lithium-oxygen systems have been largely studied since 2006; in these batteries, lithium peroxide (Li_2O_2) is formed when discharging. Recent studies found that this compound partially reacts with the electrolyte forming solid products that are difficult to remove and hinder its decomposition. As a consequence, the battery capacity fades within a few cycles. Sodium-oxygen batteries, first reported in 2012, can be an interesting alternative given the earth-abundancy of sodium, and especially because they often show a more attractive cycle life. Most authors report that no sodium peroxide (Na_2O_2) is formed during the discharge process; instead, sodium superoxide (NaO_2) is formed. This compound only forms in a one-electron transfer step and is believed to decompose more easily upon charging [1-7]. The objective of the present study was to inspect these discharge products with a spectromicroscopic technique that would reveal its composition and homogeneity.

Carbon-coated Au TEM grids after electrochemical test were stored in Ar-filled glove box and washed with DME and hexane to remove the electrolyte before characterization. Electrodes were analyzed by full-field transmission soft X-ray microscopy (TXM). The energy-resolved full-field synchrotron transmission soft X-ray microscopy was performed at ALBA's MISTRAL beamline [8]. It provides a unique access to the chemical state, spatial distribution and morphology at a single particle scale of the oxygen-based discharge products of the sample with a spatial resolution of a few tens of nanometers. Representative regions of the samples were selected from areas of 100 µm × 100 µm recorded at different zones of the sample by means of composite or "mosaic" images just at two energies, above and below the O K-edge for a first localization of oxygen compounds. On the selected areas, 2D XANES images (2 s exposure time, effective pixel size 10 nm, field of view 10 µm × 10 µm) were collected from 525 eV to 560 eV, varying the energy across the O K-edge with a spectral sampling between 0.4 eV and 0.15 eV. The objective zone plate lens and the CCD detector

positions were automatically adjusted to maintain the sample in focus and constant magnification. In this way, we have obtained 2D maps of the oxygen chemical state of the principal possible reaction products involved, with a full XANES spectrum at each pixel. The total acquisition time necessary to acquire a full XANES TXM spectrum was about 1 h, including the flat field acquisition at each energy step. The samples were transferred under N2 gas to minimize atmospheric contamination and kept in the MISTRAL microscope in cryogenic condition (T < 110 K) during all the measurements. Two particles with the characteristic external cubic shape from two different samples were completely characterized using the described technique: a fully discharged particle and a fully discharged and partially recharged particle. Composition was locally determined by the intensity of the different components in the pre-edge region [9]. A complementary view of the measured chemical composition profiles was also obtained using the Principal Components Analysis and the Multivariate Curve Resolution-Alternating Least Squares chemo-metric tools [10,11].

The performed measurements have allowed the scientists to distinguish between different regions inside the typically described cubic-shaped deposits depending on the absorption recorded for the oxygen reduction reaction (ORR) and oxygen side products (OSP) as shown in figure 22 for the fully discharged particle. A thin O-deficient layer encloses these cubes as a result of O_2 loss, indicating the instability of these deposits. In addition, scientists also observed an external layer containing secondary products (likely carbonates) in the electrolyte/deposit interface. The solution-mediated oxidation of the cubes during the charge reaction was demonstrated by the appearance of a gap between the inner cube and the enclosing secondary product shell in the partially recharged cube. Nevertheless, none of these components were detected after six complete galvanostatic cycles, demonstrating that oxidation during charging is

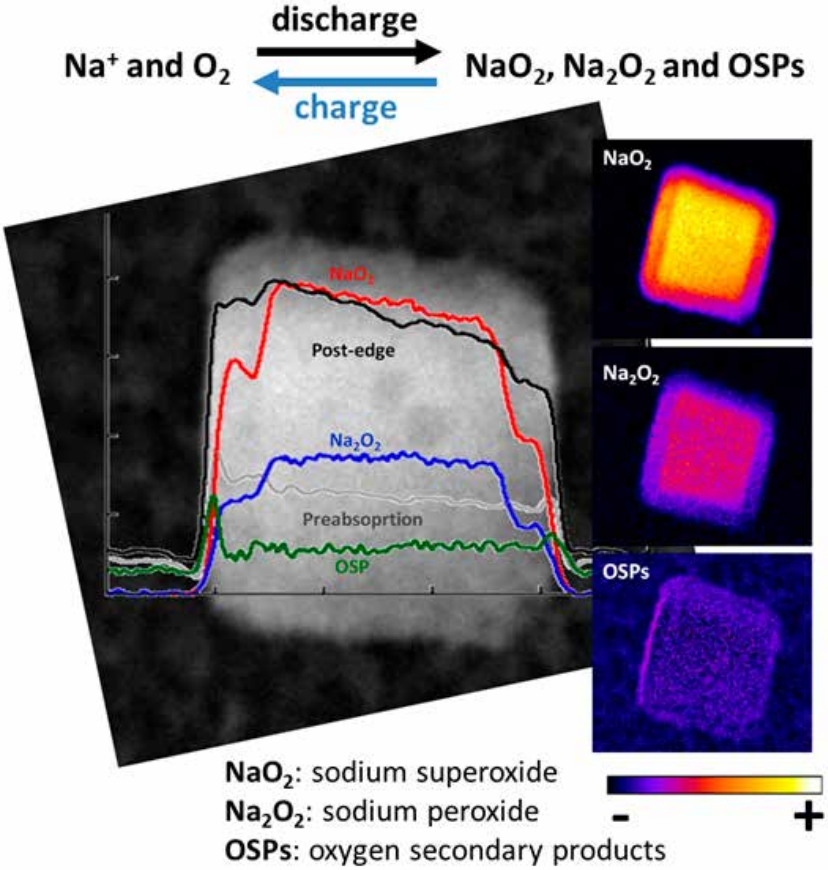

Figure 22: Left: concentration profiles of the different compounds along the discharge product (cubic-shaped) of a sodium-oxygen battery. Right: maps of oxygen distribution. The scale represents the fraction of oxygen in each of the main chemical forms found in the cubic-shaped deposits.

effective in eventually removing these deposits. However, since these observations indicate product dissolution and electrolyte decomposition, the researchers believe that the formation of secondary products in the discharge process and the effect of their spatial distribution deserve further studies to obtain a satisfactory long term cycle life in these batteries.

ACKNOWLEDGEMENTS

The X-ray microscopy experiments were performed at the MISTRAL beamline at ALBA Synchrotron with the collaboration of ALBA staff. Work was funded by the Spanish Ministry of Economy, Industry and Competitiveness, through the "Severo Ochoa" Programme for Centres of Excellence in R & D (SEV-2015-0496), and through projects MAT2015-68394-R, MAT2013-41128-R, MAT2016-78266-P, by the Government of Catalonia (grant 2014 SGR 1505), the European Regional Development Fund (ERDF) and the Eusko Jaurlaritza/ Gobierno Vasco (under project IT-570-13). I.L.M. thanks the University of the Basque Country (UPV/EHU) for his predoctoral and postdoctoral fellowships.

OTHER REFERENCES

1. I. Landa-Medrano, C. Li, N. Ortiz-Vitoriano, I. Ruiz de Larramendi, J. Carrasco, T. Rojo, Sodium–oxygen battery: steps toward reality, J. Phys. Chem. Lett. **7** (2016)1161–1166.

2. E. Peled, D. Golodnitsky, H. Mazor, M. Goor, S. Avshalomov, Parameter analysis of a practical lithium- and sodium-air electric vehicle battery, J. Power Sources **196** (2011) 6835–6840.

3. H. Yadegari, Q. Sun, X. Sun, Sodium-oxygen batteries: a comparative review from chemical and electrochemical fundamentals to future perspective, Adv. Mater. **28** (2016) 7065–7093.

4. C.L. Bender, D. Schröder, R. Pinedo, P. Adelhelm, J. Janek, One- or two-electron transfer? The ambiguous nature of the discharge products in sodium–oxygen batteries, Angew. Chem. Int. Ed. **55** (2016) 4640–4649.

5. J. Kim, H. Park, B. Lee, W.M. Seong, H.-D. Lim, Y. Bae, H. Kim, W.K. Kim, K.H. Ryu, K. Kang, Dissolution and ionization of sodium superoxide in sodium–oxygen batteries, Nat. Commun. **7** (2016) 10670.

6. D. Schröder, C.L. Bender, R. Pinedo, W. Bartuli, M.G. Schwab, Z. Tomović,J. Janek, How to control the discharge product in sodium-oxygen batteries:proposing novel pathways for sodium peroxide formation, Energy Technol. 2017).http://dx.doi.org/10.1002/ente.201600539.

7. I.M. Aldous, L.J. Hardwick, Solvent-mediated control of the electrochemical discharge products of non-aqueous sodium–oxygen electrochemistry, Angew.Chem. **128** (2016) 8394–8397.

8. E. Pereiro, J. Nicolas, S. Ferrer, M. Howells, A soft X-ray beamline for transmission X-ray microscopy at ALBA, J. Synchrotron Radiat. **16** (2009) 505–512.

9 D. Tonti, M. Olivares-Marín, A. Sorrentino and E. Pereiro, "Studies of Lithium-Oxygen Battery Electrodes by Energy-Dependent Full-Field Transmission Soft X-Ray Microscopy" in *X-ray Characterization of Nanostructured Energy Materials by Synchrotron Radiation*, eds. M. Khodaei and L. Petaccia, InTech, 2017, DOI: 10.5772/66978.

10. J. Jaumot, A. de Juan, R. Tauler, MCR-ALS GUI 2.0: new features and applications, Chemom. Intell. Lab. **140** (2015) 1–12.

11. C. Ruckebusch, L. Blanchet, Multivariate curve resolution: a review of advanced and tailored applications and challenges, Anal. Chim. Acta **765** (2013) 28–36

AFFILIATION:

1. Department of Inorganic Chemistry, Faculty of Science and Technology, University of the Basque Country (UPV/EHU), Barrio Sarriena s/n, 48940 Leioa, Bizkaia, Spain. Present address: BCMaterials, Parque Científico y Tecnológico de Bizkaia, 48160 Derio, Bizkaia, Spain.

2. Institute of Materials Science of Barcelona, National Research Centre (ICMAB-CSIC), Campus UAB, Bellaterra, Barcelona, Spain.

3. ALBA Synchrotron, Cerdanyola del Vallès, Barcelona, Spain.

4. Institute Charles Gerhardt Montpellier UMR CNRS 5253, Univ. Montpellier, 34095 Montpellier Cedex 5, France.

5. Network for Electrochemical Storage of Energy (RS2E), FR CNRS 3459, 33 rue Saint Leu, 80039 Amiens, France.

6. CIC EnergiGUNE, Albert Einstein 48, 0150 Miñano, Spain.

SCIENTIFIC RESULTS
CATALYSIS

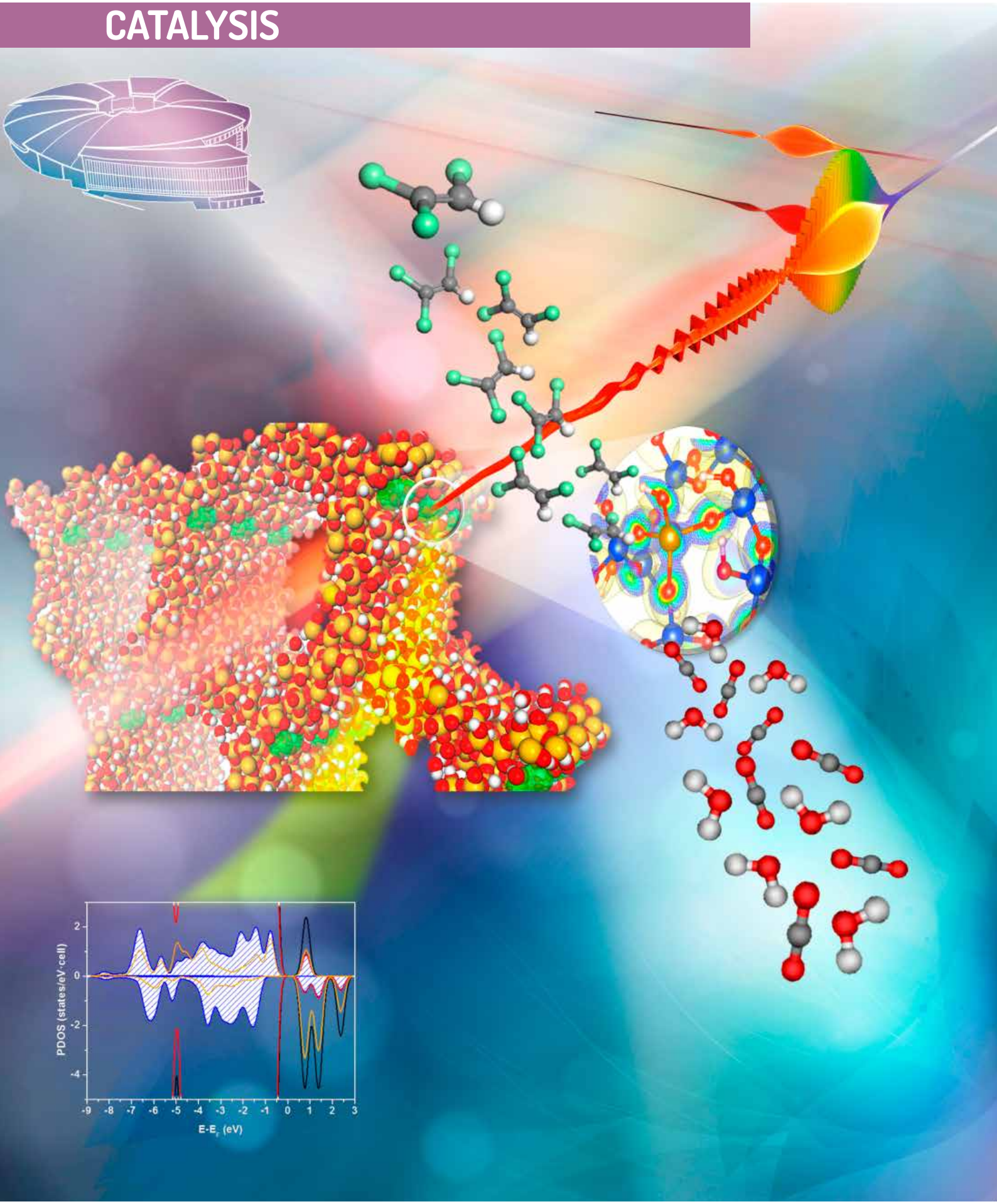

Courtesy of Victor de la Peña O'Shea

Unraveling the Photoredox Nature Isolated Iron Active Sites for Volatile Organic Compound Remediation

Elucidating the Photoredox Nature of Isolated Iron Active Sites on MCM-41.
***ACS Catalysis* 7 (3), 1646−1654 (2017)**

Laura Collado[1,2] Ingrid Jansson[3], Ana E. Platero-Prats[4], Virginia Perez-Dieste[5], Carlos Escudero[5],Elies Molins[6], Lluis Casas i Doucastela[7], Benigno Sanchez [3], Juan M. Coronado[2], David P. Serrano[2,8], Silvia Suarez [3], Victor A. de la Peña-O'Shea[1]*

Effect of optoelectronic properties, determined by NEXAFS, in the reaction mechanism of Fe- doped meso structured SiO_2 (MCM-41), as a highly efficient photoredox catalyst for VOCs remediation.

Solar-energy conversion is one of the most important challenges of this century [1]. Photocatalytic processes allow to perform: elimination of water and air pollutants, bacteria disinfection and production of fuels and high added value chemicals by artificial photosynthesis, without the concourse of elevated temperatures using (sun)light as the unique energy input.

Exposure to air pollution is the fifth ranking human health risk factor globally [2]. Organic aerosols from oxidation of volatile organic compound (VOCs) are the major component of fine particulate matter in cities [3]. In addition, VOCs oxidation in the presence of nitrogen oxides leads to an increase of tropospheric ozone, increasing the mortality due to respiratory diseases. Therefore, the use of photocatalytic technologies will help to mitigate these environmental and health problems.

The design and development of efficient, robust and low-cost light driven materials is crucial for the achievement of industrially competitive photocatalysts. Semiconductors have been traditionally employed due to their unique optoelectronic and catalytic properties. The major drawbacks are: their low quantum yields, high recombination rates, charge transport/transfer limitations, inadequate bandgaps, photocorrosion and the use of expensive or harmful elements. A promising alternative is the development of low-cost isolated active sites photocatalysts based on abundant earth metal doping ordered silicon-mesoporous structures.

This work reports for the first time a whole draw of the mechanism that converts Fe tetrahedral single sites, incorporated into an insulating nanostructured SiO2 (MCM-41), into a very efficient photoredox catalyst. Advanced structural and optoelectronic characterization techniques were combined with theoretical calculations to truly understand the reaction pathways and intermediates involved in the photoxidation of trichloroethylene (TCE), one of the most abundant VOCs, when using isolated Fe active sites (Figure 23).

Due to the nano-nature and complexity of these materials, a combination of Mössbauer spectroscopy, theoretical calculations and PDF analysis using X-ray scattering data was used to provide detailed insights into the local structure of the single sites. All of these

techniques confirm that Fe atoms are tetrahedrally coordinated in the SiO2 framework and theoretical calculations endorse that the incorporation of Fe into an insulator matrix leads to significant changes in the electronic structure, which are intriguingly linked to the geometrical conformation and environment of the active site and will determine the photocatalytic behavior. However, it is necessary to use spectroscopic techniques such as Near Edge X-ray Absorption Fine Structure (NEXAFS) combined with Time dependent density functional theory (TD-DFT) calculations to explain the optoelectronic effect in this reaction.

NEXAFS spectra were recorded at the CIRCE beamline of ALBA Synchrotron in total electron yield mode. The beamline resolving power is E/ΔE=8000 (ie. ΔE=83 meV for the Fe L-edge). NEXAFS experiments under illumination were conducted using a UV-LED source with an emission wavelength centered at 365 nm. These studies confirm the photoreduction of iron by charge-transfer (CT) processes. Under dark conditions, the Fe LIII-edge of an iron-based (Fe-20) sample is dominated by dipole allowed 2p-3d transitions, as evidenced by the broad band centered at ~711 eV with a shoulder at ~710 eV. These contributions are associated with t2 and e orbitals of high-spin Fe3+ species in a tetrahedral coordination with a crystal field splitting of ~0.9 eV.

Under UV illumination (Figure 25B), the broadening of the bands suggests the existence of a new contribution at lower energy (708.3 eV), assigned to the presence of iron species with higher electron density (Feδ+). This suggests the photo-reduction of Fe3+ species through LMCT processes, as is also corroborated by TD-DFT calculations (Figure 24).

The combination of these unusual structural and optoelectronic properties leads to high yield of TCE conversion. This result indicates a higher interaction of TCE with iron active sites that favors the oxidation processes, through the LMCT induced by light (NEXAFS) that enables the photo-generation of localized charges within the Fe site, as well as the formation of hydroxyl radicals (OH▪). The hole injection converts the Fe-OH▪ into a Fe=O transition state leading an unsaturated Fe site which is oxidized to the starting point (Figure 25).

As a result of both experiments and theoretical calculations, it is clear that isolated tetrahedral iron sites have unique textural, structural and optoelectronic properties and excellent stability, which result in high TCE photoxidation rates. This is the first study that establishes a photo-oxidation mechanism for isolated active sites, including intermediates and excited states. This reaction mechanism is based on the formation of highly reactive hydroxyl radicals that are coordinated to Fe. The first step of the photo-oxidation reaction is through LMCT processes determined by NEXAFS, and the subsequent formation of an intermediate

OTHER REFERENCES

1. Coronado, J. M.; Fresno, F.; Hernández-Alonso, M. D.; Portela,R. Design of Advanced Photocatalytic Materials for Energy and Environmental Applications, Springer Verlag London, 2013.

2. Current challenges of CO2 photocatalytic reduction over semiconductors using sunlight" (2015 pp. 171-191) by De La Peña O'Shea, V.A., Serrano, D.P., Coronado, J.M. From Molecules to Materials: Pathways to Artificial Photosynthesis ISBN: 978-331913800-8; 978-331913799-5 Springer, Ed E. A. Rozhkova, K. Ariga.

3. GBD 2016 Risk Factors Collaborators, Lancet **390**, 1345–1422 (2017).

4. McDonald et al., Science **359**, 760–764 (2018)

ACKNOWLEDGEMENTS

L.C. thanks funding from the FPI grant (BES-2010-032400). I.J, B.S and S.S acknowledge financial support from the Spanish Ministry of Economy and Competitiveness through the project (CTM2011-25093) and V.A.P.O. to SolarFuel (ENE2014-55071- JIN). A.E.P.P. acknowledges a Beatriu de Pinos fellowship (BP-DGR-2014) from the Agency for Management of University and Research Grants (Government of Catalonia). V.A.P.O. acknowledges support from the Centre of Supercomputing Centre of Catalonia (CESCA) and to ALBA Synchrotron facility. This work has been developed under the HyMAP project (ERC-CoG).

AFFILIATION:

1. Photoactivated Processes Unit, Institute IMDEA Energy, Avda. Ramon de la Sagra 3, 28935 Mostoles, Spain.
2. Thermochemical Processes Unit, Institute IMDEA Energy, Avda. Ramon de la Sagra 3, 28935 Mostoles, Spain.
3. Photocatalytic Treatment of Pollutants in Air FOTOAIR-CIEMAT, Avenida Complutense, 22, 28040 Madrid, Spain.
4. X-ray Science Division, Advanced Photon Source, Argonne National Laboratory, 60439 Argonne, USA.
5. ALBA Synchrotron, Carrer de la Llum 2-26, 08290 Cerdanyola del Valles, Spain.
6. Institute of Materials Science of Barcelona (ICMAB-CSIC), 08193 Bellaterra, Spain.
7. Departament of Geology, UAB, 08193 Bellaterra, Spain.
8. Department of Chemical and Environmental Engineering Group, URJC, C/ Tulipan, 28933 Mostoles, Spain.

Fe=O state through hole injection. Afterwards, unsaturated Fe- sites are re-oxidized by O2 forming superoxide species. The existence of this intermediate step and the low metal density explain the high yield of intermediate oxidation products. These results provide a better understanding of the reactivity and the charge transfer processes (NEXAFS) in single site based photocatalysts and intermediate species. This information may be critical to develop a more rational design of these materials. Authors hope that the findings presented here would open new possibilities in the use of these low-cost and environmentally friendly photocatalysts in other light-mediated reactions such as CO2 reduction, water splitting or remediation of air and/or water contaminants.

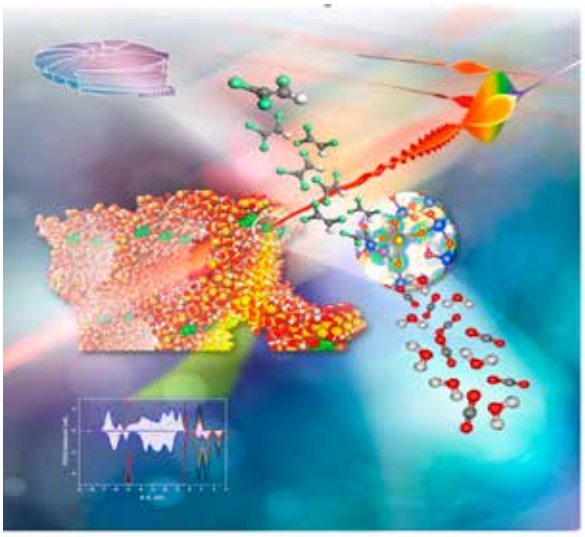

Figure 23: Combination of advanced characterization tools and theoretical calculation to draw the effect of photoredox nature of Fe single active sites in photocatalytic VOCs elimination.

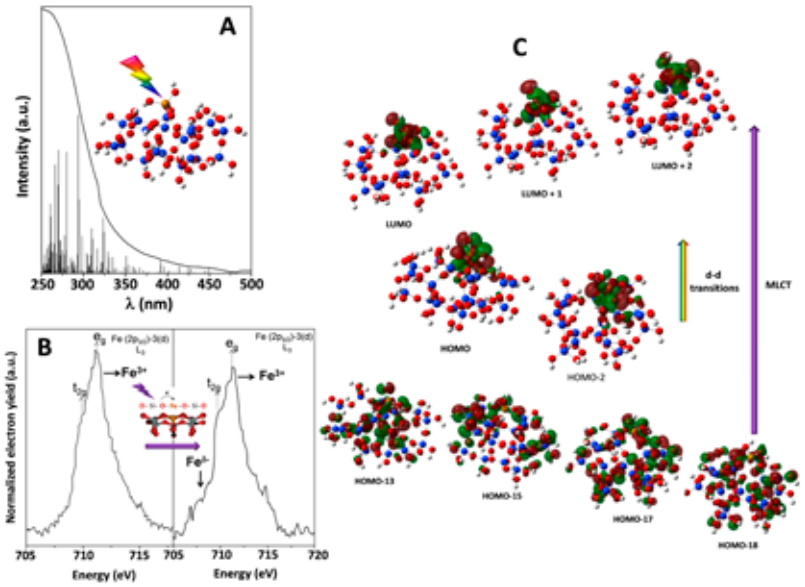

Figure 24: (A) UV–Vis spectra of Fe-20 and calculated excitation energies (vertical bars) for A-Fe, B-Fe and C-Fe sites. Calculated transitions are slightly shifted to higher wavelengths, because DFT underestimate absorption energies, giving LUMO energies which are far too stable; (B) Fe L-edge NEXAFS spectra of Fe-20 in the dark (left) and under UV illumination (right) and (C) selected molecular orbitals contributing to d-d (visible) and LMCT (UV) transitions for C-Fe site.

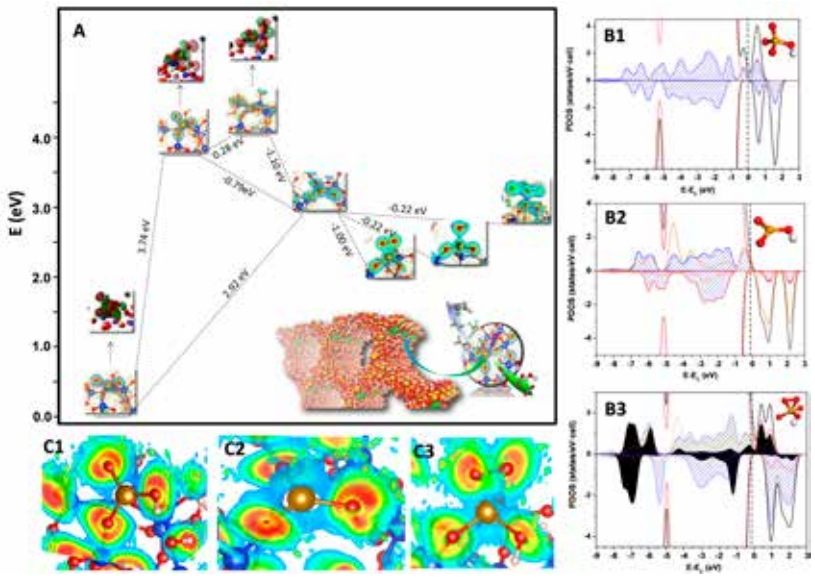

Figure 25: (A) Energy profile of proposed reaction pathways and schematic representation of charge density isosurfaces (inset); Total DOS (black) and atom-projected DOS (PDOS) for (B1) C-site(TS), (B1) C-site(OU*) and (B3) superoxide formation, where Fe (orange line), total O (red line), O neighboring to Fe (blue dash), and O form superoxide specie (black filled). Electron localization function for same reaction centers are also depicted (C1-C3).

Exploring the CO oxidation activity of catalysts combining cobalt and cerium oxides

Nanostructured Catalysts Based on Combinations of Cobalt and Cerium Oxides for CO Oxidation and Effect of the Presence of Water. *Journal of Nanoscience and Nanotechnology* 17, 3816-3823 (2017)

C. L. Bolívar-Díaz[1], J. C. Conesa[1], V. Cortés Corberán[1], M. Monte[1], and A. Martínez-Arias[1]*

The work aims to get details about structure/activity relationships in nanostructured Co_3O_4/CeO_2 catalysts employed for CO oxidation.

The catalytic properties for oxidation of CO of nanostructured catalysts based on combinations of oxides of cobalt and cerium, which were prepared by coprecipitation within reverse microemulsions and which differ in their Co/Ce ratio, are examined in this work. The catalysts were characterized by SBET measurement, XRD, Raman spectroscopy and XPS. Their catalytic properties were examined by tests under CO–O2 or CO–O2–H2O mixtures with the aim of exploring deactivation processes taking place in the systems in the presence of water. Catalytic tests were in turn complemented by operando-DRIFTS and –XANES experiments under similar reaction conditions (Fig. 26). It is shown that the catalysts are basically constituted by combination of CeO_2 and Co_3O_4 nanostructures while a trend towards stabilization of cobalt as Co2+ appears upon increasing the interaction with ceria. It is generally evidenced that the degree of interaction between the two catalyst components can favorably affect the resistance of the systems for CO oxidation towards deactivation in the presence of water.

XAFS measurements under reaction conditions were performed on the CLÆSS beamline at the ALBA Synchrotron equipped with a Si(111) double crystal monochromator and a toroidal Rh mirror for armonic rejection. Data were collected at the Co K and Ce L3 edges in fluorescence mode using a Si solid-state detector. The sample was precalcined under oxygen diluted in inert flow at 500 ºC and then, after cooling to room temperature under the same flow, subjected to treatments under either $CO+O_2$ or $CO+O_2+H_2O$ reactant mixtures at different temperatures and under similar conditions as exposed above for the DRIFTS experiments. The energy scale was calibrated with the measurement of a cobalt foil or CeO_2 reference.

The spectra observed for the initial calcined samples are similar to that observed for pure Co_3O_4, therefore confirming cobalt is basically in that form for any of the catalysts. A subtle difference is however found between them since the maximum around 7728 eV appears sharper and slightly shifted to higher energy for the sample with highest cobalt loading, which exhibits a spectrum much closer to that expected for pure Co_3O_4. In contrast, the spectrum of the sample with lowest cobalt loading (in which the interaction with ceria becomes maximised, presents a stronger contribution from Co2+. An apparent change is observed upon first contact of the catalyst with the CO–O2 reactant mixture and is related to an increase in the absorption at ca. 7722 eV. Such change becomes more pronounced upon decreasing the cobalt content of the sample. This suggests that it must mainly be related to modifications produced in surface or interface cobalt species upon formation of complexes

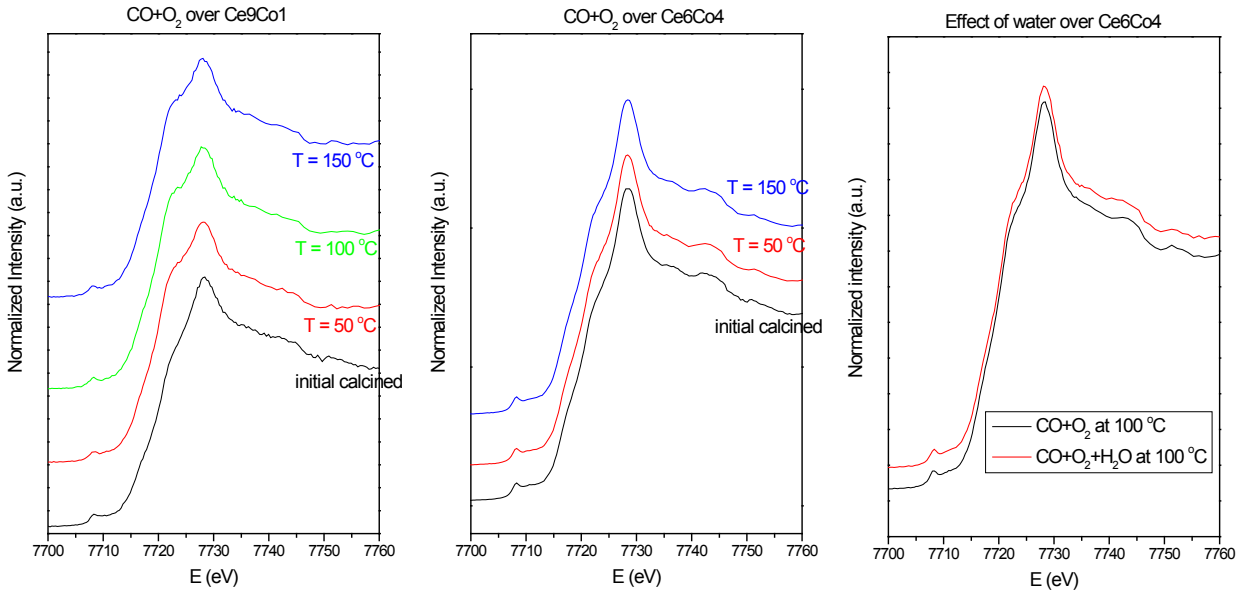

Figure 26: XANES spectra obtained for indicated catalysts under exposed conditions.

modifying the chemical environment of the cobalt cations while apparently keeping in any case a Co_3O_4-type structure in general terms and under any of the inspected reaction conditions. No important changes are observed in this sense either upon increasing the reaction temperature under CO–O2 or introducing water in the reactant mixture. The catalytic behavior of the samples is shown to be strongly dependent on the cobalt content and/or relative degree of interaction between cobalt and ceria. Basically, two reaction regions can be defined as a function of the impact that deactivation by water has on the catalyst. Below ca. 120 °C, important deactivation effects are observed while they are less apparent above such temperature. The catalyst with lower cobalt content is shown to be the one in which deactivation effects of water can be minimized. Since this catalyst is the one in which the contact of nano-cobalt oxide and (Co-doped) CeO_2 becomes maximized, it can be concluded that the interaction between cobalt and CeO_2 results beneficial for decreasing deactivating effects of water in this type of catalysts.

AFFILIATION:
1. Institute of Catalysis and Petrochemistry. CSIC. C/ Marie Curie 2. Campus de Cantoblanco, 28049 Madrid, Spain.

Using XAS and XPS to identify a surface cobalt carbide phase as catalytic sites for ethanol dehydrogenation

Cobalt Carbide Identified as Catalytic Site for the Dehydrogenation of Ethanol to Acetaldehyde. *ACS Catalysis* 7, 5243-5247 (2017)

Alberto Rodriguez-Gomez[1,2], Juan P. Holgado[1,2] and Alfonso Caballero[1,2]

Under ethanol reforming reaction conditions, Co/SBA-15 catalysts developed a surface cobalt carbide phase which enhances the dehydrogenation activity of ethanol to acetaldehyde.

The growing interest in reducing the impact of fossil fuels in the environment has promoted the use of hydrogen as an energy carrier, even though the current technology for hydrogen production is not economically competitive [1]. Currently, most hydrogen is obtained from steam reforming of methane, although its production from renewable sources, mainly bioethanol, has been proposed as a promising route [2]. In this way, hydrogen can be obtained by the steam reforming reaction of ethanol (ESR). Although this is the main desired reaction, depending on the catalyst and reaction conditions, many other side reactions can occur, yielding different undesirable chemicals. Cobalt has appeared as a high-performance catalytic system, although activity and selectivity to desirable and undesirable products are strongly dependent on factors such as the support or the dispersion state of the metal, and the chemical state of cobalt under ESR conditions is still controversial [3]. The catalytic site for acetaldehyde production is another point of controversy, as oxidized or reduced cobalt has been proposed as catalytic sites [4].

Authors have prepared two cobalt catalysts supported on SBA-15 and a high surface SiO_2, which have been characterized under reduction and ESR conditions. The catalytic performances in the ESR reaction were measured at 500 ºC. The Co/SBA-15 catalyst shows an ethanol conversion of 88.6% while the Co/SiO_2 only has 57.6%. Co/SiO_2 selectivity to acetaldehyde reaches a value of 28.8%, rising to 43.5% in Co/SBA-15, revealing a high dehydrogenation activity of both catalysts. As reforming and dehydrogenation to acetaldehyde reactions are antagonistic, the catalytic sites of cobalt responsible for both reactions must have a different nature. In order to elucidate the chemical and physical nature of these two cobalt catalytic sites, authors have accomplished a characterization work of these two systems after calcination, reduction and SRE reaction conditions. The XANES and F.T. of Co/SBA-15 after reduction at 750 ºC (Figure 27) indicate the presence of reduced cobalt, with a mean coordination number of 11.0. Under ESR reaction conditions no noticeable changes can be detected by XAS spectroscopy. However, the TEM images (Figure 28) suggest that cobalt particles are strongly modified during SRE reaction, especially in the Co/SBA-15 catalyst. Figure 29 shows the Co2p region of XPS obtained in situ for both catalytic systems reduced at 750 ºC and after ESR reaction at 500 ºC. After reduction both systems present a metallic phase (778.0 eV), while under ESR reaction conditions the main Co2p peak is widened and shifted to lower binding energies, meaning that cobalt is transformed into a new more reduced state, shift more significant in the SBA-15 catalyst, which can be adjusted with 70% metallic cobalt and 30% of a new cobalt phase, while in the Co/

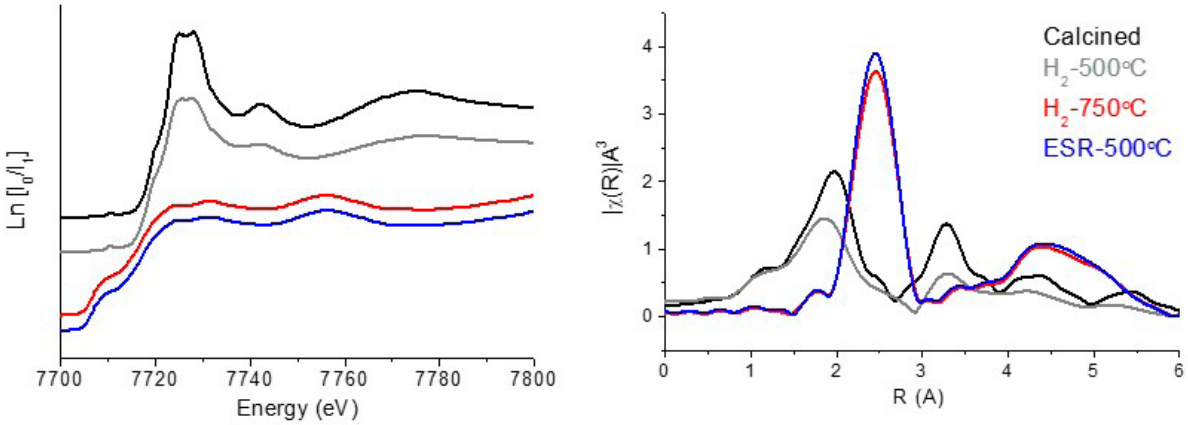

Figure 27: Co K-edge XANES spectra and F.T. of Co/SBA-15 after different treatments.

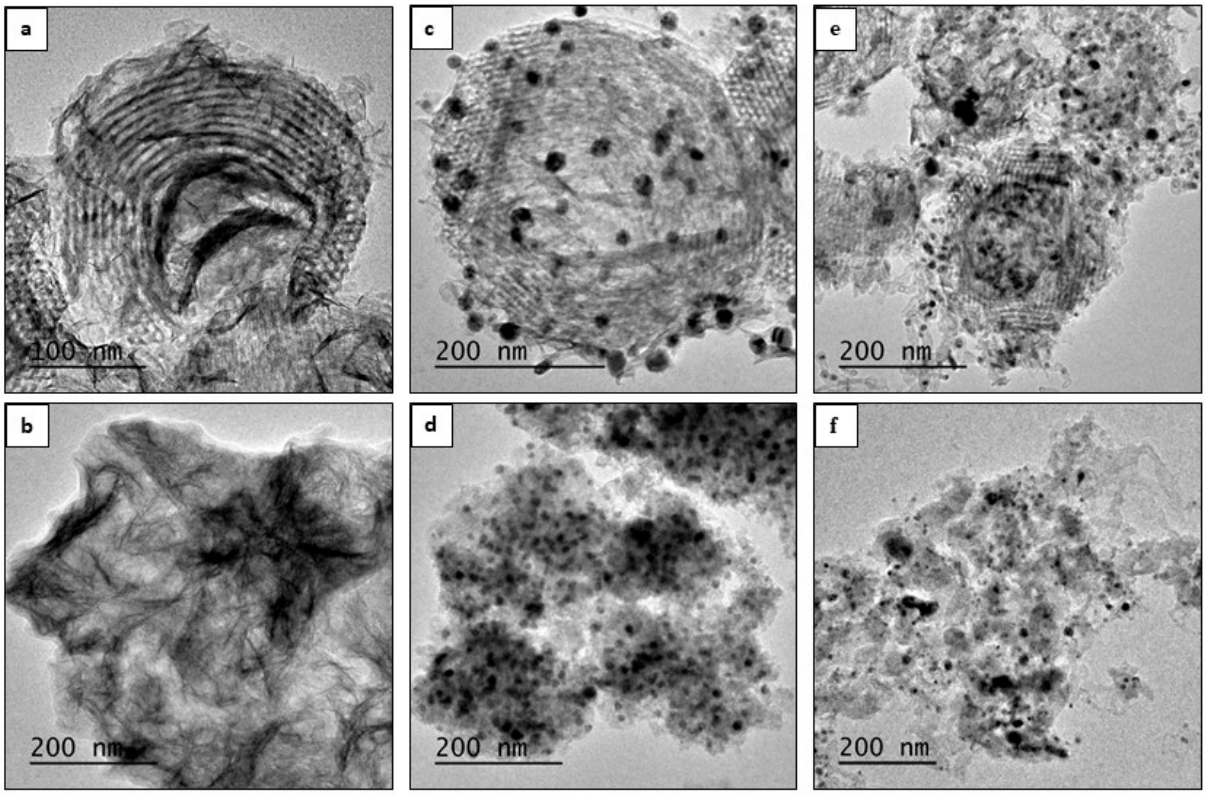

Figure 28: TEM images of Co/SBA-15 (top) and Co/SiO_2 (bottom) after calcination (a-b), reduction (c-d) and ESR reaction (e-f).

SiO_2 system the peak is adjusted with 82% and 18%, respectively. A peak in such a low energy position has been previously ascribed to a cobalt carbide phase [5], which agrees with other results from XRD. The fact that this phase has been clearly detected by XPS upon ESR treatment but is undetectable by XAS (Figure 27), may be an indication that this carbide phase must be located just on the surface of the metallic cobalt particles. According to previous DFT calculations [6], the formation of cobalt carbide is exothermic with respect to Co under the presence of a CO and H_2 mixture. Considering that under SRE conditions a syngas mixture is produced, these facts support the experimental findings that a carbide phase is formed under ESR conditions but only on the surface of the metallic particles. DFT studies [6] also demonstrated the strong metallic-like character of the cobalt carbide, but with a variety of low index planes exposed, which modifies the metallic character of the Co-C bond.

In conclusion, authors have demonstrated that, under ESR reaction conditions, an initially well-reduced Co phase is partially transformed into a surface cobalt carbide phase, coexisting metallic and carbide cobalt in different proportions (70:30 for Co/

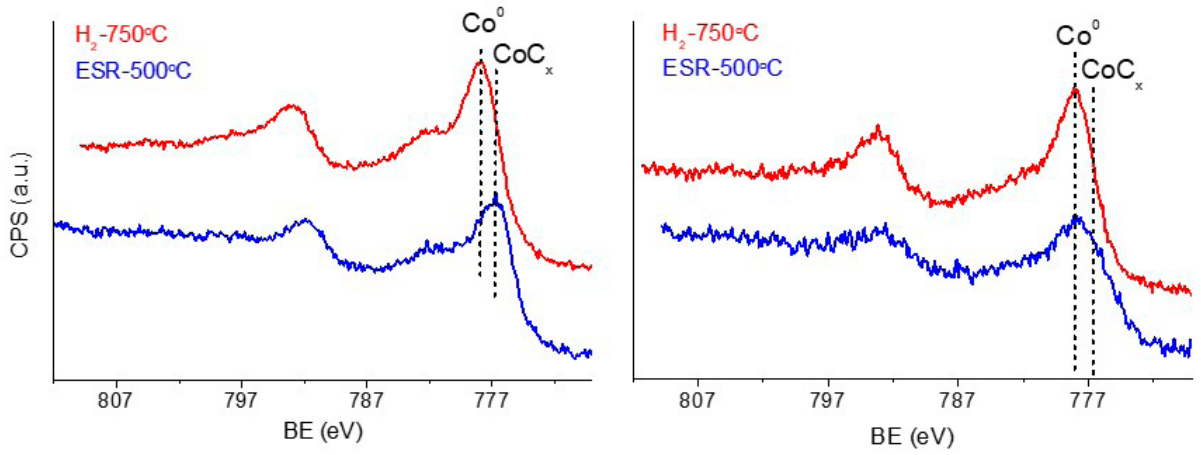

Figure 29: Co2p region XPS spectra of Co/SBA-15 (left) and Co/SiO_2 (right) after the indicated *in-situ* experiments.

SBA-15 and 82:18 for Co/SiO_2), as determined by XPS. Considering the different catalytic selectivity of these two catalysts, the production of CO and CO_2 comes from the steam reforming of ethanol reaction, which occurs over catalytic sites of metallic cobalt, proportionately more abundant in the Co/SiO_2 catalyst. In the same way, the higher productivity of acetaldehyde with the Co/SBA-15 catalyst correlates with the higher amount of carbide phase detected in this system, which is achieved by dehydrogenation of the ethoxide groups adsorbed on cobalt carbide sites. At the same time, the subsequent breakage of the C–C bond to generate the reforming products is not catalyzed on the cobalt carbide sites. This interpretation is also supported by the well-known activity in hydrogenation–dehydrogenation reactions of transition-metal carbides, but also in homogeneous reactions with different types of organometallic compounds.

ACKNOWLEDGEMENTS

Authors thank the Ministry of Economy and Competitiveness of Spain (Project Nos. ENE2011-24412 and CTQ2014-60524-R) and the ALBA facility and staff (BL22 CLÆSS beamline) for their experimental support. A.R.G. also thanks the Spanish Government for the PhD fellowship (No. BES-2012-061744).

OTHER REFERENCES

1. International Energy Agency. World Energy Outlook 2008; IEA Publications: Paris, 2008.
2. Renewable Sustainable Energy Rev. 2010, **14**, 166–182.
3. ACS Catal. 2014, **4**, 1205–1218.
4. ACS Catal. 2011, **1**, 1414–1420.
5. Thin Solid Films 2005, **485**, 95–100.
6. Surf. Sci. 2012, **606**, 598–604.

AFFILIATION:

1. Institute of Materials Science of Seville (CSIC-University of Seville).
2. Department of Inorganic Chemistry, University of Seville. Av. Americo Vespucio, 49, 41092 Seville, Spain.

MAGNETISM & SUPERCONDUCTIVITY

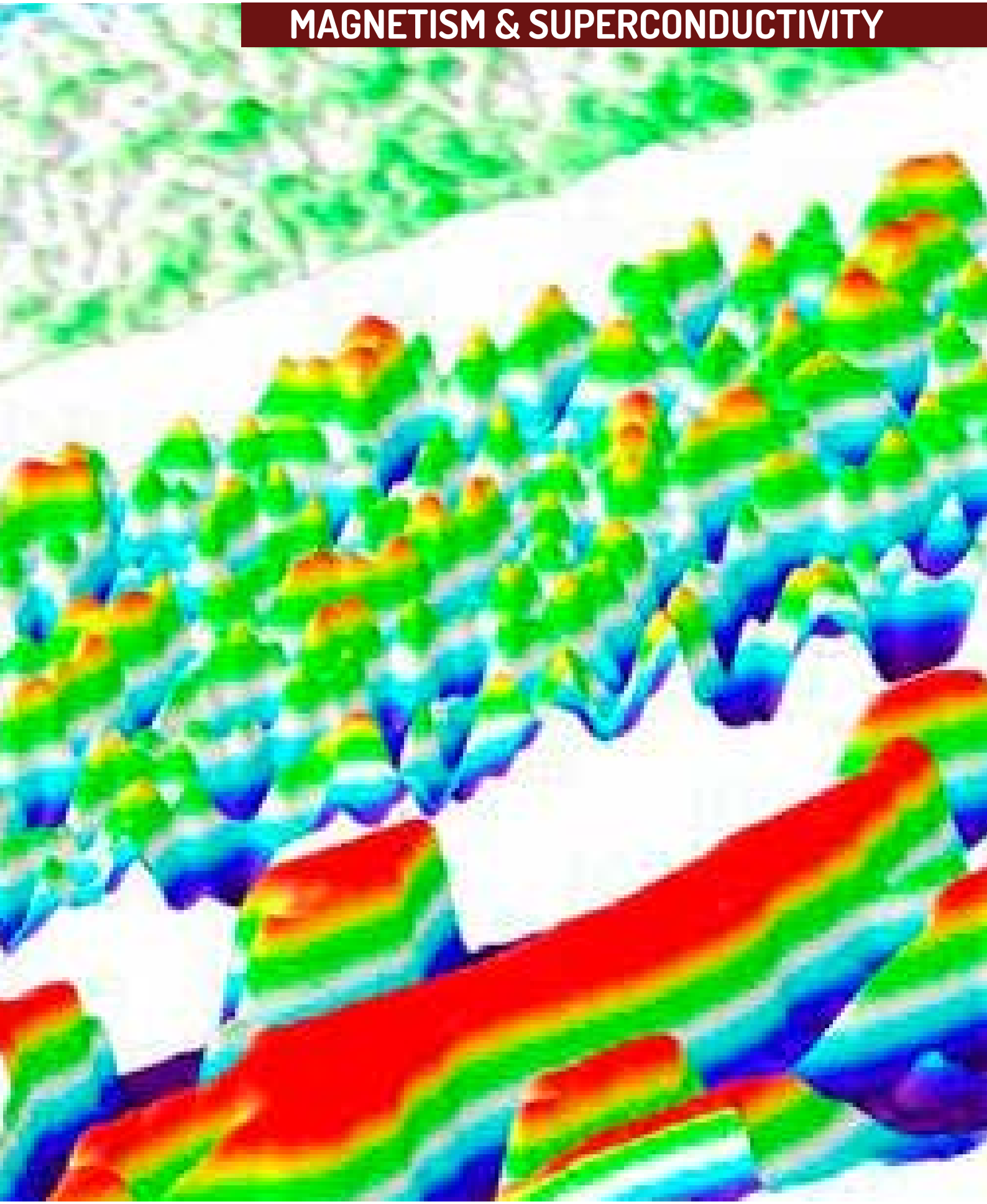

Courtesy of Ignasi Fina.

Sign Control of Magnetoresistance in Spin Valves Based on Novel Lanthanide Quinoline Molecules

Interface-Assisted Sign Inversion of Magnetoresistance in Spin Valves Based on Novel Lanthanide Quinoline Molecules. *Adv. Funct. Mater.* (2017)

Amilcar Bedoya-Pinto[1], Sara G. Miralles[2], Saül Vélez[1], Ainhoa Atxabal[1], Pierluigi Gargiani[3], Manuel Valvidares[3], Fèlix Casanova[1,4], Eugenio Coronado[2] and Luis. E. Hueso [1,4]

This study demonstrates how the atomic interaction at metal-molecule interfaces is used to engineer macroscopic output parameters in a molecular spintronic device. Combining magnetotransport and *in-situ* X-ray absorption spectroscopy experiments, it is shown that specific metal-molecule hybrid states fully govern the interface spin polarization, thus controlling both sign and magnitude of the magnetoresistance in a fully-functional molecular spin valve.

Molecules, due to their wide-ranging chemical functionalities that can be tailored on demand, are becoming increasingly attractive components for applications in materials science and solid-state physics. Remarkable progress has been made in the fields of molecular-based electronics and opto-electronics, with devices such as organic field-effect transistors (OFETs) and light-emitting diodes (OLEDs). As for spintronics, a nascent field which aims to use the spin of the electron for information processing, molecules have been proposed to be an efficient medium to host spin-polarized carriers due to their weak spin relaxation mechanisms.[1]. Recently, the research focus in this discipline has been set in using the chemical versatility of molecules to achieve a deterministic control and manipulation of the electron spin [2]. Significant progress has been made by controlling and reading spins at the single-molecule level [3], but such a degree of control has not yet been implemented in large-area functional device architectures. In this work, authors demonstrate the control of the magnetoresistance in a fully functional molecular spin-valve system based on NaDyClq, a novel mononuclear quinoline molecule, combined with Cobalt and Permalloy as spin injector and detector electrodes. The sign change of the magnetoresistance is linked to the formation of specific hybrid electronic states at the molecular/ferromagnetic interface, as evidenced by X-ray absorption spectroscopy.

The key feature of this study was to combine magneto-transport experiments in multi-layered hybrid spin-valve devices with a rigorous in-situ X-ray absorption spectroscopy of the metal-molecule interfaces that are found to be relevant to modulate the device output.

The spin valve stack was entirely fabricated in an ultra-high-vaccum chamber, employing a novel lanthanide quinoline molecule as spin transporting layer (Fig. 30a), and Cobalt (Co) and Permalloy (Py) as ferromagnetic injector/detector electrodes (Fig. 30b). Contrary to other Co/AlOx/molecule/Py spin valve systems, the Co/AlOx/NaDyClq/Py devices exhibit negative magnetoresistance (Fig. 31a), evidencing a negative spin polarization at the NaDyClq/Py interface. Inverting the spin valve stack order –NiFe/AlOx/NaDyClq/Co – leads to positive magnetoresistance (Fig. 31b), which points out to a positive spin

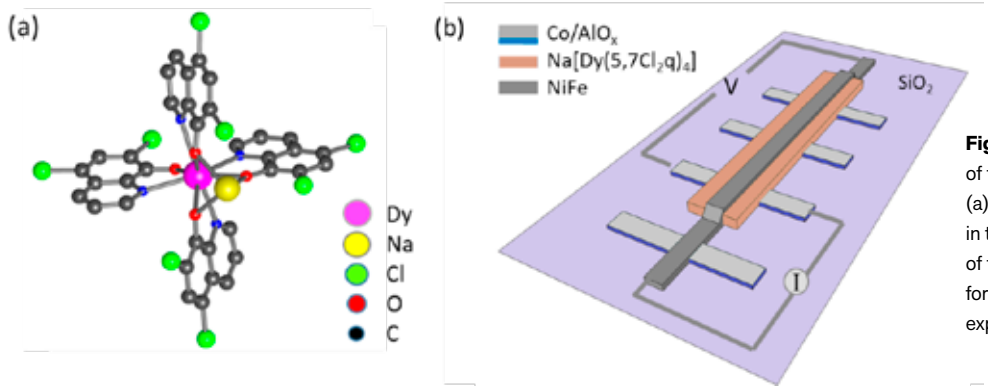

Figure 30: a) Molecular structure of the Na[Dy(5,7Cl$_2$q)$_4$] compound (a), used as a spin transport layer in the device. b) Schematic view of the device geometry employed for the magneto-transport experiments.

polarization at the NaDyClq/Co interface. These two interfaces were reproduced with exactly the same growth conditions at the preparation chamber of the HECTOR endstation at BOREAS, capable of preparing both molecular and metal layers in the same run. X-ray absorption and dichroism spectra were taken of all the elements present in the molecule *before* and *after* the deposition of the ferromagnetic layer (Fig. 32 a,b), thus being able to distinguish the fingerprints of the interaction at the metal-molecule interface. It is found that the C and N atoms at the molecular ligand sites are the ones that interact with the ferromagnetic atoms.

Figure 32 compares the normalized C *K*-edge and N *K*-edge *XAS* spectra of the NaDyClq layer before and after metal deposition, confirming that each metal surface (Py and Co) leads to a different, specific interaction with the molecular orbitals. While the Py adsorption notably modifies the carbon *K*-edge spectrum (Figs. 32a-b), Co atoms rather interact with the N-sites of the molecule, as seen in the changes of the N *K*-edge absorption spectrum (Figs. 32c-d).

In the carbon *K* edge of the pristine molecular layer, the electronic transitions belonging to both π and σ carbon orbitals can be clearly identified (Fig.32b). In the case of the π states, there are three prominent peaks (A_1-A_3), which have been previously observed in Alq_3 molecules and ascribed to the LUMO and LUMO+1 transitions localized at the carbon rings of the quinolinolate ligands [4]. Comparing the spectrum before and after deposition of Py atoms, there is a clear increase in spectral weight in the pre-edge region, especially at 280.6 ± 0.2 eV and 282.0 ± 0.3 eV (Fig. 32b). This change in the spectrum indicates electronic transitions of the core electrons to newly formed electronic states and can be understood in terms of a specific hybridization of NiFe and carbon orbitals, since the spectra of all other species of the NaDyClq molecule remain unperturbed.

In the case of Co atoms deposited onto the NaDyClq layer, the carbon K-edge spectrum displays the same features as the pristine NaDyClq molecule, whereas the N *K*-edge displays a clear new peak in the pre-edge region at 397.1 ± 0.1 eV (Figure 31c and 31d), in addition to the well-known transitions of the π (C_1) and **σ** (C_2,C_3) orbitals. Once again, the interaction of Co is found to be specific to the nitrogen atoms of the quinoline molecule. Interestingly, these states present a clear linear dichroism, feature which is not

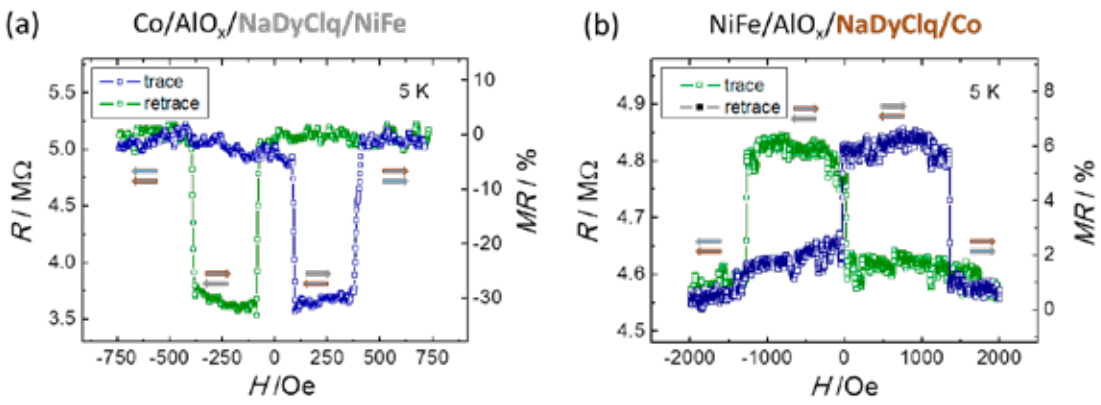

Figure 31: Magnetotransport measurements in NaDyClq spin valves and the role of the metal-molecule interface. a) Negative *TMR* measured at 5 K and -10 mV in a Co/AlO$_x$/NaDyClq/NiFe spin valve. b) Positive *TMR* measured under the same conditions in a NiFe/AlO$_x$/NaDyClq/Co spin valve, highlighting the role of the top metal-molecule interface. The brown and gray arrows indicate the magnetization direction of the Co and NiFe electrodes respectively.

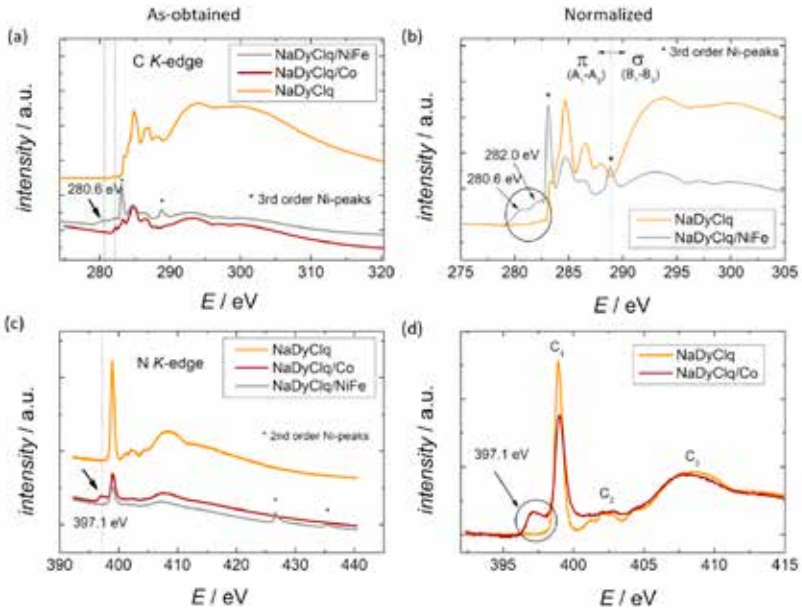

Figure 32: X-ray absorption spectroscopy of the interacting elements at the two studied metal-molecule interfaces. (a) As-obtained X-ray absorption spectra at the C K-edge, highlighting that the absorption features at 280.6 eV and 282.0 eV arise specifically at the NaDyClq/NiFe interface, while all other features are present in the pristine molecule, though with different relative intensities. (b) Normalized C K-edge spectrum highlighting the features in the pre-edge region upon NiFe deposition, in addition to the multiple transitions of the π (A1-A3) and σ (B1,B2) orbitals. (c) As-obtained N K-edge spectrum of the NaDyClq/Co interface, presenting a clear feature related to Co-N bonding states, which is not present at the NaDyClq/NiFe interface. The normalized spectrum is shown in (d), along with the known C1-C3 transitions of the N-orbitals.

present in the purely (**π,σ**) molecular states, pointing towards a geometrical orbital asymmetry originated from the Co-N hybridization process.

In summary, molecular spin-valves based on novel lanthanide-based quinolines of the form FM1/AlO_x/NaDyClq/FM2 have been investigated. As for the magnetotransport properties, the Co/AlO_x/NaDyClq/NiFe devices exhibit a negative magnetoresistance (MR), whereas swapping the NiFe and Co electrodes leads to a positive *MR* signal. This effect is found to be related to the formation of hybrid states at the NaDyClq/NiFe (Co) interface. Element-specific, *in-situ* X-ray absorption spectra reveal the existence of interface-specific hybridized Co-N and Py-C states, both of which are found to be energetically below the LUMO of the molecule and hence contributing to the electronic and spin-dependent transport of the spin valves. This combined transport and spectroscopic study of the spin valve structures demonstrate how a specific interaction between a ferromagnetic metal and a molecule governs macroscopic device parameters such as the sign and magnitude of magnetoresistance. These findings underline the huge potential of molecules to tailor spin-dependent properties at metal interfaces and most importantly, transduce this microscopic interaction into device output signals, ultimately proving the *spinterface* concept [2] in functional large-area spintronic devices.

ACKNOWLEDGEMENTS

A.B.-P. and S.G.M. contributed equally to this work. The authors thank Roger Llopis for technical support at CiC nanoGUNE. Financial support from the EU (COST Action in Molecular Spintronics 15128, Projects HINTS FP7-263104, Spintros ERC Starting Grant ERC-2009-257654, and SpinMol ERC Advanced Grant ERC-2009-AdG-20090325), the Spanish Ministry of Economy and Competitiveness (MINECO) (Unit of Excellence Maria de Maeztu MDM-2015-0538 and MDM-2016-0618 as well as projects co-funded by the ERDF MAT2011-22785 MAT2012-37638, FIS2013-45469-C4-3-R, MAT2014-56143-R, and MAT2015-65159-R), Generalitat Valenciana (PROMETEO programme). S.G.M. thanks the Spanish MINECO for an FPI predoctoral grant. The authors acknowledge beamtime access at ALBA BL29 via proposal 2015-021263.cofinancing MAT2011-22785 MAT2012-37638, FIS2013-45469-C4-3-R, MAT2014-56143-R, and MAT2015-65159-R), Generalitat Valenciana (PROMETEO programme). S.G.M. thanks the Spanish MINECO for an FPI predoctoral grant. The authors acknowledge beamtime access at ALBA BL29 via proposal 2015-021263.

OTHER REFERENCES

1.V. A. Dediu, L. E. Hueso, I. Bergenti, C. Taliani, *Nat. Mater.* **2009**, *8*, 707.

2. M Cinchetti, VA Dediu, L.E Hueso, *Nat. Mater.* ***2017,*** 16 (5), 507.

3. A. Lodi Rizzini, C. Krull, T. Balashov, J. J. Kavich, A. Mugarza, P. S. Miedema, P. K. Thakur, V. Sessi, S. Klyatskaya, M. Ruben, S. Stepanow, P. Gambardella, *Phys. Rev. Lett.* **2011**, *107*, 1.

4. A. Demasi, L. F. J. Piper, Y. Zhang, I. Reid, S. Wang, K. E. Smith, J. E. Downes, N. Peltekis, C. McGuinness, A. Matsuura, *J. Chem. Phys.* **2008**, *129*.

AFFILIATION:

1. CIC nanoGUNE Tolosa Hiribidea 76, 20018 Donostia - San Sebastián, Spain.
2. Institute of Molecular Science (ICMol), University of Valencia, C/ Catedrático José Beltrán 2, E-46980, Valencia, Spain.
3. ALBA Synchrotron, E-08290 Cerdanyola del Vallés, Barcelona, Spain.
4. IKERBASQUE, Basque Foundation for Science, 48011 Bilbao, Spain.

Electronically cubic J_{eff} = 1/2 ground state for α-$RuCl_3$, a candidate material for the observation of Majorana fermions

Electronically highly cubic conditions for Ru in α-$RuCl_3$. *Physical Review B* 96, 161107(R) (2017)

S. Agrestini[1], C.-Y. Kuo[1], K.-T. Ko[1], Z. Hu[1], D. Kasinathan[1], H. B. Vasili[2], J. Herrero-Martin[2], S. M. Valvidares[2], E. Pellegrin[2], L.-Y. Jang[3], A. Henschel[1], M. Schmidt[1], A. Tanaka[4], and L. H. Tjeng[1]

Using ALBA and Taiwan synchrotron sources, a group of international researchers have determined the local symmetry of the electronic and magnetic ground state of α-$RuCl_3$.

α-$RuCl_3$ is the most promising candidate for the long-sought materialization of the Kitaev model and for the observation of emergent Majorana fermion excitations. These fermions, predicted to exist by E. Majorana in 1937, are identical to their own antiparticles but, despite being looked for 80 years, firm evidence of them is still missing. A prerequisite for these expectations is that the symmetry-imposed noncubic crystal field is smaller compared to the spin-orbit coupling and does not significantly perturb the description of the electronic ground state in terms of the J_{eff} = 1/2 state.

An international research team has used ALBA and Taiwan synchrotron sources to investigate the ground state of α-$RuCl_3$. The authors have combined polarization-dependent X-ray absorption spectroscopy, a technique that gives direct access to the crystal field of a material, and full multiplet atomic calculations to determine the size and sign of the noncubic crystal-field splitting. The results demonstrate that the "electronically cubic conditions" and the J_{eff} = 1/2 ground state for Ru in α-$RuCl_3$ are fulfilled.

Single crystals of α-$RuCl_3$ were grown by chemical transport reaction with chlorine between 730 to 660 °C and annealed for five months at 440 °C under vacuum.

X-ray Linear Dichroism (XLD) and X-Ray Magnetic Circular Dichroism (XMCD) are well-established techniques to study the local electronic and magnetic properties, respectively. The XMCD signal can be analyzed by means of sum rules, allowing for a direct experimental determination of the desired quantum numbers L_z and S_z. The energy separation between Ru-L_3 and L_2 edges of about 150 eV is much larger than the multiplet effects (a few eV), and therefore the spectra are very suitable also for spin sum rule analysis. It is important to stress that obtaining a reasonable degree of circular polarized light at the photon energies of the *L* edges of 4*d* elements is challenging. BOREAS beamline at ALBA was key to experimentally confirm the J_{eff} = 1/2 state ground state by allowing to perform XMCD measurements at the Ru $L_{3,2}$ edges thanks to its broad photon energy range extending onto the tender x-ray range (2-4 keV). The XMCD signal was measured using a magnetic field of 6 Tesla with the sample at a temperature of 2 K. The spectra were recorded using the total electron yield method (by measuring the sample drain current) in a chamber with a vacuum base pressure of $2x10^{-10}$ mbar.

The linear polarized XAS or XLD was measured at the 16A1 tender x-ray beamline of the NSRRC in Taiwan.

The linear dichroism at the Ru $L_{2,3}$ edges (see Fig. 33) was found to be vanishingly small, which indicates that electronically the Ru 4*d* local symmetry is highly cubic. Using full atomic multiplet cluster calculations the authors were able to reproduce the spectra excellently and to extract that the non-cubic crystal field is −12 ± 10 meV, i.e., negligible as compared to the Ru 4*d* spin-orbit coupling (150 meV). Consistent with the XMCD measurements performed in ALBA and reported in Fig. 34, a ratio was determined of 2.0

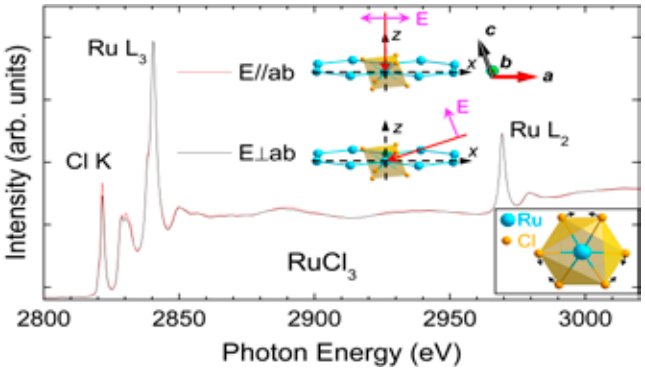

Figure 33: Experimental Ru $L_{2,3}$ X-Ray Absorption (XAS, blue circles) and X-Ray Magnetic Circular Dichroism (XMCD, green circles) spectra of a $RuCl_3$ single crystal together with calculated XAS (blue line) and XMCD (green line). The spectra were measured at $T = 2$ K and $B = 6$ T.

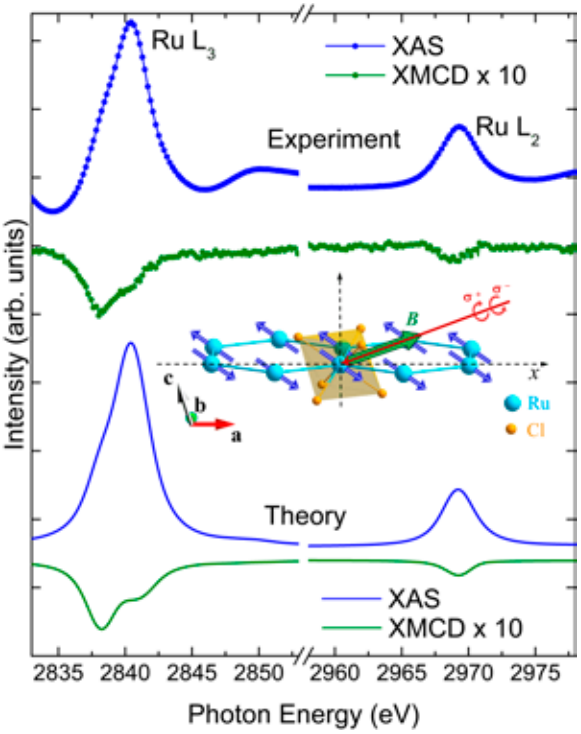

Figure 34: Ru $L_{2,3}$ X-Ray absorption spectra of a $RuCl_3$ single crystal for incoming linear polarized light with the electric field vector **E** normal (black line) and parallel (red line) to the *ab* plane. Inset: Sketch of the trigonal distortion of the $RuCl_6$ octahedron.

between the orbital and the spin contributions to the local Ru 4*d* magnetic moment, i.e., the value expected for a $J_{eff} = 1/2$ ground state. The results therefore demonstrate that, as far as the Ru 4*d* local properties are concerned, α-$RuCl_3$ is an ideal candidate for the realization of Kitaev physics and for the observation of emergent Majorana fermion excitations.

ACKNOWLEDGEMENTS

The research in Dresden was partially supported by the Deutsche Forschungsgemeinschaft through SFB 1143 and FOR1346. K.-T.K. acknowledges support from the Max Planck-POSTECH Center for Complex Phase Materials (Grant No. KR2011-0031558).

AFFILIATION:

1. Max Planck Institute for Chemical Physics of Solids, Nöthnitzerstrasse 40, 01187 Dresden, Germany.
2. ALBA Synchrotron, 08290 Cerdanyola del Vallès, Barcelona, Spain.
3. National Synchrotron Radiation Research Center, 101 Hsin-Ann Road, Hsinchu 30076, Taiwan.
4. Department of Quantum Matter, ADSM, Hiroshima University, Higashi-Hiroshima 739-8530, Japan.

Magnetic coupling through graphene: a single-atom-thick spacer layer for synthetic anti-ferromagnets

Graphene-based synthetic antiferromagnets and ferrimagnets.
***Nature Communications* 8, 699 (2017)**

P. Gargiani[1], R. Cuadrado[2,3], H. B. Vasili[1], M. Pruneda[2,3] and M. Valvidares[1]*

Researchers have developed novel graphene-based antiferromagnetic multilayer structures featuring robust magnetic properties. Employing X-ray magnetic circular dichroism and theoretical DFT calculations, the authors have demonstrated that single-layer graphene-spaced magnetic thin film structures present perpendicular antiferromagnetic coupling together with a number of properties that are well suited for applications.

Antiferromagnetic spintronics may pave the way to innovative information storage devices promising lower energy current induced switching and higher information densities. In this context, synthetic ferrimagnetic and antiferromagnetic (SFiM,SAF) structures are gaining renewed attention for spintronic applications and magnetic information storage. SAF structures based on metallic multilayers were initially developed in the 90s, inspired by the discovery of exchange coupling in multilayers and oscillatory magnetic interactions. A prototypical SAF structure is composed of two ferromagnetic films that are antiferromagnetically exchange-coupled through a non-magnetic spacing material due to the Ruderman–Kittel–Kasuya–Yosida (RKKY) interaction, and have been broadly used to improve the thermal and magnetic properties of spin valves. Furthermore, exchange-coupled magnetic layers with perpendicular magnetic anisotropy (PMA) are intensively studied for developing vertical magnetic tunnel junctions (MTJs), in views of their potential application in future high-density and low current-induced magnetization-switching spintronic devices. In the search for novel hybrid SAF structures, graphene-spaced magnetic systems with perpendicular coupling may offer exciting opportunities for emerging technologies.

To this end, a team of researchers employed element-resolved X-ray Magnetic Circular Dichroism (XMCD) and *ab-initio* density functional theory (DFT) calculations to demonstrate that ultra-thin Fe/graphene/Co films grown on Ir(111) (Fig. 34a) exhibit robust perpendicular antiferromagnetic exchange-coupling, and gather a collection of magnetic properties well-suited for applications. The samples, grown *in-situ* in the experimental facilities available at the BOREAS beamline, were realized by employing the intercalation method that allows to grow a magnetic layer directly below a single-layer graphene sheet, ensuring the realization of a particularly clean and controllable interface. The XMCD technique, being element sensitive, allows disentangling the magnetic behavior of the different elements of the multilayer structures. In this way it is possible to unravel the relative orientation of the magnetization of the Fe and Co layers in the Fe/graphene/Co hetero-structures. It was found that the single-atomic thin Graphene film mediates a strong antiferromagnetic exchange interaction between the

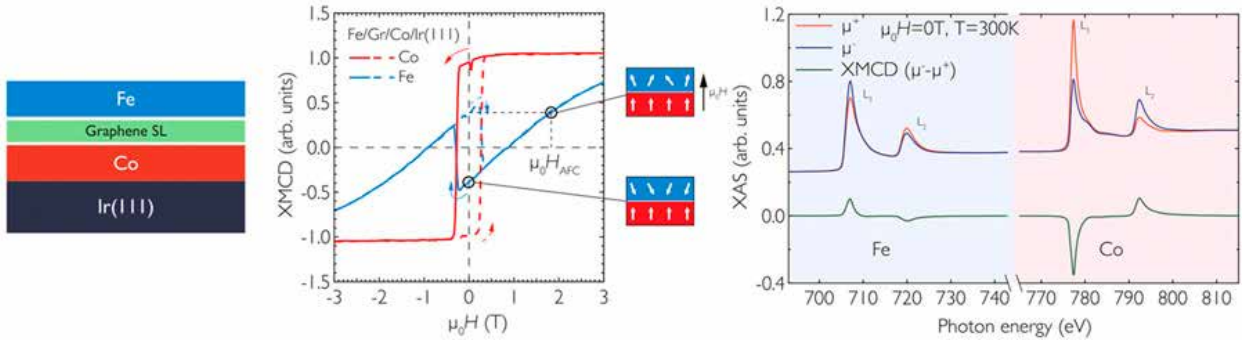

Figure 35: On the left, a schematic view of the Fe/Gr/Co/Ir(111) multilayer system. At the center, an element specific XMCD magnetization loop showing the magnetization of the Co and Fe layers with antiparallel orientation when there is no applied magnetic field. On the right, a view of the XMCD spectra collected at BOREAS showing the sign inversion of the Fe and Co magnetic signal proof of the antiferromagnetic ordering of the films.

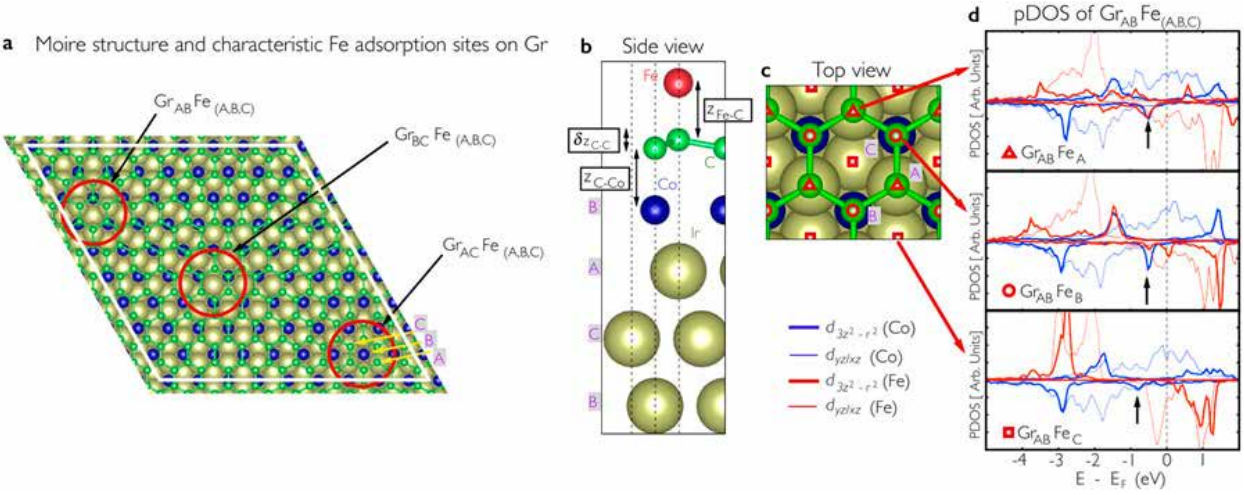

Figure 36: Left, structural models for Fe/Gr/Co/Ir(111) heterostructures as a result of the first principles calculations. (a) Schematic top view of the Moiré superlattice defined by graphene on top of Co/Ir(111). Center: side view of the system in one configuration. Right: projected density of states (pDOS) on Co and Fe d states indicating the presence of a peak in the DOS in the stronger antiferromagnetic coupling arrangements.

Fe and Co films, as evidenced by the sign inversion of the XMCD signal between Fe and Co (Fig 35c). The XMCD signal measured as a function of the applied magnetic field (Fig. 35b), demonstrates that the remnant state of the magnetic multilayer has an antiparallel orientation of the Fe and Co magnetization with a perpendicular orientation with respect to the sample surface. A temperature dependence investigation of the XMCD signal demonstrates that the exchange coupling is stable at and above room temperature. Those remarkable findings are both of fundamental importance when it comes to possible applications.

The atomistic first-principle DFT calculations (Fig. 36) confirmed that Graphene does not act as a mere spacer but has a direct role in sustaining the AF coupling. In particular, the Fe and Co layers magnetically interact via the hybridization of their wave functions with graphene's, thus enabling a *super-exchange interaction mechanism* mediated by the single atomic thin graphene film, in contrast with metallic multilayer SAF structures where the RKKY type exchange interaction is mediated by several atomic layers of non-magnetic metal.

These results provide a path for producing graphene-based perpendicular synthetic antiferromagnetic systems, which seem exciting for fundamental nanoscience but also for their potential use in spintronic devices. They demonstrate an additional class of synthetic-AF multilayered materials that, while being of fundamental interest, appear capable of providing practical magnetic devices with PMA which are potentially relevant for perpendicular magnetic recording media, perpendicular spin valves, MTJ structures or all-optical switching magnetic materials.

ACKNOWLEDGEMENTS

The research leading to this work has been funded by Spanish MINECO/FEDER, grants no. FIS2013-45469-C4-3-R (AEI / ERFD, EU). Additional funding by FIS2015-64886-C5-3-P, FIS2016-78591-C3-2-R (AEI/ERDF, EU), and MAT2014-59315-R, Government of Catalonia (2014SGR301), CERCA Programme/Government of Catalonia, European Union H2020-EINFRA-2015-1 grant agreement No. 676598 and ALBA in-house research program is acknowledged.

OTHER REFERENCES

1. Jungwirth, T., Marti, X., Wadley, P. & Wunderlich, J. Antiferromagnetic spintronics. *Nat. Nanotechnol.* **11**, 231–241 (2016).

2. Grünberg, P., Schreiber, R., Pang, Y., Brodsky, M. B. & Sowers, H. Layered magnetic structures: evidence for antiferromagnetic coupling of Fe layers across Cr interlayers. *Phys. Rev. Lett.* **57**, 2442–2445 (1986); Parkin, S. S. P., More, N. & Roche, K. P. Oscillations in exchange coupling and magnetoresistance in metallic superlattice structures: Co/Ru, Co/Cr, and Fe/Cr. *Phys. Rev. Lett.* **64**, 2304–2307 (1990).

3. Rougemaille, N. et al. Perpendicular magnetic anisotropy of cobalt films intercalated under graphene. Appl. Phys. Lett. 101, 142403 (2012).

AFFILIATION:

1. ALBA Synchrotron, Cerdanyola del Valles, Bellaterra, 08290, Barcelona, Spain.
2. Catalan Institute of Nanoscience and Nanotechnology (ICN2), CSIC Campus UAB, Bellaterra, 08193, Barcelona, Spain.
3. Universitat Autonoma de Barcelona, Cerdanyola del Valles, Bellaterra, 08193, Barcelona, Spain.

Observation of correlated displacement of vortex-antivortex pairs in magnetic trilayers

Deterministic propagation of vortex-antivortex pairs in magnetic trilayers *Appl. Phys. Lett.* 110, 262402 (2017)

A. Hierro-Rodriguez[1], C. Quirós[2,3], A. Sorrentino[4], R. Valcárcel[4], I. Estébanez[2], L. M. Alvarez-Prado[2,3], J. I. Martín[2,3], J. M. Alameda[2,3], E. Pereiro[4], M. Vélez[2,3] and S. Ferrer[4]

Using X–ray microscopy, authors have found an interesting result concerning the correlated motion of V-AV pairs along stripe magnetic domains in magnetic structures.

Spintronics exploits the spin of the electrons which confers their magnetic moment to store information or to process it. Moving magnetic walls separating two parts of a magnetic system with different magnetizations carries magnetic information sensed by reading heads; however domain walls are sensitive to imperfections in the materials that disrupt their displacements. Magnetic singularities such as vortices, skyrmions or other, are textures of the magnetization with topological characteristics that provide robustness against external perturbations. A magnetic vortex (V) is one of the most studied singularities. It can be visualized as a typhoon in the atmosphere that can move long distances without being perturbed by buildings or trees. In magnetism, instead of the air, it is the magnetization that is rotating. An antivortex (AV) is another singularity that, if it collides with a vortex, results in mutual annihilation.

The microscope at MISTRAL, which is usually devoted to tomographic imaging of biological cells, can also be used for magnetic studies by utilizing the circularly polarized synchrotron radiation laying above or below the horizontal plane of the electrons orbit in the storage ring. The XMCD effect provides element specific magnetic sensitivity and allows acquiring images of the magnetization of a sample with magnetic domains. As the dichroic contrast is proportional to cosθ, where θ is the angle that the X ray beam makes with the magnetization, the technique also provides information on the components of the magnetization.

The samples investigated were magnetic trilayers consisting in a central film of NdCo with weak perpendicular magnetic anisotropy and magnetically softer permalloy (Py) at the top and GdCo layer at the bottom. Their individual thickness was in the range 40-60 nm. They were grown at the Condensed Matter Physics Laboratory of the University of Oviedo by DC sputtering at room temperature. The application of an in-plane magnetic field to the sample results in stripe domains in the central layer that are imprinted by exchange coupling to the external ones.

The images in the figure were acquired at an angle of 35 deg, with respect to the normal of the film and are sensitive to the x (in-plane) and z (perpendicular) components of the magnetization. The photon energy was tuned to the L3 Fe absorption energy and the images are therefore sensitive to the magnetization of the permalloy layer only. The blue arrows (+,+) and (+,-) indicate the signs of (mx, mz). Enclosed in the dashed circle is a bifurcation. The image was acquired after applying an in-plane magnetic field pulse

of -15 mT aimed to invert mx. Whereas at the top image mx is positive everywhere, after increasing the field amplitude to -17 mT (central image) two new contrasts appear corresponding to the inversion of mx as indicated by the red arrows. Further increase in the field leads to the propagation to the left of the (-,-) and (-,+) stripe terminations. Detailed micromagnetic simulations demonstrated that at the end points of the (-,-) and (-,+) stripes, vortex and antivortex singularities exist. Simulated images agreed very well with the measurements. Comparing the images at -17 and -19 mT , we observe that the V-AV move together about 3 μm. Interestingly, the motion can be inverted and then repeated again in a controlled way provided that the magnitude of the field is not too large. The magnetic stripes act as roads to transport the V-AV pairs along distances which are large at nm scale. An interesting feature is that these magnetic stripes are formed spontaneously by applying a magnetic field and do not require any nanometric engineering. The V-AV pairs are robust and might have applications in transport of magnetic information. Moreover, it was also observed that V-AV pairs emanating from bifurcations pointing to the opposite sense than that in the figure and having inverted sign of mz, moved in opposite sense to that in the figure, i.e. to the right when the negative Hx field was increased. The reason for this difference is well understood from micromagnetic simulations and previous work.

In summary, magnetic bifurcations act as nuclei for the inversion of the magnetization in permalloy/NdCo/GdCo trilayers with stripe domains. At the permalloy layer the inversion occurs by the generation of vortex antivortex pairs that can move together several micrometers along the magnetic stripes. This is a robust result that might have practical applications in spintronic devices.

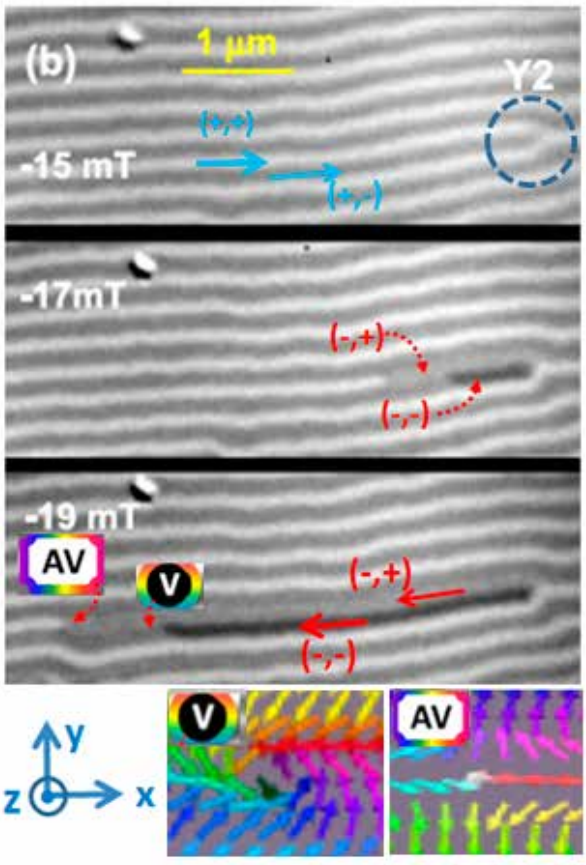

Figure 37: Magnetic images of the propagation of reversed domains in the NiFe layer under a sequence of Hx pulses, as indicated in each panel. The signs of (Mx, Mz) magnetizations at different locations are indicated. The upper branch of the bifurcation changes the sign of Mx, as indicated, and has an antivortex (AV) that propagates along the white stripe. The lower branch also inverts the sign of Mx and has a vortex V that propagates towards the left. The correlated motion of the V-AV pair is controllable with the applied field extending several micrometers.

AFFILIATION:
1. IN-IFIMUP, Department of Physics and Astronomy, Faculty of Sciences, University of Porto, 4169-007 Porto, Portugal.
2. Physics Department, University of Oviedo, 33007 Oviedo, Spain.
3. Research Centre for Nanomaterials and Nanotechnology, CINN (CSIC – Universidad de Oviedo), 33940 El Entrego, Spain.
4. ALBA Synchrotron, 08290 Cerdanyola del Vallès, Spain.

Imaging dynamic magnetoelectric and magnetothermal memory effects in FeRh

Electric-Field-Adjustable time-dependent magnetoelectric response in martensitic FeRh alloy. ***ACS applied materials & interfaces*** **9** (18), 15577-15582 (2017)

I. Fina[1], A. Quintana[2], J. Padilla-Pantoja[3], X. Martí[4], F. Macià[1], F. Sánchez[1], M. Foerster[6], L. Aballe[6], J. Fontcuberta[1], and J. Sort[2]

Hidden Magnetic States Emergent Under Electric Field, In A Room Temperature Composite Magnetoelectric Multiferroic. ***Scientific Reports*** **7** (1), 15460 (2017)

J. D. Clarkson[1], I. Fina[2], Z. Q. Liu[1,3], Y. Lee[1], J. Kim[4], C. Frontera[2], K. Cordero[5], S. Wisotzki[6], F. Sanchez[2], J. Sort[7,8], S. L. Hsu[1,9], C. Ko[1], L. Aballe[10], M. Foerster[10], J. Wu[1,9], H. M. Christen[3], J. T. Heron[11,12], D. G. Schlom[11], S. Salahuddin[13], N. Kioussis[4], J. Fontcuberta[2], X. Marti[14],R. Ramesh[1,9,14]

Time dependent magnetoelectric response and thermal/electric-field driven magnetic memory effects in near room temperature FeRh metamagnetic phase transition revealed by XMCD-PEEM microscopy.

Magnetic materials have been used to store all sort of information, mainly information requiring long-term storage. The appearance of magnetic memories stimulated the concomitant optimization of replication processes to assist the ultimate purpose of information dissemination. This duplication is in general assumed legitimate. However, there is a worrying increase of illicit copies. Industry demands for a higher degree of security point out to a strategy of producing storage media able to protect the stored data by themselves. Overall, hiding the stored information at the materials level will fulfill the demands of the industry.

Authors have investigated how magnetic domain can disappear and appear again at the same position while crossing the metamagnetic phase transition in FeRh films, controlled either by thermal or electric stimuli. FeRh shows an antiferromagnetic to ferromagnetic phase transition while increasing temperature. X-ray Magnetic Circular Dichroism in combination with PhotoEmission Electron Microscopy (XMCD-PEEM) technique can allow to track this phase transition in FeRh films as revealed by Figure 38 that shows XMCD and PEEM images. In the figure, green regions account for no-magnetic contrast and blue (valleys) and red (mountains) account for ferromagnetic domains pointing along opposite directions. In Figure 38a, XMCD-PEEM image collected at room temperature shows no significant contrast. As temperature increases (Figures 38b,c collected at ≈110 ºC and ≈170 ºC, respectively) ferromagnetism emerges and the exact position of newly formed domains can be tracked. After thermal and electric cycling (the latter produced thanks to the necessary use of a piezoelectric film stacked to the FeRh film), authors reported that magnetic domains appear at the same position. The effect is robust and reconweurable. Thus, it demonstrates that the materials show the ability of storing magnetic information and hide it across the metamagnetic phase transition. XMCD-PEEM also allowed tracking the magnetic state under the application of external electric field with approx. 2 seconds time resolution. The information collected

using this technique revealed an unexpected dynamic magnetoelectric response plus the fact that contraction and expansion of ferromagnetic domains in the antiferromagnetic matrix rather than ferromagnetic domain nucleation (similar to what happens under thermal cycling) accounts for the observed memory effects.

To sum up, thermally or electrically crossed FeRh phase transition has been characterized at the microscopic level allowing to conclude that very small ferromagnetic domains surviving at very low temperatures are responsible for the observed magnetic memory effects. Time dependent FeRh phase transition controlled by electric means has also been characterized as showing an unexpected dynamic magnetoelectric response.

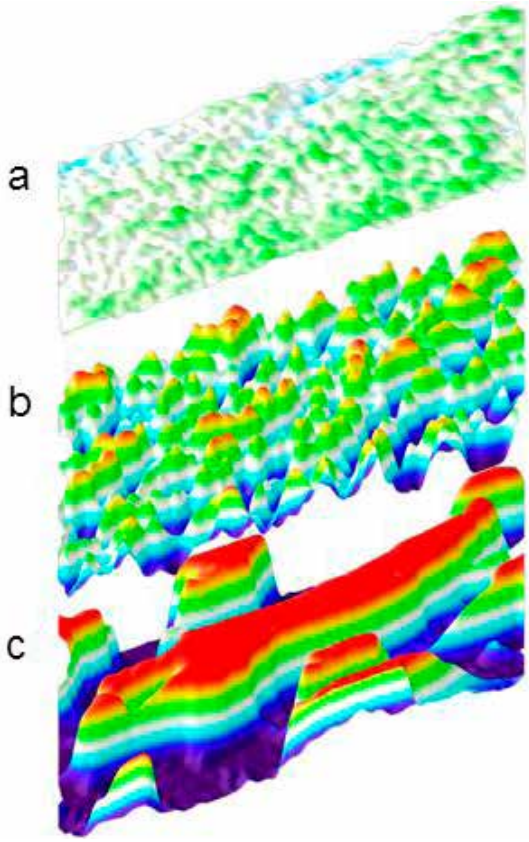

Figure 38: XMCD-PEEM image sequence of magnetic domains in a FeRh film at (a) RT, (b) ≈110 ºC, and (c) 170 ºC.

AFFILIATION:

1. Institute of Materials Science of Barcelona (ICMAB-CSIC), Campus UAB, Bellaterra, E-08193 Barcelona, Spain.
2. Department of Physics, Universitat Autònoma de Barcelona, Bellaterra, E-08193 Barcelona, Spain.
3. Catalan Institute of Nanoscience and Nanotechnology (ICN2), CSIC and The Barcelona Institute of Science and Technology, Campus UAB, Bellaterra, E-08193 Barcelona, Spain.
4. Institute of Physics, Academy of Sciences of the Czech Republic, Cukrovarnická 10, 162 53 Praha 6, Czech Republic.
5. ALBA Synchrotron, Carrer de la Llum 2-26, Cerdanyola del Vallès, 08290 Barcelona, Spain.
6. Catalan Institution for Advanced Research and Studies (ICREA), Pg. Lluís Companys 23, E-08010 Barcelona, Spain.

---

1. Department of Materials Science and Engineering, University of California, Berkeley, California, 94720, USA.
2. Institute of Materials Science of Barcelona (ICMAB-CSIC), Campus UAB, Bellaterra, 08193, Barcelona, Spain.
3. Oak Ridge National Laboratory, Center for Nanophase Materials Sciences, Oak Ridge, Tennessee, 37831, USA.
4. Department of Physics, California State University, Northridge, California, 91330-8268, USA.
5. Catalan Institute of Nanoscience and Nanotechnology (ICN2), CSIC and The Barcelona Institute of Science and Technology, Campus UAB, Bellaterra, 08193, Barcelona, Spain.
6. Max Planck Institute of Microstructure Physics, Weinberg 2, D-06120, Halle (Saale), Germany.
7. Department of Physics, Universitat Autònoma de Barcelona, E-08193, Bellaterra, Spain.
8. Catalan Institution for Advanced Research and Studies (ICREA), Passeig Lluís Companys 23, E-08010, Barcelona, Spain.
9. Materials Sciences Division, Lawrence Berkeley National Laboratory, Berkeley, California, 94720, USA.
10. ALBA Synchrotron, Carrer de la Llum 2-26, Cerdanyola del Vallès, Barcelona, 08290, Spain.
11. Department of Materials Science and Engineering, Cornell University, Ithaca, New York, 14850, USA.
12. Department of Materials Science and Engineering, University of Michigan, Ann Arbor, Michigan, 48109, USA.
13. Department of Electrical Engineering and Computer Science, University of California, Berkeley, California, 94720, USA.
14. Department of Physics, University of California, Berkeley, California, 94720, USA.
15. Institute of Physics ASCR, v.v.i., Cukrovarnicka 10, 162 53, Praha 6, Czech Republic.

Magnetism catches the wave – Picosecond magnetization dynamics induced by magnetoelasticity

Direct imaging of delayed magneto-dynamic modes induced by surface acoustic waves. *Nature Communications* 8, 407 (2017)

M. Foerster[1*], F. Macia[2,3], J. M. Hernandez[3], S. Finizio[4,5], A. Hernandez-Minguez[6], N. Statuto[2,3], S. Lendinez[3], P. Santos[6], J. Fontcuberta[3], M. Klaeui[4], and L. Aballe[1]

The magneto-elastic effect, i.e. the change of magnetic properties under elastic deformation (strain) has been studied with unprecedented spatial and temporal resolution in the photoemission electron microscope.

The control of nanometric magnetic domains by electrical voltages rather than conventional electrical currents (entailing Ohmic losses) has been a focus of material science research, driven by the promise of more energy efficient microelectronic devices and memories. Within multiferroic materials and heterostructures, the most sizable magnetoelectric effects have been realized using strain mediated coupling, i.e. the magnetoelastic effect. However, while most studies have focused on the static or very slow timescales, which are incompatible with the envisaged applications, experiments at the CIRCE beamline demonstrated the dynamic magnetic response to an elastic deformation on the picosecond timescale with a spatial resolution below 100 nm. The photoemission electron microscope (PEEM) used for these studies forms images of the sample using the electrons emitted under illumination by the ALBA Synchrotron light. The experiment makes use of the synchrotron light time structure (a short pulse of light every 2 ns), exciting the sample at the same frequency.

The key ingredient of the experiment is the generation of dynamic strain (deformation) of the magnetic system (Ni squares in a Landau flux closure state) by surface acoustic waves (SAW) in an underlying piezoelectric $LiNbO_3$ (LNO) substrate (Figure 39). The SAW excitation signal applied to the "antennas" (interdigitated electrodes, IDT) is perfectly synchronized with the Synchrotron light pulses through the master radio frequency close to 500 MHz using a system developed by the ALBA Electronics department. The synchronization allows acquiring stroboscopic images (snapshots) of the sample with a propagating SAW, where each single Ni square is in a well-defined strain state. Note how in part of Figure 39 labelled "PEEM image" the SAW is directly visible as bright and dark gray, vertical stripes. The SAW is visible because it shifts the piezoelectric LNO surface potential varying with the phase. Importantly, this fact provides the data to quantify in which strain state each Ni square is. Magnetic contrast is obtained by combining images with opposite circular polarization through X-ray circular magnetic dichroism (XMCD) at the Ni L_3 absorption edge.

The SAW induces a time dependent magnetic anisotropy in the Ni square through the magnetoelastic effect along the SAW propagation direction [1]. An example of the resulting effect is shown in Figure 40. On the left, two schematics of domain configurations

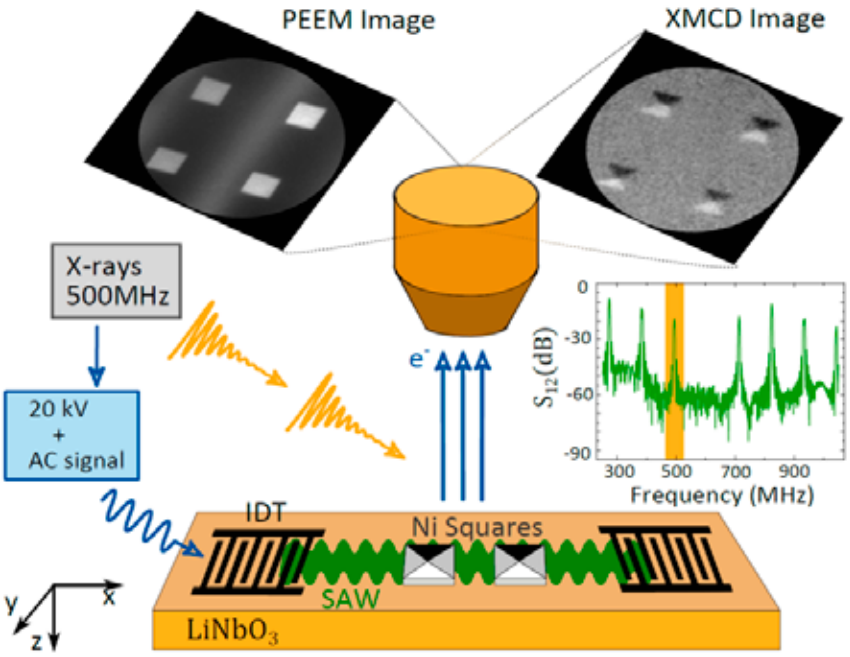

Figure 39: Scheme of the experiment: Propagating surface acoustic waves (SAW) are excited in a $LiNbO_3$ crystal onto which magnetic Nickel patterns have been prepared. The SAW are synchronized with the Synchrotron light pulses in order to obtain stroboscopic images with a fixed SAW phase for each point on the sample, and magnetic images using the XMCD effect.

(four domains in flux closure state) with zero (upper) and finite (lower) uniaxial anisotropy favoring the horizontal magnetization direction are shown, colored in the corresponding grayscale of an XMCD-PEEM image. On the right, a series of direct (upper) and XMCD (lower) images at different electronic delays and thus phase of the SAW in the Ni square (2x2 um) are shown. One can clearly appreciate how the SAW passes with a maximum (bright gray stripe) through the Ni square between the third and fourth panel, while the magnetic domain configuration reaches an extreme point, marked by the maximum extension of black and white domains, later, i.e. between the fourth and fifth panel. The delay for this magnetic response, taking place through domain wall motion, is determined to be around 270 ps from a fit to all data. On the other hand, if the geometry is adapted so that the SAW is passing a Ni square along its diagonal, no domain wall motion occurs, but the magnetization rotates within each domain, which is a much faster process with a smaller delay of around 90 ps. These results are understood in a quantitative micromagnetic model (Fig. 41).

In summary, the experiment resolves the magnetoelastic effect in Ni patterns triggered by surface acoustic waves with unprecedented spatial and temporal resolution. First, it demonstrates that sizable magneto-elastic effects can be achieved on this fast timescale. Moreover, it reveals that the response time, with delays in the order of hundreds of ps, which will ultimately determine the operation

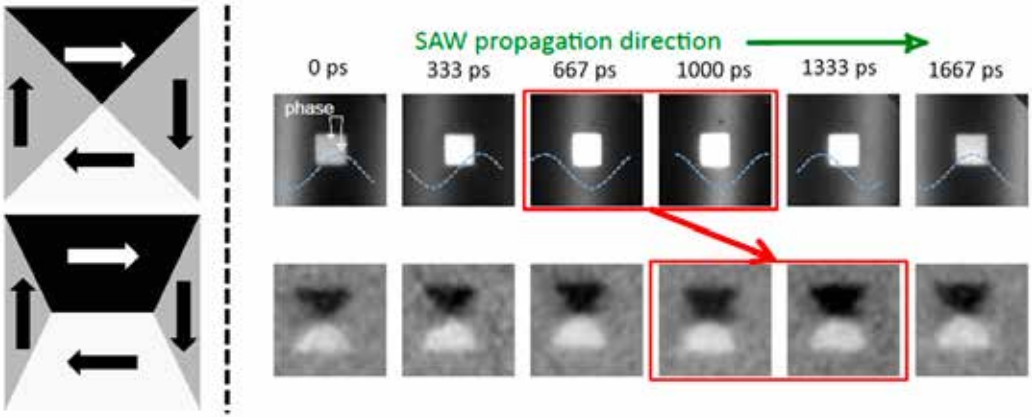

Figure 40: Left: Schematic of the response of an ideal magnetic square in flux closure state to an induced anisotropy favoring domains with horizontal magnetization. In the lower figure, black and white domains are enlarged at the cost of the gray domains. The gray scale colors correspond to the domain appearance in XMCD-PEEM. Right, upper line: Direct PEEM images from which the phase of the SAW (bright gray vertical stripe) at the Ni square (2x2 um) is determined. Lower line: corresponding XMCD magnetic contrast images showing the variations between the domains.

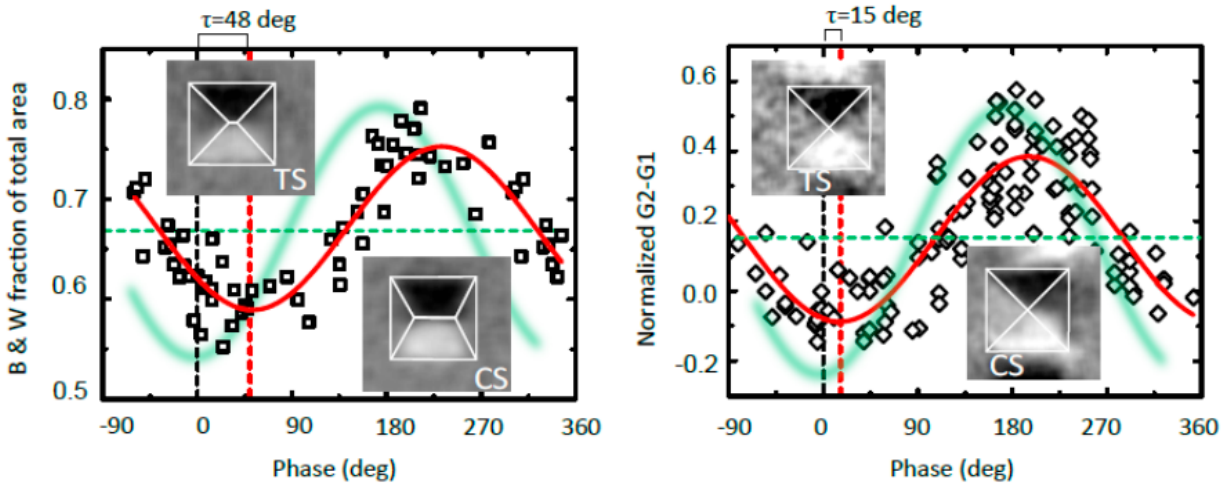

Figure 41: Fits to experimental data of the two configurations and the resulting delays.

rate, is given by the intrinsic magnetization dynamics itself and not limited by the magneto-elastic effect or the transmission of strain. Thus, the importance of the right choice of the magnetic system and domain configuration is highlighted.

OTHER REFERENCES

1. S. Davis, A. Baruth and S. Adenwalla, Appl. Phys. Lett. **97**, 232507 (2010)

ACKNOWLEDGEMENTS

The authors thank Jordi Prat for technical help on the beamline and with the data analysis, Hermann Stoll and Rolf Hedemann for advice on electronics, Abel Fontsere, Bernat Molas and Oscar Matilla from ALBA electronics for the development of the 500 MHz synchronous excitation setup, and Werner Seidel from PDI for assistance in the preparation of the acoustic delay lines on LiNbO3.

The project was supported by the ALBA in-house research program through IH2015PEEM and the allocation of in-house beamtime as well as with proposal 2016021647. FM acknowledges financial support from the Ramon y Cajal program through RYC-2014-16515. FM and JF acknowledge support from MINECO through the Severo Ochoa Program for Centers of Excellence in R&D (SEV-2015-0496). Funding from MINECO through MAT2015-69144 (JMH, NS and FM) and MAT2015-64110 (LA and MF) is acknowledged. SF and MK acknowledge the Graduate School of Excellence Materials Science in Mainz (Grant No. GSC 266), the Swiss National Science Foundation (SNF), the German Research Foundation DFG (TRR 173 Spin+X), the ERC (ERC-2014-PoC 665672 MULTIREV), The EC (NMP3-LA-2010 246102 IFOX, FP-PEOPLE-2013-ITN 608003 WALL) and the Center for Innovative and Emerging Materials at the Johannes Gutenberg Universitaet Mainz.

AFFILIATION:

1. ALBA Synchrotron, 08290, Cerdanyola del Valles, Spain.
2. Institute of Materials Science of Barcelona (ICMAB-CSIC), Campus UAB, 08193, Bellaterra, Spain.
3. Dept. of Condensed Matter Physics, University of Barcelona, 08028, Barcelona, Spain.
4. Institut für Physik, Johannes Gutenberg Universität Mainz, 55099, Mainz, Germany.
5. Swiss Light Source, Paul Scherrer Institut, CH-5232, Villigen PSI, Switzerland.
6. Paul-Drude-Institut fur Festkörperelektronik, Hausvogteiplatz 5-7, 10117, Berlin, Germany.

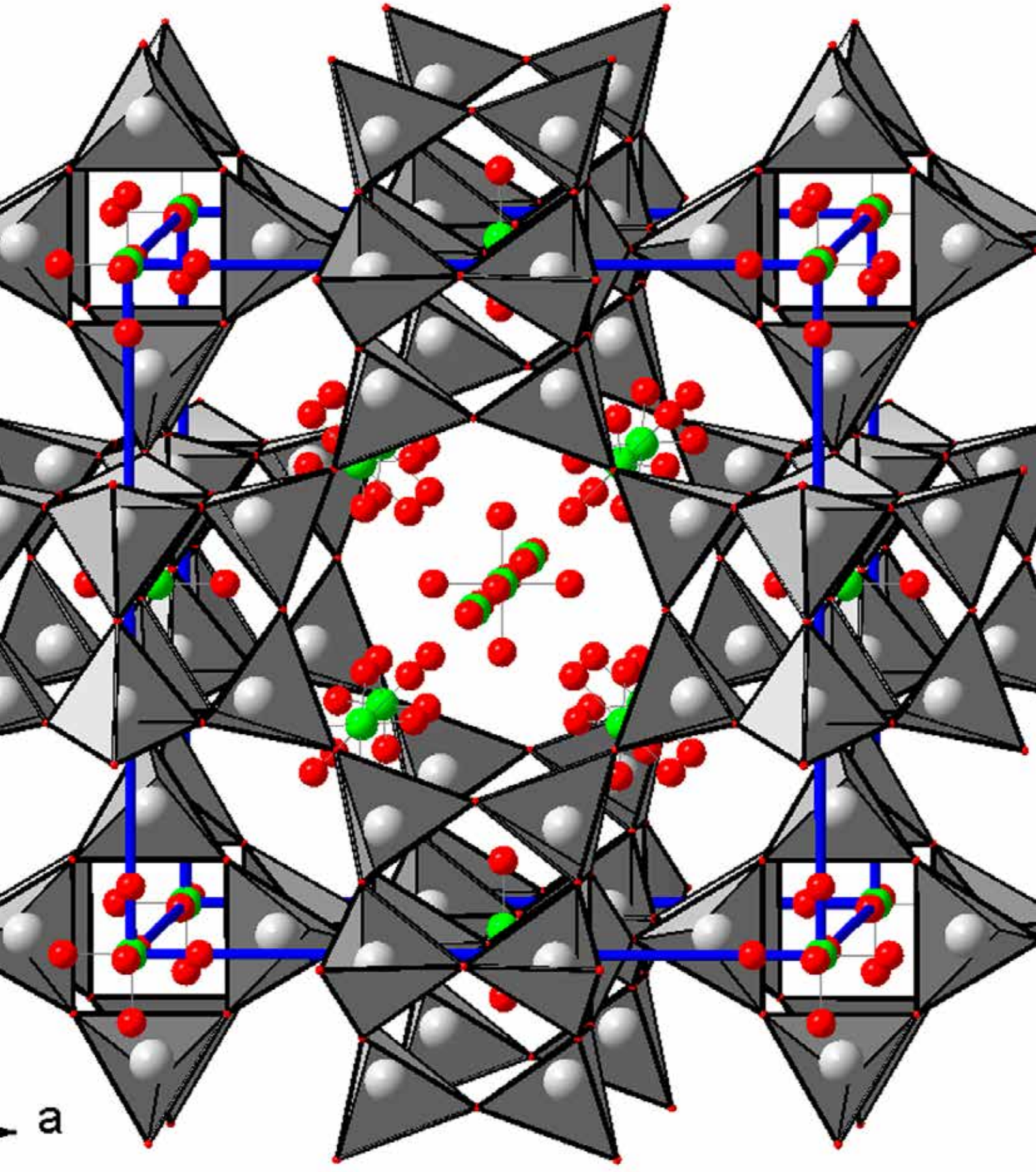

Courtesy of David Santamaría.

Pair distribution function and Rietveld analyses to characterize aluminum hydroxide gel in cement pastes

Aluminum hydroxide gel characterization within a calcium aluminate cement paste by combined Pair Distribution Function and Rietveld analyses *Cement and Concrete Research* 96 1-12 (2017)

Ana Cuesta[1,3*], Rodrigo U. Ichikawa[2], Diana Londono-Zuluaga[3], Angeles G. De la Torre[3], Isabel Santacruz[3], Xavier Turrillas[1,4], Miguel A.G. Aranda[1,3]

The main aim of this work is to better characterize nanocrystalline gels formed in cement hydration by using quantitative PDF analyses jointly with Rietveld methodology.

The analysis of amorphous/nanocrystalline phase(s) within cement matrices that contain high amounts of crystalline phase(s) is very challenging. Synchrotron techniques can be very useful to characterize such complex samples [1]. In particular, atomic pair distribution function (PDF) analysis of total scattering powder diffraction data can give information about the local structure of those components. The PDF approach jointly with Rietveld methodology allows us to have a better insight about the nanocrystalline/microcrystalline components which coexist in cement pastes.

In calcium aluminate cement (CAC) hydration, amorphous/nanocrystalline aluminum hydroxide coexists with other crystalline materials as a result of the hydration reactions [2]. Its main phase is $CaAl_2O_4$ [2] and its hydration mechanism depends on the temperature, as different crystalline phases can be formed with temperature [2-3]. CAC is used for special applications. Its main advantages are: high early strength development, chemical resistance and workability and rapid strength development at low temperatures. Depending on humidity and temperature some phase conversion can occurs which is very dangerous because it can cause an increase in concrete porosity and a loss of strength. For this reason, it is key to study the nanocrystalline/amorphous gels included in the cement matrices.

Four reference samples and one model specimen containing aluminum hydroxide gel have been investigated in this work. The reference materials were commercial crystalline gibbsite, commercial amorphous aluminum hydroxide, laboratory-synthesized boehmite and laboratory-synthesized hydrogarnet. The model sample, prepared from the hydration of $CaAl_2O_4$, contained hydrogarnet and aluminum hydroxide gel. Total scattering data were collected at MSPD beamline using the Mythen detector.

The raw PDF data for all the samples are displayed in Fig. 42. The PDF signal for crystalline gibbsite had only the features expected from the crystal structure of gibbsite, including the peaks at 1.91 Å due to Al-O_{oct}, 2.40 Å related with Al···H and O···O and 2.85 Å due to Al···Al and O···O first-shell interatomic distances. For commercial amorphous aluminum hydroxide, only interatomic peaks up to a correlation length of ~6 Å are observed.

The PDF data for the hydrogarnet sample was fitted with the crystal structure determined from the Rietveld study. The R_W converged to 15.2% and the unit cell value for hydrogarnet was a=12.585 Å.

The PDF data for boehmite was more complex due to the presence of two main phases. Boehmite is crystalline and aluminum oxide is nanocrystalline. The crystalline boehmite was fitted in high r region, 30-50 Å, where no contributions from nanocrystalline/amorphous phases were apparent. The fit is displayed in Fig. 43 (right) and the R_W value was 19.8%. Then, the contribution from nanocrystalline aluminum oxide was refined in a lower region, from 1.5 to 30 Å, see Fig. 43 (left). The final R_W value in this region converged to 26.7%. In addition, for nanocrystalline aluminum oxide, the diameter of the nanoparticle was also adjusted, obtaining a value close to 2 nm. For this mixture, the quantitative analysis gave 66.6 wt% of aluminum oxide and 33.4 wt% of crystalline boehmite.

For the hydrated $CaAl_2O_4$ paste, which contained crystalline hydrogarnet and nanocrystalline gibbsite, the PDF data in the high r-region, 60 to 80 Å, was fitted with the crystal structure of crystalline hydrogarnet, see Fig. 44c. The R_W converged to 14.9%. Then, all the parameters were kept fixed and the r-region, 1.5-60 Å, was used to fit the contribution of the nanocrystalline aluminum hydroxide gel contribution. The final R_W was 21.0%, see Fig. 44 b and a. The phase contents were 42.0, 52.8 and 5.2 wt% for hydrogarnet, $Al(OH)_3$ and monocarbonate, respectively. Moreover, the diameter of the nanoparticle, aluminum hydroxide gel, converged to 5.3 nm.

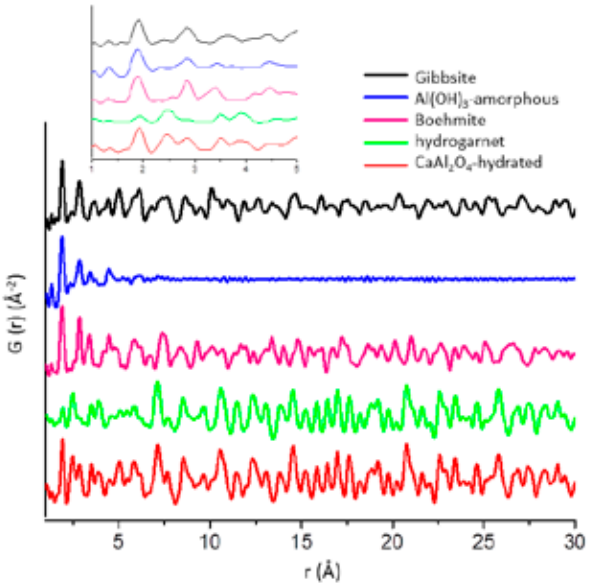

Figure 42: Experimental PDF traces for as-received commercial crystalline gibbsite, as-received commercial amorphous aluminum hydroxide, boehmite, hydrogarnet and a hydrated $CaAl_2O_4$ sample.

Additionally, authors have investigated a Ca_3SiO_5 paste, the main phase of Ordinary Portland cements. Its PDF analysis showed that a defective tobermorite, $Ca_{11}Si_9O_{28}(OH)_2 \cdot 8.5H_2O$, gave the best fits for the nanocrystalline gel [4]. Furthermore, the difference curve of the PDF analysis demonstrated that the calcium silicate hydrate gel also contains monolayers of amorphous calcium hydroxide, see Figure 45.

Commercial crystalline gibbsite was demonstrated to be a single phase and the PDF measurements indicated that its amorphous content was negligible. The amorphous aluminum hydroxide presented a very complex PDF profile with very small scattering

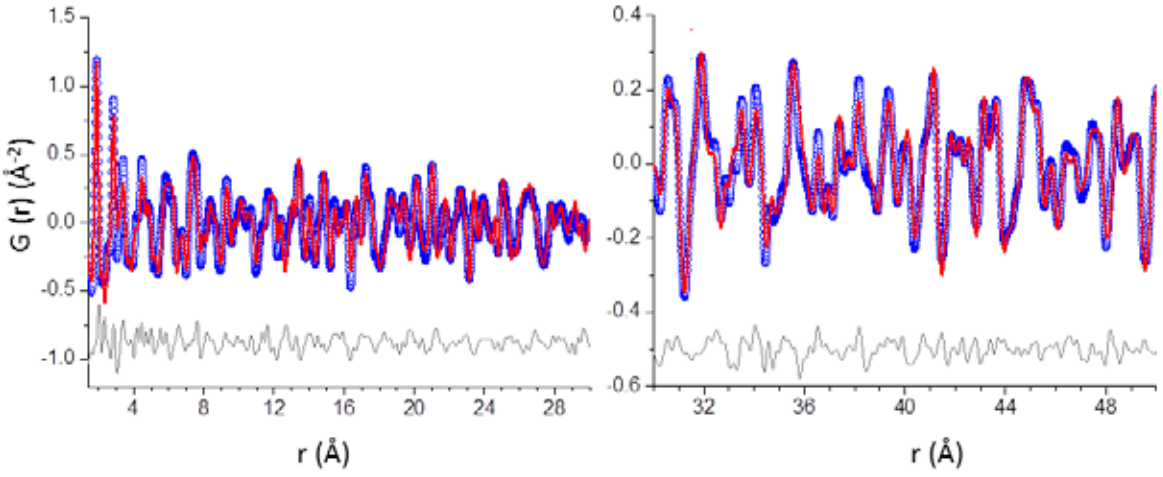

Figure 43: Experimental (blue circles) and fitted (red solid line) PDF patterns for boehmite (left) from 1.4 to 30 Å and (right) from 30 to 50 Å.

domains with size close to 0.6 nm. The mixture of crystalline boehmite and nanocrystalline aluminum oxide had an average size of aluminum oxide nanoparticles close to 2 nm. The key hydrated aluminate paste mainly contained crystalline hydrogarnet, 43 wt%, and nanocrystalline gibbsite gel, 50 wt%. The presence of amorphous content in this paste was discarded. Moreover, the PDF analysis revealed that this gel had a gibbsite local structure with an average nanoparticle size close to 5 nm. Finally, accurate phase contents can be derived from PDF analyses as compared to well-established Rietveld quantitative analysis (for crystalline phases).

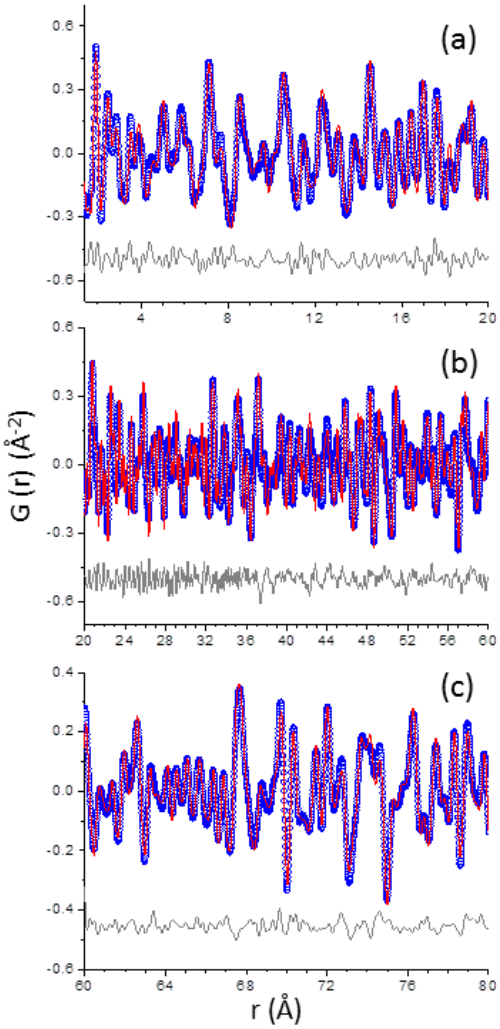

Figure 44: Experimental (blue circles) and fitted (red solid line) PDF traces for $CaAl_2O_4$-hydrated (a) from 1.4 to 20 Å, (b) from 20 to 60 Å and (c) from 60 to 80 Å.

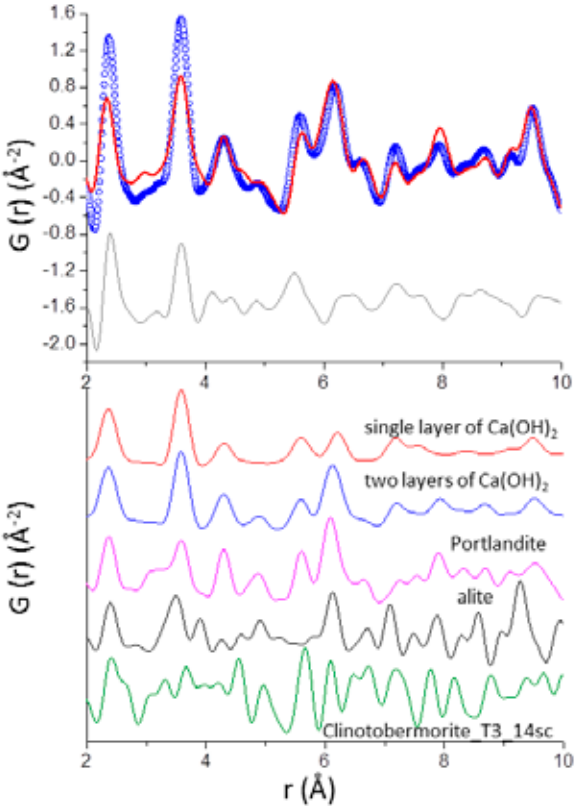

Figure 45: Experimental (blue circles) and fitted (red solid line) PDF patterns for Ca_3SiO_5 w/s=0.80 paste in the 2 to 10 Å r-range. The difference curve is shown as a grey line. Simulated PDF curves for monolayer and a double layer of calcium hydroxide, crystalline portlandite, alite and clinotobermorite T3_14sc are also included.

ACKNOWLEDGEMENTS

This work was supported by Spanish MINECO through BIA2014-57658-C2-1-R and BIA2014-57658-C2-2-R, which is co-funded by ERDF research grants. R.U.I. acknowledges funding of CNPQ, grant no. 206983/2014-0/SWE.

OTHER REFERENCES

1. M.A.G. Aranda, Recent studies of cements and concretes by synchrotron radiation crystallographic and cognate methods, Crystallogr. Rev. **22** (2016) 150-196.

2. H. Pöllmann, Calcium Aluminate Cements – Raw Materials, Differences, Hydration and Properties, Rev. Mineral. & Geochem. **74** (2012) 1–82.

3. H.F.W. Taylor, Cement Chemistry, Thomas Telford, London, 1997.

4. A. Cuesta, J.D. Zea-Garcia, D. Londono-Zuluaga, A.G. De la Torre, I. Santacruz, O.Vallcorba, M.A.G. Aranda, Synchrotron Radiation Pair Distribution Function Analysis of Gels in Cements, Crystals **7** (2017) 317.

AFFILIATION:

1. ALBA Synchrotron, Carrer de la Llum, 2-26, E-08290 Cerdanyola del Vallés, Barcelona, Spain.
2. IPEN-Institute of Energy and Nuclear Research, Av. Prof. Lineu Prestes, 2242 - Cidade Universitária, São Paulo, SP, 05508-000, Brazil.
3. Department of Inorganic Chemistry, University of Malaga, Campus Teatinos S/N, 29071 Málaga, Spain.
4. Institute of Materials Science of Barcelona – CSIC, UAB Campus, 08193 Cerdanyola del Vallès, Barcelona, Spain.

Characterization of the ultra-high CO_2-loaded pure-silica LTA zeolite upon compression

Structural evolution of CO2-filled pure silica LTA zeolite under high-pressure high-temperature conditions. *Chemistry of Materials*, 29, 4502-4510 (2017)

David Santamaría-Pérez[1,*], Tomas Marqueño[1], Javier Ruiz-Fuertes[1,2], Raquel Chuliá-Jordan[1], Daniel Errandonea[1], Simon MacLeod[3,5], Catalin Popescu[4]

Zeolites are tridimensional silicate compounds containing systems of large cavities interconnected by channels such that the enclosed ions or molecules can readily diffuse through the crystal. These microporous materials have a wide range of utilities based on their selective cation-exchange ability (i.e. molecular sieves) and catalytic properties, and they are used in different fields such as oil industry, construction industry, water treatment or storage of nuclear waste.

Penetrability of external molecules in zeolites at high pressure is known to be governed by several variables, among which, the most important ones are: the diameter of the cavities, the pressure of the penetrating molecular fluid, the temperature at which the experiment is conducted or the chemical nature and configuration of the extra-framework population [1,2]. Pure silica zeolitic frameworks like LTA-ITQ29 avoid the latter of these variables and give us the opportunity of examining the effect of pressure and temperature without interferences of charge-balancing cations. This study provides the structural characterization of the CO_2-loaded LTA-SiO_2 zeolite at full adsorption capacity and equilibrium conditions. We report the preferred (most stable) sorption sites of 13 CO_2 molecules per unitcell and discuss the crystal-fluid interactions at high-pressure high-temperature conditions.

The crystal structure of CO_2-filled pure-SiO_2 LTA zeolite has been studied at high pressures and high temperatures by means of *in situ* synchrotron x-ray powder diffraction. Experiments were carried out at the MSPD and GSECARS beamlines in ALBA and APS synchrotrons, respectively, using diamond-anvil cells (DACs) loaded with pure silica zeolite A [3] and high-purity CO_2. For high temperature measurements, the DAC was contained within a custom-built vacuum vessel and wrapped by a coiled heater [4]. The existence of CO_2 in the zeolite cages at 0.5 GPa was apparent from the abrupt change in the XRD peak intensity ratios between the empty and the observed zeolite patterns. The exact CO_2 content and the position of the hosted CO_2 molecules within the structure could be completed by Rietveld refinement and Fourier recycling [5]; i.e., the electron density map from difference Fourier calculations allowed us to locate the guest molecules in the porous structure. Thus, a total of 13 CO_2 molecules are accommodated in the LTA zeolitic cavities, 12 in the large α-cages and one in the β sodalite cages (see Fig. 46), giving a final stoichiometry $(CO_2)_{13}[SiO_2]_{24}$.

The initial cubic structure undergoes a second-order displacive phase transition to a rhombohedral structure at approx. 1.2 GPa, which is basically a distorsion caused by the compression along the diagonal of the cubic unitcell. This structure remains stable under a pressure of at least up to 20 GPa, indicating that the pressure-induced amorphization

is prevented by the insertion of CO_2 molecules in the open framework.

The ambient-temperature lattice compressibility and thermal expansivity at P~5 GPa were determined. The bulk modulus of this filled zeolite (B_0= 39(3) GPa) is comparable to that of α-quartz and entails direct compression of the silica framework. As for the high-temperature measurements, our data confirmed that the insertion of CO_2 reverses the negative thermal expansion of the empty zeolite structure by minimizing the [SiO_4] tetrahedral tilting. What's more, we found that the structure of the CO_2-filled ITQ-29 framework recovers the initial cubic symmetry when the CO_2 acting as pressure transmitting medium becomes liquid. This result points to a high sensitivity of the zeolite to surrounding nonhydrostatic conditions, since even a soft solid medium like the CO_2-I molecular phase produces structural distortions at relatively low pressures.

The analyses of the interatomic distances between the atoms of the CO_2 guest molecules and the atoms of the SiO_2 host framework reveal that pressures above 30 GPa will be required to bring atoms close enough to enhance the potential chemical activity and synthesize a possible silicate carbonate.

In summary, authors have determined the structural behavior of the ultra-high CO_2-loaded pure-silica LTA zeolite under high-pressure high-temperature conditions and provided a detailed overview of the phase diagram in this CO_2:SiO_2 system. The usual compression mechanism in LTA zeolite observed in high-pressure experiments using non-penetrating pressure media, which involved the collapse of the structure around the empty pores and the formation of the denser ITQ-50 zeolite [6], is hindered by the presence of guest CO_2 molecules. Results indicate that the insertion of carbon dioxide leads to the deactivation of the pressure-induced amorphization mechanism, the ITQ-29 material being retained in a slightly distorted rhombohedral form to pressures of at least 20 GPa. X-ray powder diffraction data at low pressures allow researchers to determine the location of the guest molecules in the cage, which is a critical step for understanding the existing host-guest atomic interactions. A total of 13 molecules of carbon dioxide per unitcell were accommodated in the α- and β-cages of this silica-pure zeolite structure, providing a SiO_2:CO_2: content ratio lower than 2.

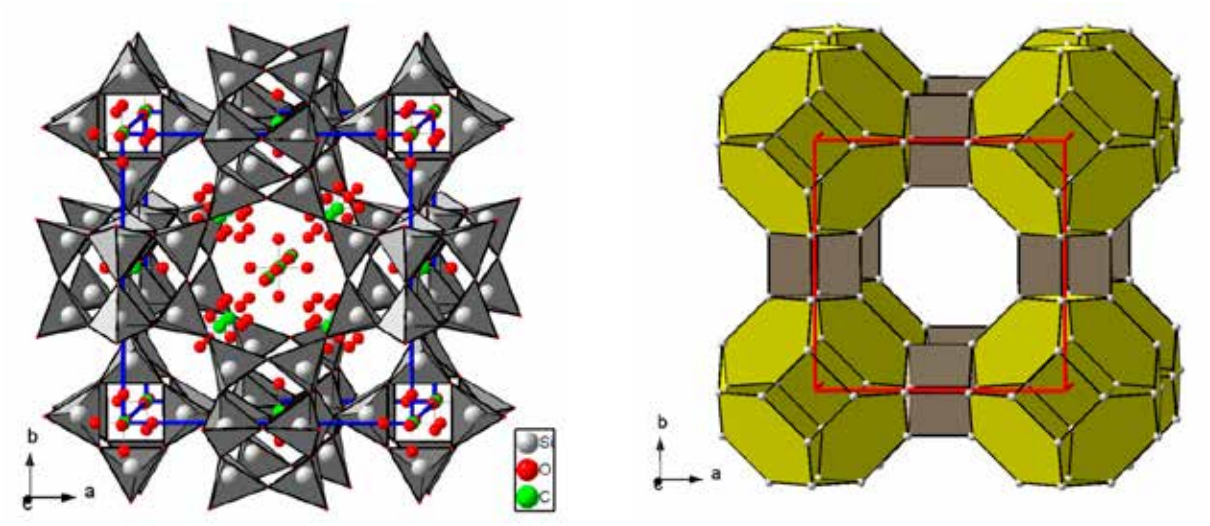

Figure 46: (Left) Packing of polyhedra formed by the host [SiO_4]-based framework in pure-silica LTA zeolite. The large α-cage is in the center of the unit cell and the β sodalite cage, in yellow, is in the unit cell corner. (Right) The same framework structure showing the [SiO_4] connectivity and the location of CO_2 molecules at 0.5 GPa. Grey, green and red spheres represent Si, C, and O atoms, respectively. *Copyright 2017. American Chemical Society.*

ACKNOWLEDGEMENTS

The authors thank the financial support of the Spanish Ministry of Economy and Competitiveness (MINECO), the Spanish Research Agency (AEI) and the European Fund for Regional Development (ERDF) under Grants No. MAT2016-75586-C4-1-P, MAT2015-71842-P, Severo Ochoa SEV-2012-0267 and No.MAT2015-71070-REDC (MALTA Consolider). D. S-P. and J. R-F acknowledge MINECO for a Ramón y Cajal (RYC-2014-15643) and a Juan de la Cierva (IJCI-2014-20513) contract, respectively. Portions of this work were performed at GeoSoilEnviroCARS (Sector 13), Advanced Photon Source (APS), Argonne National Laboratory. GeoSoilEnviroCARS is supported by the National Science Foundation - Earth Sciences (EAR-1128799) and Department of Energy (DE-FG02-94ER14466, DE-AC02-06CH11357). Authors thank ALBA Synchrotron for beamtime allocation at MSPD. British Crown Owned Copyright 2017/AWE. Published with permission of the Controller of Her Britannic Majesty's Stationery Office.

OTHER REFERENCES

1. G.D. Gatta, P. Lotti, G. Tabacchi. The effect of pressure on open-framework silicates: elastic behavior and crystal-fluid interaction. Phys. Chem. Minerals. **2017**, DOI: 10.1007/s0026.

2. T. Marqueño, D. Santamaria-Perez, J. Ruiz-Fuertes, R. Chulia-Jordan, J.L. Jorda, F. Rey, C. McGuire, A. Kavner, S. MacLeod, D. Daisenberger, C. Popescu, P. Rodriguez-Hernandez, A. Muñoz. An ultrahigh CO2-loaded silicalite zeolite: Structural stability and physical properties at high pressures and temperatures. *Inorg. Chem.* **2018**, *57*, 6447-6455

3. A. Corma, F. Rey, J. Rius, M.J. Sabater, S. Valencia, Supramolecular self-assembled molecules as organic directing agent for synthesis of zeolites. *Nature*, **2004**, *431*, 287 – 290.

4. D. Santamaria-Perez, J. Ruiz-Fuertes, T. Marqueño, J. Pellicer-Porres, R. Chulia-Jordan, S. MacLeod, C. Popescu. Structural behavior of natural silicate-carbonate spurrite mineral, Ca5(SiO4)2(CO3), under high-pressure, high-temperature conditions. *Inorg. Chem*. **2018**, *57*, 98-105.

5. A.N. Fitch, H. Jobic, A. Renouprez. Location of benzene in sodium-Y zeolite by powder neutron diffraction. *J. Phys. Chem.* **1986**, *90*, 1311-1318.

6. J.L. Jordá, F. Rey, *et al*. Synthesis of a novel zeolite through a pressure-induced reconstructive phase transition process. *Angew. Chem. Int. Ed.*, **2013**, *52*, 10458-10462.

AFFILIATION:

1. Department of Applied Physics-ICMUV, MALTA, University of Valencia, 46100, Valencia, Spain.
2. DCITIMAC, MALTA, University of Cantabria, 39005 Santander, Spain.
3. Atomic Weapons Establishment, Aldermaston, Reading, RG7 4PR, UK.
4. ALBA Synchrotron, 08290, Cerdanyola, Spain.
5. School of Physics & Astronomy, and Centre for Science at Extreme Conditions, The University of Edinburgh, Edinburgh, EH9 3FD, UK.

Transforming C_{60} into graphene on Cu foils: procedure and characterization

High-quality PVD graphene growth by fullerene decomposition on Cu foils, *Carbon* 119, 535 (2017)

J. Azpeitia[1], G. Otero-Irurueta[2], I. Palacio[1], J. I. Martinez[1], N. Ruiz del Árbol[1], G. Santoro[1], A. Gutiérrez[3], L. Aballe[4], M. Foerster[4], M. Kalbac[5], V. Vales[5], F. J. Mompeán[1], M. García-Hernández[1], J. A. Martín-Gago[1], C. Munuera[1], M. F. López[1]

A new strategy to grow large-area high-quality graphene from C_{60} is presented. Following a multitechnique characterization (μ-LEED, AFM, Raman, XPS, ARPES, SEM, EBSD) the quality of these layers is evaluated.

C_{60} molecules were used as carbon source to grow large-area high-quality graphene layers on polycrystalline Cu foils. The graphene growth process was performed in UHV conditions and was thermally promoted by annealing the substrate at 800 ºC during evaporation of C_{60} molecules. Several surface characterization techniques were applied to evaluate the quality of the graphene layer. *In-situ* low-energy electron diffraction (LEED) images show spots corresponding to a polycrystalline Cu surface with predominance of (110) faces and the typical LEED graphene ring. *Ex-situ* atomic force microscopy (AFM) and Raman spectroscopy were used to determine the quality and thickness of the graphene layer. This confirmed the existence of a graphene layer that extends over large areas. Angle-resolved photoemission spectroscopy (ARPES) measurements were performed to unveil the linear behaviour of electrons near the Dirac point. Additionally, the X-ray photoelectron spectroscopy (XPS) experiments showed the C1s XPS core level signature of clean graphene layers. Raman spectra show lower intensity signal just after graphene growth than after ageing, probably due to the decoupling induced by oxygen intercalation. It could be also verified that the present new protocol is a self-limiting process leading exclusively to one single graphene layer.

Graphene was prepared by evaporating C_{60} on polycrystalline copper at 800 ºC in UHV. Fig. 47a represents the μ-LEED pattern acquired at 40 eV after graphene growth on Cu foil showing a ring and multiple spots mainly with rectangular crystallographic order. The ring is the fingerprint of polycrystalline graphene while the multiple spots correspond mainly to the substrate (110) grains. Electron backscattered scattering diffraction (EBSD) measurements (see Fig. 47b) corroborate this preferred (110) orientation.

XPS and Raman spectroscopy were performed to evaluate the graphene quality. Fig. 48a shows the XPS C-1s spectrum of the graphene/Cu foil, acquired after exposing the sample to air, without any cleaning treatment. The spectrum was fitted with five subspectra assigned to C-sp2, C-OH, C-O, C=O, and C-C=O together with O-C=O species (284.4, 285.4, 286.7, 288.5 and 290.5 eV, respectively). The strong intensity of the C-sp2 component with respect to the oxide components evidences, even after air exposure, the high quality of the graphene layer. The combination of UHV conditions and low temperatures involved in the growth process ensures a more controlled and cleaner procedure than other methods.

Fig. 48b exhibits the Raman spectra of the graphene layer in the case of a freshly prepared graphene sample (red curve) and two months after growth (black curve). The red spectrum exhibits the G, 2D and D peaks that are distinctive of graphene although with very low intensity. Interestingly, the black curve exhibits those peaks but with a larger intensity. It is important to remark that no differences were observed by AFM in the morphology of the sample after ageing two months, suggesting that the increase in the signal is related to the evolution of the graphene/Cu interface. This suggests the formation of copper oxide in the interface by oxygen intercalation from the atmosphere. The calculated integrated I_{2D}/I_G ratio gives a value of 5.2, which supports the presence of a monolayer of graphene.

The authors present a new protocol to grow high-quality graphene on Cu foils using C_{60} as precursor molecules in UHV conditions. The growth mechanism involves the thermally activated decomposition of the C_{60} molecules on the Cu surface. The present approach introduces some advantages with respect to the use of hydrocarbons. From one side, it is a self-limiting process that gives rise only to one single graphene layer. On the other hand, it requires lower substrate temperatures than other conventional methods, as CVD, and therefore results in a clean graphene-copper interface. A multitechnique characterization was performed to evaluate the quality of the graphene layer grown by this protocol. Thus, all the results show that our protocol leads to a large-area high-quality graphene layer.

ACKNOWLEDGEMENTS

The authors thank the financial support from EU Horizon 2020 research and innovation program under grant agreement No. 696656 (GrapheneCore1-Graphene-based disruptive technologies) and the Spanish MINECO (grants MAT2014-54231-C4-1-P, MAT2014-52405-C2-2-R, CSD2009-00013, FPI BES-2012-058600 and FPI BES-2015-072642, RYC-2014-16626 and RYC-2015-17730). JIM and GS are supported by the ERC-Synergy Program (grant ERC-2013-SYG-610256 Nanocosmos). MK and VV acknowledge funding from ERC-CZ (LL1301) project. GO-I acknowledges FCT for his grant (SFRH/BPD/90562/2012).

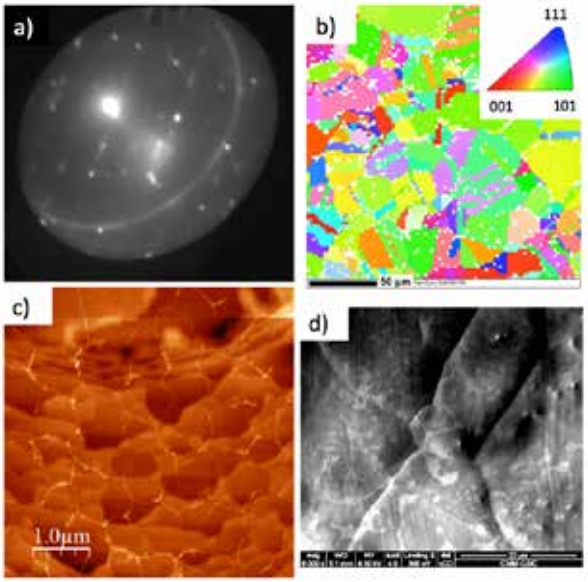

Figure 47: a) μ-LEED pattern, b) EBSD map (inset showing the color code) and c) AFM image of the graphene/Cu sample after growth. d) SEM image of an incomplete graphene layer.
Figure 47c shows an AFM image revealing the presence of different atomic steps delimiting terraces within a Cu grain and the graphene wrinkles. Fig. 46d exhibits the special case of a partial graphene layer on Cu as depicted by scanning electron microscopy (SEM), which reveals that graphene crosses the boundaries between neighboring Cu crystallographic domains, extending over different Cu grains. The uncovered Cu areas appear lighter than those from graphene.

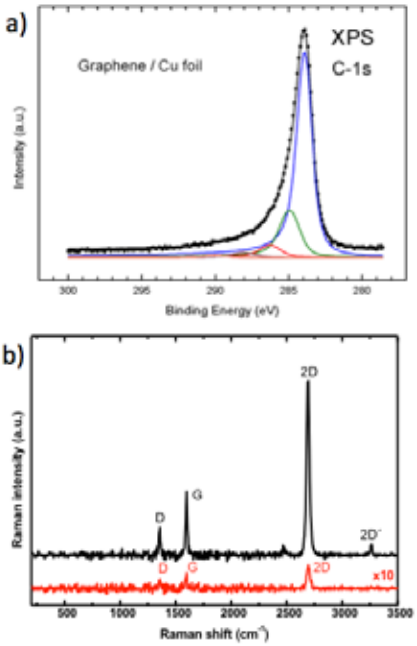

Figure 48: a) XPS C-1s core level spectrum of the graphene layer on the Cu foil, b) Raman spectra of a freshly prepared (red) and aged (black) graphene layer.

AFFILIATION:

1. Materials Science Factory, Institute of Materials Science of Madrid (ICMM-CSIC), Sor Juana Inés de la Cruz 3, E-28049 Madrid, Spain.
2. Center for Mechanical Technology and Automation (TEMA-DEM), University of Aveiro, 3810-193 Aveiro, Portugal.
3. Department of Applied Physics, Autonomous University of Madrid, E-28049 Madrid, Spain.
4. ALBA Synchrotron Light Facility, Carrer de la llum 2-26, Cerdanyola del Vallès, Barcelona 08290, Spain.
5. J. Heyrovský Institute of Physical Chemistry, ASCR, v.v.i., Dolejškova 3, CZ-18223 Prague 8, Czech Republic.

INDUSTRIAL
LIAISON OFFICE

Relations with the industry

Núria Valls, Marta Ávila and Alejandro Sánchez
Industrial Liaison Office

One of the goals of ALBA is to provide scientific and technological support to the companies to increase their competitiveness and their societal impact.

Synchrotron techniques for industry

2017 has been the most successful year in both industrial access and number of companies using the ALBA synchrotron techniques. Industrial beamtime usage was the highest ever, almost ten-fold bigger than in the first year of ALBA industrial activity in 2013 (Figure 49), while a total of 22 national and international different companies took profit from the state-of-the-art techniques available at ALBA. Among these companies, 14 of them were already industrial users of ALBA, whereas 8 were new customers, therefore boosting the portfolio of proprietary clients of ALBA. About half of the industrial experiments corresponded to the pharmaceutical sector, and the other half was related to nanotechnology, chemistry, catalysis and, to a lesser extent, automotive and energy (Figure 50).

For the first time, in 2017 all ALBA beamlines had industrial experiments. This is a clear proof that all the advanced characterization techniques available at ALBA are useful for industrial applications, as is expected to be the case with the forthcoming techniques, corresponding to beamlines under construction, that will be available in the future.

Specialised laboratories for external proprietary users

Besides the synchrotron techniques, ALBA is offering its specialised laboratories for external proprietary access whenever there is no interference with the regular operation. This is a special feature of ALBA that allows industry to access outstanding laboratories such as the Magnetic Measurements Laboratory, the Radiofrequency Laboratory and the Optics and Metrology Laboratory. This year, other activities related to supporting laboratories expertise were reinforced with different training courses on low-level radiofrequency and Sardana software provided to different synchrotron facilities by specialised staff from the Accelerators and Computing Division.

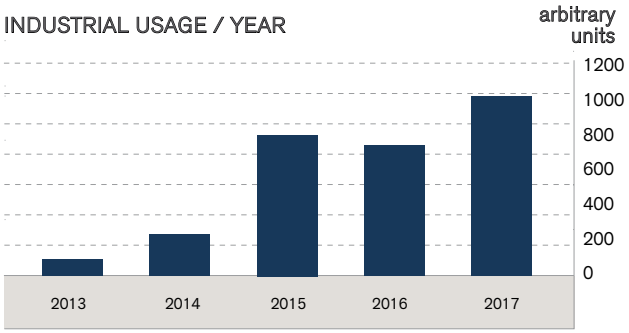

Figure 49: Evolution of industrial beamtime per year in arbitrary units.

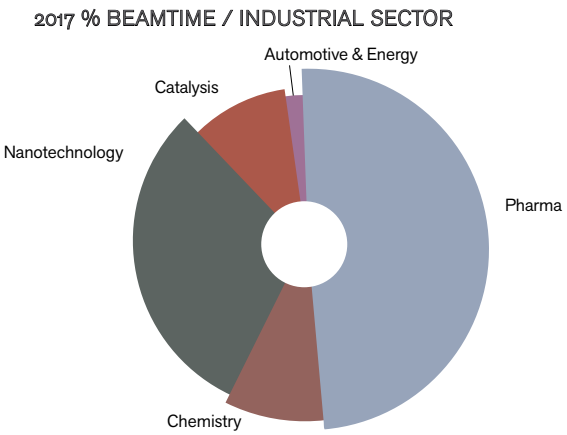

Figure 50: Distribution of beamtime per industrial sector (2017).

Long-term engagement with industry

Strong industrial relationships were also established during 2017. Six new collaboration agreements were signed with different companies and institutions such as an important contract between ALBA and Henkel for the characterization of Henkel samples and materials using the advanced and specialized synchrotron techniques available at ALBA.

Industrial outreach

Given the limited knowledge of synchrotron techniques amongst national companies,, industrial outreach activities represent a key point. ALBA has carried out a series of structured events to raise awareness of the capabilities of the synchrotron techniques among specific private sectors. This year, the industrial outreach has focused on the agrifood and packaging sectors on one hand, and on the pharmaceutical and cosmetics sectors on the other.

The workshop on agrifood and packaging, held on 12th May in the ALBA synchrotron premises with the support of the NFFA European project, gathered nearly 70 people from 30 different companies and institutions, becoming the industrial workshop with most attendees ever. After the workshop, over 10 different meetings were held with companies, and small workshops and meetings were carried out with specific research groups experts in this field. Additionally, during the EFFoST conference, the meeting of the European Federation of Food Science and Technology, a special session was dedicated to synchrotron and neutron applications.

For the first time, ALBA, with the support of the European project CALIPSOplus, has organised an industrial workshop outside ALBA, in Madrid, at CSIC premises, on 10th October focused on pharma, cosmetics and biomedicine. Given the novelty of the location, the dissemination of the workshop was strengthened by publishing different articles and interviews in two industrial journals: Farmespaña Industrial and Industria Cosmética. Over 24 attendees from 18 different companies attended the workshop. Moreover, a fruitful bio-nanotechnology networking meeting was organised at ALBA with biotech companies, hospitals and academic groups belonging to the B-30 association. Following the strategy of approaching the biomedicine sector, a series of presentations were carried out at hospitals and Pharmaceutical companies around Madrid and Barcelona by a permanent external collaborator of ALBA specialized in skin care (Prof. Manel Sabés). ALBA participated as well in in a healthcare-pharmaceutical workshop in the Cosmetorium conference, and a lecture was given during a hair training course organised by CTC (Hair Technological Center).

ALBA is an active member of the SECPhO cluster, which acts as a loudspeaker for the ALBA industrial outreach activities, and participated in innovation workshops organized by SECPhO in the fields of aeronautics, urban and industrial water management, and technical textiles.

An ALBA presentation was done in Expoquimia 2017, an International Chemical Exhibition with more than 500 industrial exhibitors, and in the 5-Continent Congress on Lasers and Aesthetic Medicine.

Industrial applications brochure

This year an industrial brochure has been created. It compiles ALBA industrial applications in a brief but comprehensive and easy-to-understand way (Figure 51). This brochure is focused on applications rather than techniques, and it is structured by industrial sectors. The benefits of synchrotron techniques in each specific field are demonstrated through examples of actual experiments performed at ALBA. In addition, the brochure contains

Figure 51: Industrial applications brochure.

Figure 52: Workshop on agri-food and packaging synchrotron industrial applications.

information about ALBA specialized supporting labs and examples of industry clients, among other information.
The brochure can be downloaded in the following link: https://www.albasynchrotron.es/en/industry/industrial-services

CALIPSOplus and SMEs access promotion

In 2017, the Horizon2020 project CALIPSOplus was launched aiming at lowering the access barriers to the light sources in Europe. ALBA Synchrotron is the leader of the work package TamaTA pursuing to facilitate small and mid-sized companies' access to European light source facilities. The first call of TamaTA has already been launched and all SMEs interested in having access to synchrotron facilities can send their proposals to the following website http://www.wayforlight.eu/eng/sme-access-proposal.aspx

This access provides both beamtime and data analysis and is highly recommended contacting the synchrotron (industrialoffice@cells.es) prior to the submission of the proposal.

Technology transfer

ALBA continuously develops new solutions to guarantee the optimal performance of the facility. Such innovative developments are offered to the industrial community as a technological transfer. In 2017 the ALBA patent portfolio was enriched with two new patent registrations. The different technology offers available for licensing are published on the ALBA website:
https://www.albasynchrotron.es/en/industry/technology-transfer

TECHNOLOGY

ALBA Digital Low Level RF

Angela Salom, Francis Pérez

The radiofrequency (RF) cavities accelerate the beam by creating high electric RF fields in the path of the particles. The low-level RF (LLRF) system is responsible for the control of the amplitude and phase of this electric field, for synchronising it with the beam and for compensating any external disturbance that may affect the stability of the beam. The initial requirements of the ALBA LLRF were to control the amplitude and phase of the RF cavity voltage within 0.5% and 0.5º respectively, as well as to adjust the resonance frequency of the cavity. Nowadays, LLRF systems are based on digital platforms with high-speed parallel processors specifically developed for digital signal processing applications (FPGAs or DSPs) and high-resolution, high-speed ADCs/DACs, which have allowed to extend their performance with respect to their original requirements. ALBA digital LLRF system is based on commercial FPGA boards with different formats (cPCI, uTCA and stand-alone platforms). The ALBA team efforts have been focused on the development of the algorithms embedded in the FPGA processors to guarantee the cavity field stability, to improve mean time between failures (MTBF) and to automate operational aspects of the RF plants in order to improve mean time to recovery (MTTR). Through several collaborations with other labs, ALBA LLRF has also been implemented in other synchrotron light sources like Max-IV, Solaris, Diamond Light Source and Sirius. Using the same hardware (HW) and main conceptual design, the system was adapted to the different needs of these labs, proving the flexibility of this kind of systems.

An RF system of a particle accelerator is composed of an RF amplifier, an accelerating cavity receiving the RF amplifier power and a control system that synchronises the cavity voltage field with the beam. RF amplifiers usually introduce ripples in the cavity field that may affect the stability of the beam. Other disturbances like thermal drifts and beam loading effects may also affect the cavity field and thus, the stability of the beam. The goal of the LLRF is to measure those disturbances and apply corrections so that the beam is not affected.

Hardware

Figure 53 shows a scheme of the DLLRF HW which consists of three main sub-systems: analogue front ends, digital boards (ADCs-FPGA-DACs) and local timing.

Analogue Front Ends: In order to measure the cavity field, the high-frequency RF signals provided by the cavity pick-up loops have to be translated into equivalent signals in terms of amplitude and phase, but with lower frequency. This task is accomplished in the analogue front ends. For doing so, the RF 500 MHz signals are mixed or multiplied by a local oscillator (LO) of 520 MHz. The LO is constant in amplitude and locked in phase with the master oscillator. After low-pass filtering the product output, the front end provides an intermediate frequency (IF) signal of 20 MHz, whose amplitude and phase are proportional to the RF signal of interest. This lower frequency signal can be connected the ADCs of the FPGA platform as shown in Figure 53.

Similarly, the control signals provided by the DACs of the digital boards are intermediate frequency signals of 20 MHz. These outputs are mixed with the 520 MHz LO to provide a 500 MHz RF signal to be sent to the RF amplifier and, from there, to the cavities.

Local Timing System: The local timing system provides the 520 MHz LO by mixing the the master oscillator signal (500 MHz) with a 20 MHz internal clock. This local timing system also provides a 80 MHz digital clock for the ADCs, DACs and FPGA of the digital boards.

Digital Boards: Commercial digital boards with fast ADCs (14 bits – 100 MHz) and fast DACs (14 bits

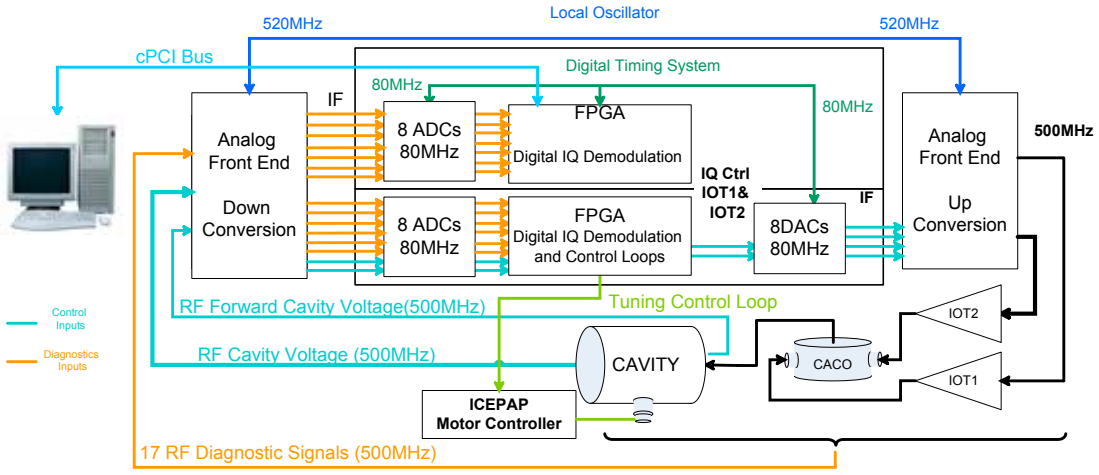

Figure 53: ALBA digital LLRF HW scheme.

– 125 MHz) and FPGAs (Xilinx Virtex-4) have been used for the LLRF. The algorithms to control the amplitude and phase of the cavity voltage and other utilities are embedded in these FPGA processors.

Software

Digital IQ demodulation: The IF signals provided by the front ends are sampled at an 80 MHz rate in the ADCs, a frequency four times higher than the IF. This provides an alternative sequence of the I and Q components (I, Q, -I, -Q...) as shown in Figure 54. The amplitude and phase of the cavity voltage can be calculated by demultiplexing this signal and applying trigonometric functions.

Amplitude and phase control loops: The amplitude and phase of the cavity voltage are controlled by a PI loop applied to the I and Q components of the cavity voltage signal. In this loop, the user can select the required voltage to be achieved and phase of the cavity. As shown in Figure 55, there are also diagnostic points at different stages of the PI loops that provide information on the loop performance, like the error, accumulated action and control signal. By adjusting the Kp and Ki values, the bandwidth of the loop can be adjusted from 1 kHz to 50 kHz. The IQ control outputs are then IQ modulated to provide 20 MHz control signals to be up-converted in the front end.

Tuning loop: Due to thermal effects, the cavity walls may expand or contract changing its resonance frequency. When this happens, the RF power of the cavity gets reflected. To avoid this, a cylinder (tuner) is inserted inside the cavity body in order to keep its inner volume constant. When the cavity is on resonance or on tune, the phase difference between the forward power and the cavity voltage is zero. The FPGA calculates this phase difference through the CORDIC algorithm, an iterative process capable of computing trigonometric functions with few processing resources. Whenever the cavity is out of tune, the FPGA sends the command to move this tuner either inwards or outwards the cavity body to maintain the cavity on tune, compensating thermal and any other effects.

Extra Utilities

Taking advantage of the flexibility and capabilities of the digital system, the LLRF has been expanded to provide extra utilities on top of the loops described previously. These are:

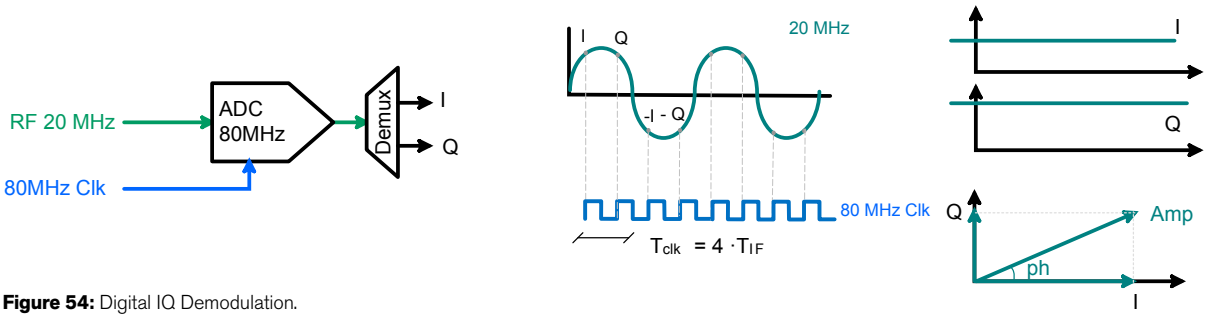

Figure 54: Digital IQ Demodulation.

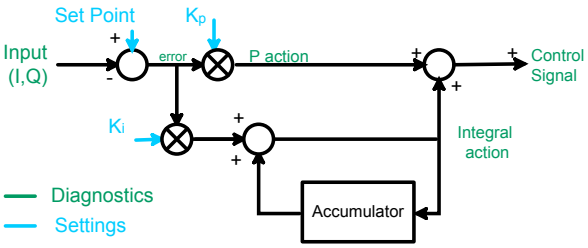

Figure 55: Amplitude and phase (I-Q) PI Loop.

Fast data logger: a 128 MB RAM integrated in the digital board is constantly storing up to 32 diagnostic signals, at an 80 MHz rate, on the DSP implemented in the FPGA. This data is retrieved when an interlock is detected in the machine in order to provide information on the cause of the interlock. Up to 418 ms of data can be recovered.

RF trip compensation: if one of the six RF cavities of the ALBA Storage Ring is stopped, the RF voltage sudden drop will introduce longitudinal oscillations in the beam, which will in turn produce an oscillation of the overall cavity voltage that may lead to a beam loss. In order to dampen these oscillations, a phase and amplitude modulation have been introduced in the LLRF drive (feed-forward loop). This special mode was introduced in 2013 and it has improved the robustness of the RF system against interlocks and at the same time allowed increasing the storage ring beam current with the reliability required by users [1].

Automatic conditioning: in this special operation mode, used to prepare the cavity's vacuum for high power, the RF power is square modulated at 10 Hz. The duty cycle and top of the pulses are increased automatically by the LLRF depending on the vacuum pressure of the cavity. This mode reduced the conditioning time of cavities from weeks to days.

Automatic recovery with beam: the recovery of cavities after an interlock can be done with a circulating beam in the SR in less than 3 minutes, reducing the MTTR and increasing the reliability of the RF systems.

Slave loops for balance compensation of amplifiers combination: These loops compensate small power imbalances of amplifiers being combined, avoiding phase errors that can cause reflected power interlocks.

Extra diagnostics: up to 19 RF signals are monitored in each LLRF. In some cases, up to 4 RF signals are sampled using the same ADC through multiplexer controlled by the FPGA, reducing the cost of input channels and providing a wide overview of the whole RF plant status, as shown in Figure 53.

Step response analysis for control loop studies: A special function in the LLRF allows the user to introduce a step in the loop reference (open and close loop) to study the dynamic behavior of the RF plant, a useful tool for the right optimization of the loops.

Booster ramping and field flatness control for multi-cells cavities: in the Booster, the energy of the particles is ramped from 100 MeV to 3 GeV and the power of the RF plant should also be ramped synchronously with the beam. Special settings were developed in the LLRF to provide a flexible ramp profile, where the user can specify the power at top and bottom of the ramp, the time periods of the ramp (top, bottom, ramping up and ramping down) and synchronized with injection/extraction of the beam. Another tuning algorithm called "field-flatness" also checks the homogeneous distribution of the RF field among the 5 cells of the Booster cavity and applies correction when needed.

New LLRF System: uTCA and stand-alone

The present ALBA LLRF is based on cPCI Boards and Windows XP drivers, which are no longer suitable for new developments. For this reason, ALBA developed a new LLRF based on a commercial uTCA platform for the collaborations established with other labs: Max-IV, Solaris, Diamond and Sirius. Figure 56 shows a scheme of this new hardware based on uTCA, a standard widely used in accelerators electronics [2, 3, 4].

The firmware and main HW components of the LLRF remain (front ends, timing and digital boards), but the FPGA processor has been upgraded to Virtex-6 family, providing ten times more processing resources for the same cost. This allowed the integration of the control of two cavities in one single LLRF, reducing the HW costs.

LLRF configurations: Several configurations have been implemented in this new LLRF to meet the different requirements of the different synchrotron's accelerators. The main characteristics are:

- Up to two cavities control in one LLRF system (normal or super conducting)
- Up to 4 RF drives

- Up to two plungers control for multi-cells cavities
- Up to 48 RF Inputs

LLRF New Utilities

- Polar loops control: independent control for amplitude and phase with different bandwidths
- Slow and fast rectangular loops with adjustable bandwidth from 0.1 Hz to 50 kHz
- Fast interlocks handling to cut RF drive in less than 10us if a problem is detected
- Landau cavities tuning control

Test results

The performance of the LLRF exceeds the initial requirements, with the following results:

The amplitude and phase resolution with the cPCI and uTCA ALBA LLRF is 0.14% rms and 0.08º as shown in Figure 57.

The achieved long-term stability (10 h) is better than 0.1% in amplitude and 0.1º in phase, as shown in Figure 58.

The dynamic range was tested and proved to be more than 30 dB (from 80 W to 80 kW).

Conclusions

ALBA LLRF systems have been in operation for more than 10 years, providing good reliability and performance. The flexibility and computational resources of FPGAs have allowed expanding the utilities of the LLRF and include automation of operational process, improving MTTR.

The diagnostic implemented in the LLRF allowed a better understanding of the dynamics of the beam and therefore the implementation of feed-forward algorithms for interlocks compensations, improving the MTBF.

The settings of the LLRF are easily adjustable to meet requirements of different operation machines. For this reasons, ALBA LLRF was adapted, installed and commissioned in other synchrotron labs (DIAMOND, SOLARIS, MAXIV and SIRIUS).

ALBA is presently working on the upgrade of LLRF HW and further developing improvements of the utilities to increase reliability and performance.

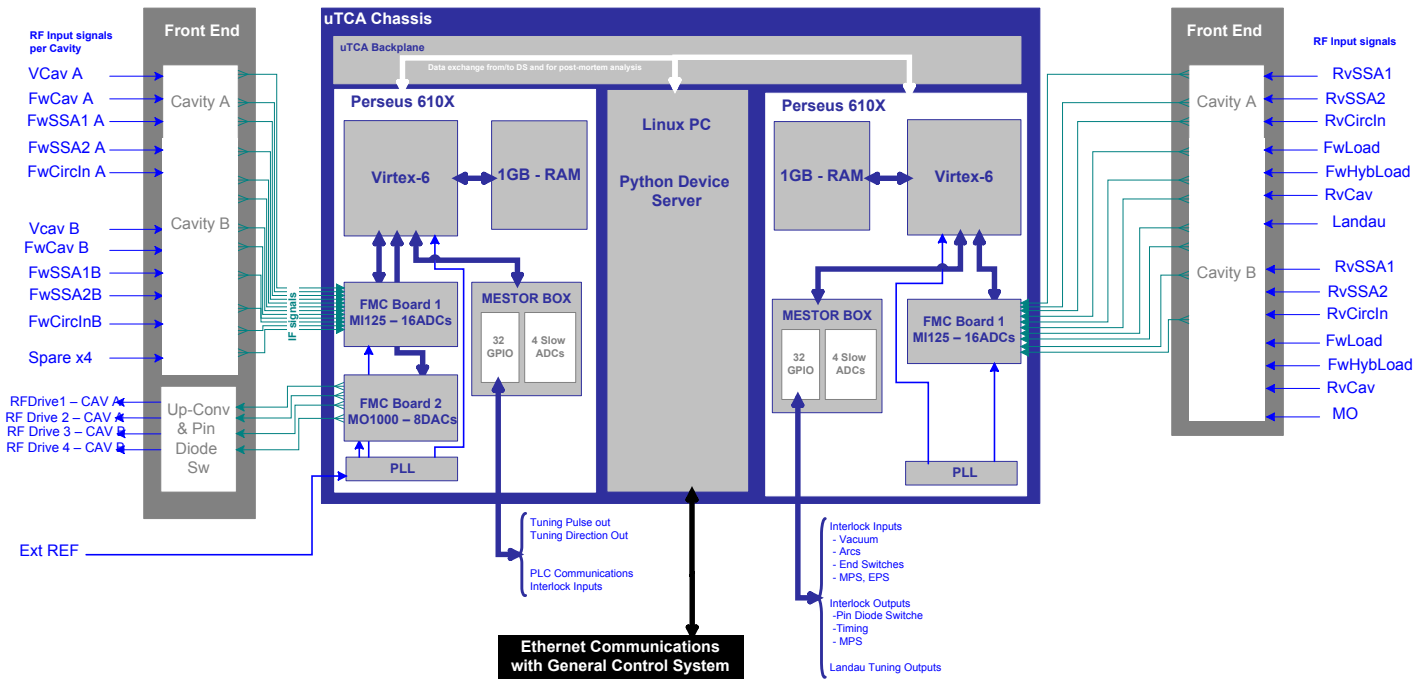

Figure 56: uTCA LLRF HW for Max-IV and Solaris.

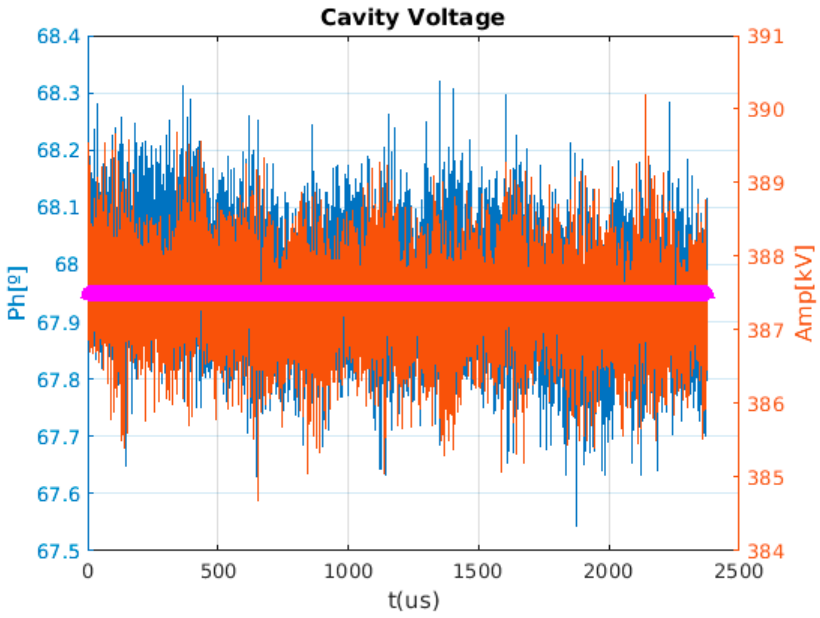

Figure 57: Loops resolution: 0.14% rms and 0.08° rms.

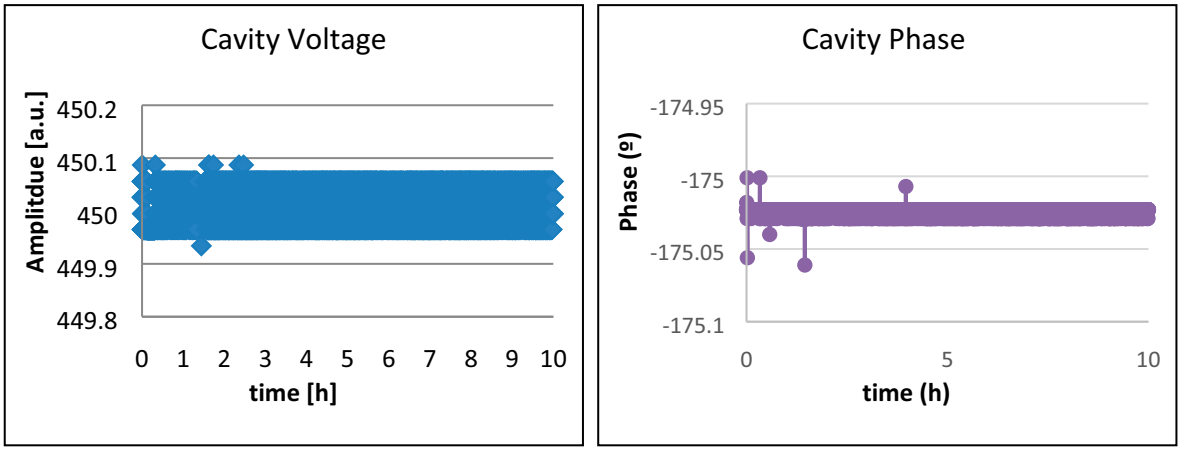

Figure 58: Long-term stability of the amplitude and phase of LLRF loops (10 h).

CONTRIBUTIONS

Angela Salom took responsibility for the project and developed the main features of the DLLRF: analogue electronics, control loops and extra utilities of the system. Francis Perez defined the specifications of the project and supervised its evolution. RF Group Members (Beatriz Bravo, Jesus Ocampo, Pol Solans, Roger Fos, Francisco Sanchez, Michel Langlois) contributed to the commissioning, start-up and development of new utilities of the LLRF. Manolo Broseta, Sergi Blanch and Antonio Milan implemented the Tango device server and graphical user interface. ALBA Electronics technicians and operators (Joan Pages, Xavi Fariñas, Marc Alvarez, Emilio Morales) assembled and tested the analogue electronics crates of the system. Maxlab, Solaris, Diamond and Sirius engineers (Lars Malmgren, Robert Lindvall, Alexsander Mitrovic, Pawel Boroviec, Isa Uzun, Pengda Gu, Chris Christou, Ruy Farias, Andrea Pontes) assembled and commissioned the HW LLRF electronics for their machines following ALBA LLRF specifications and design. Diamond control engineers (Isa Uzun, Paul Hamadyk, Glenn Christian) developed the IOC server of the LLRF in EPICS. Many people have contributed to this project over the years with their ideas, support and help. Thanks to all of them.

OTHER REFERENCES

[1] MOPTY042 - A.Salom et al, Proceedings of the IPAC'2015 Conference, Richmond (USA), 2015
[2] THOAA1 - A. Salom et al, Proceedings of the IPAC'2017 Conference, Copenhagen (DK), 2017
[3] THPAB152, P. Gu et al, Proceedings of the IPAC'2017 Conference, Copenhagen (DK), 2017
[4] THPAB135, A. Salom et al, Proceedings of the IPAC'2017 Conference, Copenhagen (DK), 2017

The ALBA helium liquefaction plant

Montse Prieto, Yury Nikitin, Carles Colldelram, Joan Casas

At ALBA, four of the eight operational beamlines are equipped with devices or performing experiments that require liquid-helium (LHe) cryogenic temperatures. These can be cryostats with superconducting magnets or experimental techniques that require samples at these liquid-helium cryogenic temperatures; BOREAS (BL 29), the resonant absorption and scattering beamline, being the main consumer. Besides, the ALBA storage ring also has one superconducting wiggler that uses helium. The standard liquid helium consumption at ALBA is about 650 l/week which is, for instance, more than 3 times the weekly helium required by a hospital MRI (Magnetic Resonance Imaging) scanner. This makes ALBA one of the major consumers of LHe in Catalonia.

Before the construction of this new liquefaction plant, all the liquid helium consumed was evaporated and released into the atmosphere. This means the He gas could not be recycled and was thus purchased periodically as a consumable. But the helium market is quite unstable and the price has been rising for years as a result of the dwindling helium natural reserves. As a consequence, the cost of this consumable tends to become unsustainable, raising the prospect of a future scenario where the construction and exploitation of its own plant becomes more profitable and worthy. Thanks to a collaboration agreement with the Catalan Institute of Nanoscience and Nanotechnology (ICN2), both institutions decided to install at ALBA's premises the equipment already acquired by the ICN2 and exploit it for the benefit of both institutions.

The plant was installed in a new dedicated building next to the perimeter laboratories at ALBA's site. Figure 59 shows the plant highlighted in colours including the experimental corridor recovery ring (blue) constructed to reach all potential consumption points.

This allows recovering the gaseous helium, to re-liquefy it and reuse it. The liquefaction plant, which is one of the few facilities of its kind in Catalonia, not only will produce cost savings of about 77% but will also reduce market dependence.

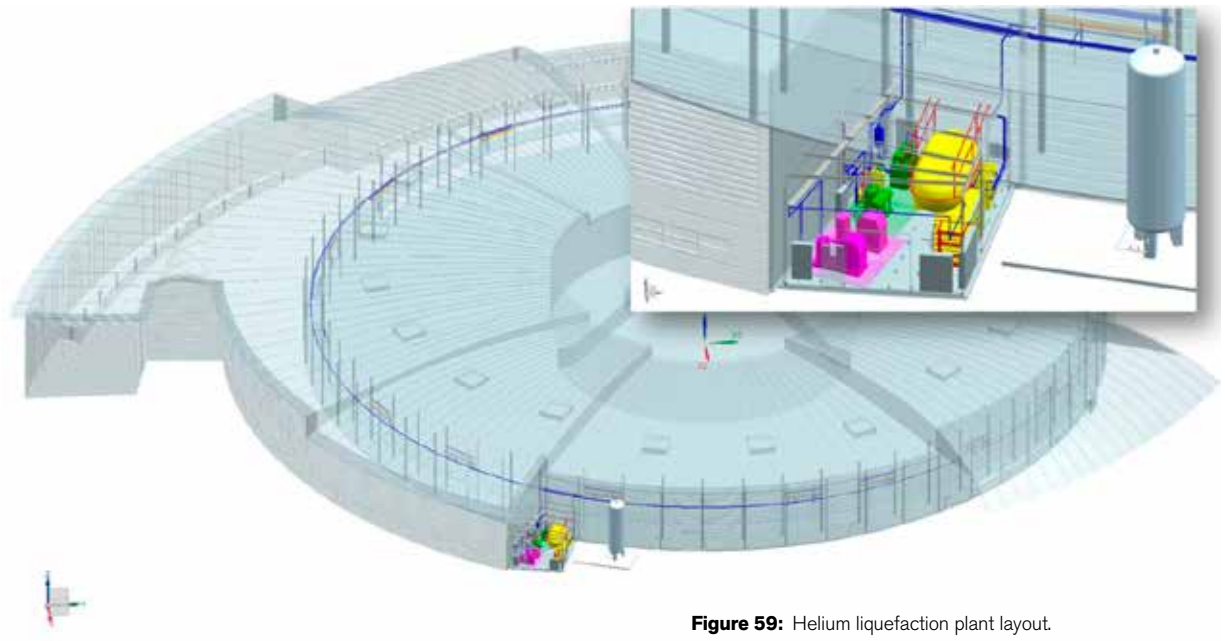

Figure 59: Helium liquefaction plant layout.

Figure 60: The helium liquefaction plant.

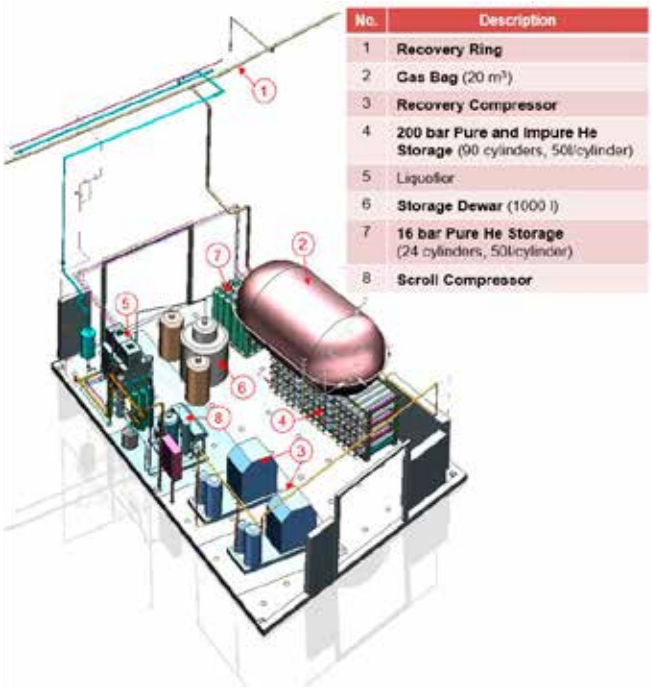

Figure 61: Helium liquefaction plant equipment identification.

The plant is composed of three main subsystems: recuperation, purification and liquefaction.

In order to reach all consumption points at the ALBA Experimental Hall, where the beamlines are located, a big 400 m perimeter stainless steel ring has been constructed. The ring has a big diameter in order to minimize the pressure drop and not bother consumers with back pressure increase. Special care has been taken to minimize elements and connections, so it has been welded as a continuous pipe surrounding the entire hall along the roof of the first stage perimeter corridor. This is where all the rest of the mechanical installations distribute supplies also with rings, and nineteen inlet connections have been included at the supply panels to reach all possible beamlines.

The recuperation starts when the vaporized helium, which results from the thermal exchange between liquid helium and the beamlines' components being cooled, is slightly heated, evaporated and exhausted through this 400 m perimeter recovery ring that leads the impure gaseous helium to a 20 m^3 atmospheric pressure gas storage balloon already located at the plant (see Figure 61). The balloon acts as a buffer, absorbing the recovery ring oscillations. The helium stored in the gas bag is compressed up to 200 bar by a recovery compressor. The resulting 200 bar helium is kept in this 200 bar impure helium storage (see Fig. 61), which is the last phase of the recovery system.

The liquefaction process requires high gas purity. Prior to liquefying this gas, it must be purified, and this is done by a liquefier's internal purifier. Once the 200 bar storage contains a reasonable amount of impure helium, the purification starts. The plant also includes two bundles of 16 bar already-purified Helium gas used to start up the liquefier.

The liquefier is composed of two expander piston devices which work in tandem with a scroll compressor to liquefy the helium. The liquefier requires to be cooled down before starting the liquefaction in steady state; for this purpose and by means of the already purified 16 bar helium gas, the system starts with a closed loop compression and expansion cycle and continues until it reaches the working temperature, when the plant starts the liquefaction of the recovered helium now stored at the 200 bar storage. This is shown Fig. 62.

As it is shown in Fig. 63, the sucked 200 bar impure helium is led to the liquefier's internal purifier so as to remove its impurities. Then, the purified helium undergoes the different expansions that take place inside the liquefier and gets colder. The cold pure helium eventually is subjected to a final expansion that takes place inside the Joule-Thomson (J-T) valve, where the gas cools below -268.93ºC, that is to say, 4,2K. The resulting liquid/gas mixture flows through the 1000 l storage Dewar, but the gaseous portion comes back into the liquefier so as to be cooled and liquefied.

Taking into account that the plant's liquid production is about 24 l/h, the strategy plan is to store the recovered gaseous helium in the 200 bar impure helium storage for two weeks. After that, 3 days will be

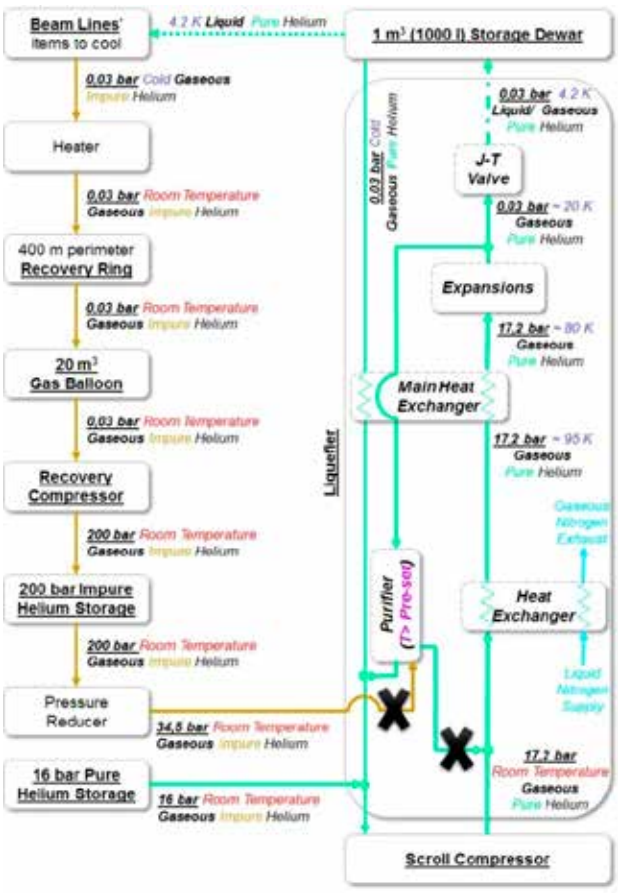

Figure 62: Plant's Flow Diagram when Liquefier's Internal Purifier is not cooled below pre-set temperatures.

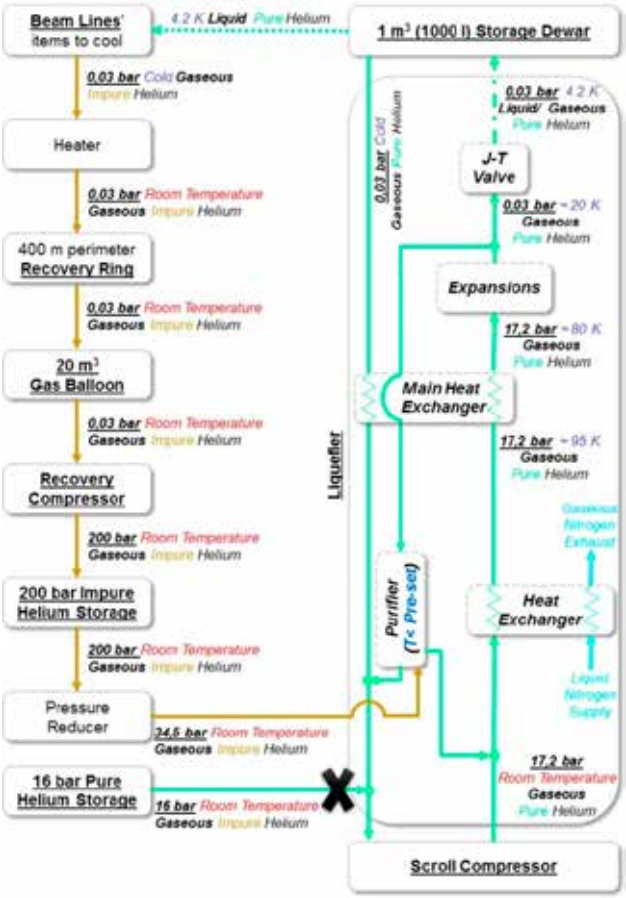

Figure 63: Plant's Flow Diagram when Liquefier's Internal Purifier is cooled below pre-set temperatures.

spent to liquefy helium so as to ensure the beamlines' liquid helium demand for the following weeks.

The detailed execution project of the plant has been done completely in-house, as well as the purchasing of a part of the installation components and the legalization of the involved pressure equipment. Qualified technicians of ALBA's workshop have taken charge of the plant's installation, all the piping and routing and the long stainless steel recovery ring. The plant now is ready to start operation in a regular mode.

CONTRIBUTIONS

Authors appreciate the technical advice and support as well as the superb installation task to ALBA's workshop chief, José Ferrer, and two members of his crew: Paco Trujillo and Jordi Navarro. An example of their outstanding work is the 400m perimeter ring, which has about 100 weld beads. In addition, authors want to express their gratitude to Jordi Iglesias, Pau Jiménez and José María Molina de la Fuente for their contribution to meet and implement in a really short time a quick functional solution for the scroll compressor cooling. Last but not least, Lluís Ginés and David Calderón are acknowledged for their time spent in leak detection.

With the collaboration of

ICN2 Institut Català de Nanociència i Nanotecnologia

EXCELENCIA SEVERO OCHOA

The challenges of instrumentation and control system standards, development and maintenance

Guifré Cuní, Óscar Matilla, Toni Pérez, Daniel Salvat, David Fernández

State-of-the-art scientific facilities explore the frontiers of knowledge and cutting-edge technologies. However, facilities like the ALBA Synchrotron are funded with limited budgets, hence installation and maintenance costs are key requirements and constraints for the lifetime of the project. Continuously improving the service and seeking maximal performance while minimizing installation and maintenance costs are critical success factors. ALBA design strategies focus on the quality, performance and excellence of the experiments and results, goals that are definitely dependent on the robustness and cost-efficiency of procedures and the maintenance of control systems. In this sense, the provision of support services to the operation faces a number of challenges represented in Figure 64.

In this context, standardization is a key factor leveraging the total cost of ownership, the maintenance costs and the performance of specific instruments. The effectiveness of standardization is difficult to measure, and perhaps a comparison with other similar institutes would be a more suitable metrics. The ALBA control system standardized operating systems, input/output controller (IOC) chassis, programmable logic controllers (PLCs), communication middleware, graphical interfaces, programming languages, version control systems for software development, repositories, configuration databases, etc. However, standards are not the solution for everything and can be counterproductive if not adapted to the environment, in the sense that they must control but not forbid exceptions. These exceptions occasionally allow a much simpler and more cost-effective solution at the expense of creating some extra workload in managing extra processes or maintaining stocks.

One of the most critical success factors of a standardization process is taking the example and the lessons learned from other similar facilities before carving standards on stone.

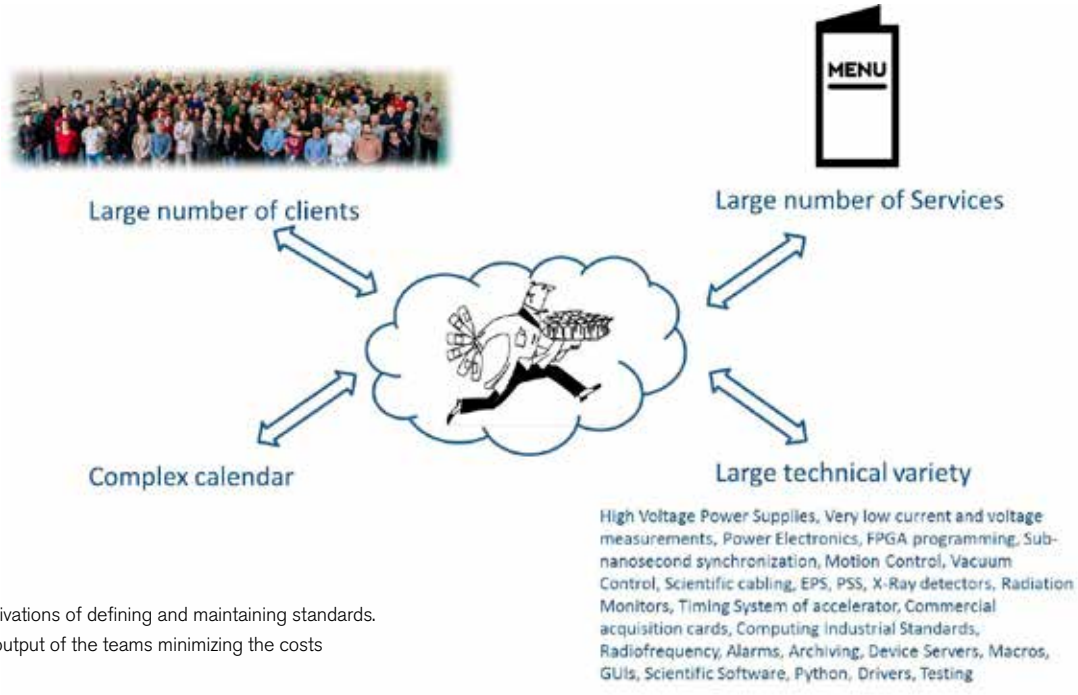

Figure 64: Motivations of defining and maintaining standards. Maximizing the output of the teams minimizing the costs

This can be tackled from different perspectives. We contemplate two approaches in the following paragraphs: (1) the technical standards and (2) the organizational standards.

Technical standards

ALBA software and hardware groups defined a number of instrumentation and control system standards after studying the examples of other installations and taking advantage of the critical lessons learned. A few examples follow:

(1) Operating systems (OS): ALBA relies on Linux distributions with no real-time extensions. The operation from the OS infrastructure perspective started in 2009 with OpenSuse 11.1, the first "evergreen" distribution with extended support, and lasted extraordinarily long until 2018, when it is going to be gradually replaced. This standard platform was deployed in about 95% of the computers. Nevertheless, having exceptions -the remaining 5% of Windows OS- on a multiplatform control system, proved to be more cost-effective and practical than imposing the standard in all cases. And on the contrary there are applications running the standard Linux kernel[1] that reach remarkably high performance and keep all the advantages of the maintenance convenience, like the fast-orbit feedback of the storage ring, running on 4-core CPU and executing the algorithms at deterministic 5 kHz.

(2) The control system; TANGO, Sardana, Taurus: ALBA joined the TANGO collaboration in 2005 and has greatly contributed to the development of the system, going a step further and creating Sardana and Taurus to build integrated supervision control and data acquisition (SCADA) systems for beamlines and accelerators. Sardana and Taurus, started and led by ALBA, are free and open source and, since 2013, international collaborations with the official participation of other three light sources: DESY, MAX-IV and Solaris, and with an increasing group of users including several tens of laboratories and private companies from all around the world.

(3) Input/output controller (IOC) chassis: In 2007 ALBA standardized the compact PCI and industrial PC platforms, which are currently in operation. The VME option was discarded for being at the end of life, considerably more expensive and less performing. ADLINK, with 16-bit 4-channel 500 kHz simultaneous ADCs (ADLINK2005), 2 MHz simultaneous (ADLINK2010), multiplexed ADCs, digital-to-analogue converters (DACs) are examples of standard data acquisition cards on these IOCs. Nowadays, eleven years after these choices, they are still valid and suitable, although there are other solutions. A new synchrotron probably would consider TCA[2] technologies, but with a clear focus on minimizing the number of high-performance and expensive IOCs chassis in the field, and making extensive use of virtualized machines in a central data center and Internet Of Things technologies.

(4) Programmable logic controllers (PLCs): The personnel protection system (PPS) is based on PILZ Safety PLCs and follows very specific constrains normalized in IEC-61508. ALBA was one of the first synchrotrons to adopt the Safety PLC technology for the PSS of the whole installation, which has now become the preferred choice because of the flexibility and simplicity of the installation and reduced costs. The Equipment Protection System (EPS) standardized B&R hardware with more than 60 PLC CPUs and more than 120 remote peripheries distributed in the field. Beamlines have their own system based on the same technology, making it easier to maintain procedures, functions and stocks. It is important to note that the standard leaves room for exceptions with other manufacturers like Siemens, Allen-Bradley or Phoenix Contact, often imposed by turn-key systems such as the linac, high voltage power supplies, radiofrequency systems, etc.

(5) Ethernet is the main communication channel for corporative networks, supervision, control and data acquisition at all levels, including also fieldbuses. Standardizing Ethernet makes the installation more efficient, and easier to maintain. Field devices like diagnostic cameras, oscilloscopes, power supplies, motor controllers, etc. are connected to the Ethernet. There are nevertheless a few cases where the standard would mean a higher cost or a lower performance and so exceptions needed to be made, like the case of Ethernet-PowerLink, installed on specific hardware, that connects the CPUs of the EPS PLCs, ensuring deterministic cycle times of a few milliseconds depending on the application.

1 The kernel has been compiled with a few extra flags to ensure preemption and the system runs in 16 4-core CPUs

2 High-end, high-performance chassis with a large bandwidth and low latencies.

(6) Motor controllers: Beamline experiments rely on several tens of motorized axes. A standardized motor control system, that allows synchronizing the movement of various motors, sending/receiving hardware signals based on position and managing complex trajectories of different axes in the beamline, is today a great competitive advantage. ALBA standardized the IcePAP, initially developed at the ESRF and later converted into a collaboration between several institutes. At ALBA, more than 95% of the axes, including insertion devices, are controlled by IcePAPs.

(7) Corporative equipment and cabling database: The development of a database for the installation equipment, cabling, instrumentation, electronics hardware and infrastructures has proven to be a major competitive advantage, centralizing and controlling the documentation, extremely convenient for managing calls for tenders and maintenance procedures and also for keeping the hardware infrastructure documented and up to date.

(8) In-house developed instruments: In few cases, when the instrumentation available in the market does not fulfill the requirements given by the experiments, a project must be defined, considered and eventually executed. That was the IcePAP case at the ESRF aforementioned and the Em# electrometer developed at ALBA, which, in response to other facilities' interest, was subsequently also converted into an international collaboration. The Em# is capable of femtoampere measurements and lists other features like data rates and triggering capabilities not available in any equivalent in the market. The Em# is today installed at MAX-IV beamlines as well, with an increasing interest by other beamlines from several facilities around the world.

This is not an exhaustive list, and it is not over. There are many standards to consider when undertaking a project of the magnitude of building a large scientific installation that will be at the forefront of scientific research and at the level of the top facilities in the world for the following thirty years (Fig. 65). New requirements, needs and technologies may lead to additional standards at any time. This is the case of piezoelectric actuators, present in most beamlines and widespread in new designs, which could be of a great complexity and, if not addressed correctly, a traumatic experience when it comes to maintenance. The piezoelectric actuator standard is currently being addressed considering several scenarios and use cases, such as in vacuum, with challenging constraints in terms of power dissipation; hysteresis and closed loop systems; free stroke of the actuator and maximum operating frequencies.

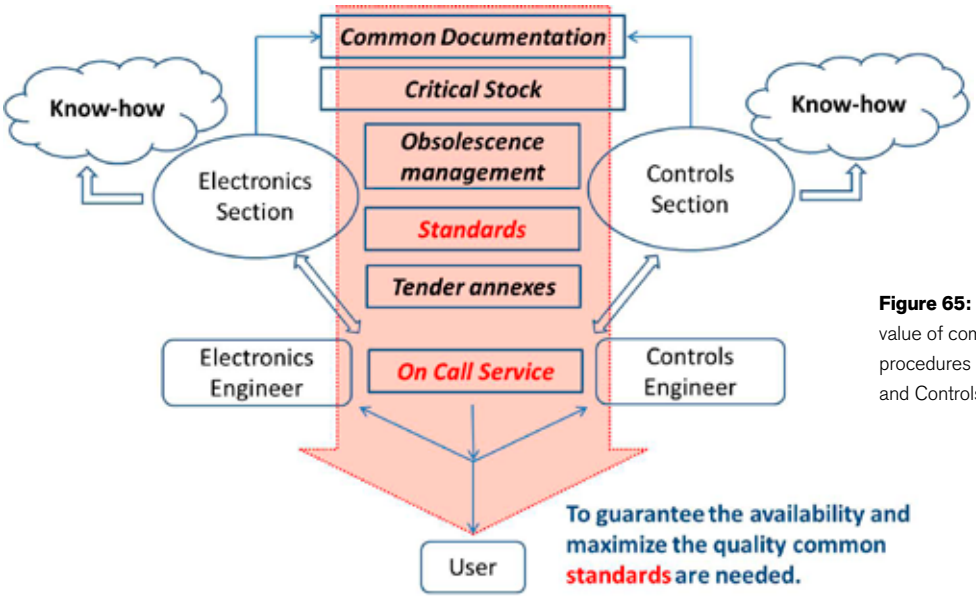

Figure 65: Illustration of the added value of common standards and procedures managed by the Electronics and Controls System sections.

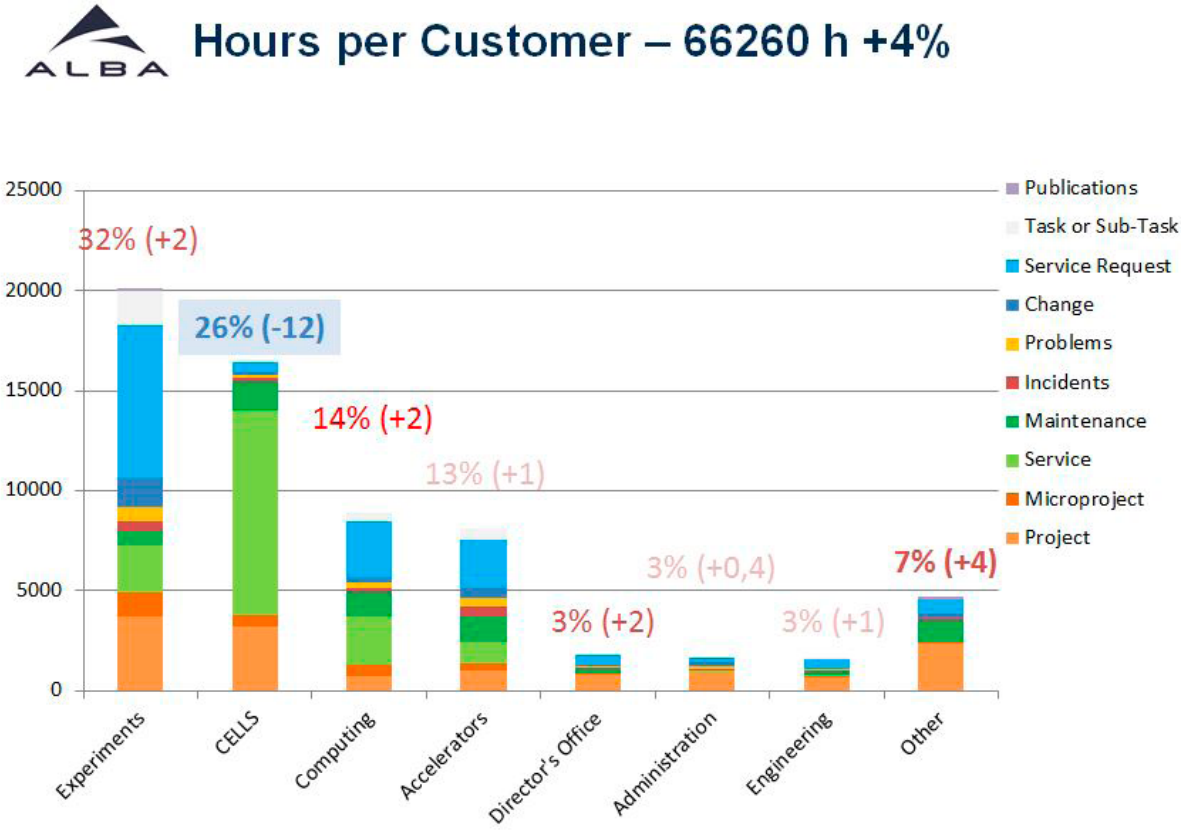

Figure 66: Report of the hours spent per customer, one of the multiple queries possible from the TimeDB.

Organizational standards

The installation and commissioning of the instrumentation and control systems are carried out by the same teams that ensure their maintenance and provide the services that support their operation and guarantee an optimum performance. The electronics instrumentation and controls software teams are coordinated and share efforts in both service design and service operation. They work in close collaboration with the IT system administration teams, essential to the control systems, as well as with the management information systems section to develop the suitable software tools to coordinate efforts and provide an optimum service level. One related example is the corporate equipment and cabling database, developed in-house and extensively used by the whole facility and in particular by all computing division teams. This central repository keeps the documentation of the instrumentation centralized and updated, assisting both electronics and controls engineers to accomplish projects and provide services (Figure 66).

Teams need to be tightly coordinated for an efficient service provision during the operation of particle accelerators and beamlines, and at the same time undertaking projects in the framework of a continuous service improvement. ITIL best practices for service management rely on the Prince2 project management methodology for the design of new services and the implementation of new features. Prince2 is combined with the Agile paradigms, in particular Scrum, for managing sprints and daily tasks. These best practices, implemented as processes, are assisted by software tools such as the Jira software, service desks and Confluence spaces to manage the documentation. Another application that is worth mentioning is the in-house developed TimeDB, that gathers work logs and

time records from different sources and for all team members. The time records are crucial to follow up projects and services, to present reports to clients and stakeholders, and after all to get feedback on the correctness of the plans and on the accuracy of the estimation of efforts and workloads. Figure 66 shows the time devoted to different customers, an example of one of the many reports generated from the TimeDB.

Conclusions

The standardization strategy was designed at the beginning of the project, aiming to make the hardware and software affordable, and to limit the proliferation of redundant types of instruments and software utilities, facilitating the installation at the construction phase, spreading the knowledge efficiently across the organization to the members of the teams, and in summary making affordable a first-rate service level for the support of the operation of a large scientific installation.

CONTRIBUTIONS

Creating, maintaining and updating standards is not a task of a single person but rather the outcome of the collaboration and commitment of the whole team. Every single team member gives continuous feedback, produces the required documentation, and works on the long term cost-effective standards limiting the short-term solutions that can easily turn into long-term problems.

This article has been written by David Fernández (Computing Division Head) with the support of Guifré Cuní (Controls Section Head), Óscar Matilla (Electronics Section Head), Toni Pérez (IT Systems Section Head) and Dani Salvat (MIS Systems Section Head). They are all writing on behalf of the Computing Division composed of more than 50 people responsible for the work described here.

2017 IN ALBA

FEBRUARY

ALBA expands its research portfolio with the NOTOS beamline

This will be the 11th beamline and will be devoted to X-ray absorption and diffraction experiments as well as technology transfer projects. Its design started in 2017 with the aim of being available for users in 2020.

MARCH

ALBA hosts a meeting with European Synchrotrons and FELs Industrial Offices

On 7-8 March, 11 representatives from the Industrial Liaison Offices of European synchrotron and free-electron laser facilities were putting in common ideas and projects within the framework of the LEAPS (League of European Accelerator-based Photon Sources) initiative.

MAY

New record of visitors at the ALBA Open Day

The event, held for the 6th year in a row, gathered 2,194 visitors and more than 100 volunteers in a day for celebrating science. It counted on the support of the Spanish Foundation for Science and Technology (FECYT) and La Caixa Foundation.

MAY

Industrial workshop on agri-food and packaging

Around 70 people attended the industrial workshop organized in collaboration with the EU project NFFA. Companies had the opportunity to discover how synchrotron techniques can enhance the agri-food and packaging sectors.

JUNE

ALBA promotes dual training studies

Twelve dual training students from Catalan schools joined our facility to learn a job while carrying out their training. They spent one year expanding their knowledge in areas such as web applications development, design and production of mechanical manufacturing, administration and finance, laboratory and quality control techniques, refrigeration and air conditioning, electrical maintenance and risk prevention. Since 2014, more than 30 students have benefitted from these grants and 5 have been hired by ALBA afterwards.

AUGUST

Installation of the undulator for the LOREA beamline

During the summer shutdown, the insertion device of the LOREA beamline (an APPLE-II undulator, that covers a long energetic range of operation (10-1000 eV) compatible with a variable polarization mode) was installed.

SEPTEMBER

Condensed matter theory workshop

On 18 September, researchers from ICMAB-CSIC and ICN2 were invited to attend a workshop in ALBA to summarise the ongoing activities in these centres and look for future collaborations.

SEPTEMBER

First ALBA Early-stage Researcher Day

On 22 September, eight students doing their PhD at the ALBA Synchrotron presented the status of their projects in areas such as the application of synchrotron light as well as accelerators development.

OCTOBER

ALBA organises ICALEPCS conference and LLRF workshop

From 8 to 13, more than 600 experts from particle accelerators, synchrotron light and laser facilities or telescopes around the world participated in ICALEPCS held in Barcelona, where they could showcase the latest developments of hardware and software to control large research facilities. One week later, on 13-19, Barcelona was the venue for the Low-Level Radio-Frequency Workshop, also hosted by ALBA.

OCTOBER

VIII AUSE Congress and III ALBA User's Meeting is held in Madrid

On 9-11 October, AUSE and ALBA gathered more than 100 people from the Spanish scientific users' community at the Campus of CSIC, in Madrid, to discuss the most exciting research results, whether obtained at ALBA or other facilities.

NOVEMBER

The LEAPS initiative is launched in Brussels

19 light source facilities across Europe, including ALBA, gathered to launch the League of European Accelerator-based Photon Sources (LEAPS) and signed an agreement to strengthen their collaboration, in the presence of high-level representatives of the European Commission and national governments.

DECEMBER

Promoting gender equality in science and technology

More than 150 high school students from Barcelona visited the ALBA Synchrotron in an event aimed at fighting against gender stereotypes and prejudices linked to research environments. The event was opened by the first Deputy Mayor of Barcelona, Mr. Gerardo Pisarello.

HEALTH AND SAFETY

Continuing with the strategy initiated in previous years, ALBA's new Prevention Plan procedure has been approved in 2017. The effort started to revise the current plan in order to have a new version, better adapted to the intense operation activities and simultaneous process of new beamline construction.

Moreover, two new software tools have been implemented, Confluence and Health & Safety Service Desk. This new software allows to request authorization for hazardous activities, entrance of external companies or training, for instance, or to inform about a new event, an accident, or any situation that can imply an accident or new working conditions.

During this year, the 9th ALBA beamline, LOREA, started its construction. Shielding calculations for this new UV beamline have been performed by the Radiation Protection Service and the results sent to the Nuclear Safety Council (CSN) for evaluation, as part of the documentation to be prepared for the modification of the ALBA radioactive facility. The changes have been approved by our Regulator and the Optics safety hutch has already been installed in our Experimental Hall. Regular survey of radiation safety aspects at ALBA was developed as usual, without any relevant news.

In the area of emergencies, one of the main efforts made during 2017 has been to have an emergency plan approved by the CECAT (*Centre for coordination and information on civil protection in Catalonia*). Team members undergo specific training and participate in ad-hoc organization meetings and drills.

During 2017, several HAZOP (Hazard and Operability) safety risk assessment studies were carried out on new plant designs, such as the helium gas recovery plant or the design of the new sampling facility at CLÆSS.

Team building has been reinforced by means of the attendance to international conferences like ITSF 17 and Radsynch '17.

The follow-up of external contracts has been completed through the New CAE Platform software. This tool permits us to control an enormous amount of legal documents.

A new safety rule for working at height has been implemented, purchasing new equipment in order to reduce risks during these tasks. Regular safety visits have been implemented to detect opportunities for improvement and reinforcement of laboratory standards with those responsible.

In the Biosafety area, special effort has been put on the preparation of the register of all GMO samples received in ALBA during 2017 and its submission to the CCBS (Catalan Commission on Biosafety) for assessment by the CNB (National Commission on Biosafety).

Likewise, all CMR (carcinogenic, mutagenic and reprotoxic) products have been identified and all chemicals reordered according to their compatibility; as part of this, all the material safety datasheets (MSDS) of the products used have been drawn up and made available to internal and external laboratory users.

The Biosafety staff has also begun the procedures to request:
- On one hand, the extension of the authorization to use BSL 1 after the reform (finished after summer), and
- On the other, the authorization of BSL 2 (Mammalian Cell Cultures Room), after its construction (also finished after summer).

Finally a great number of health and safety training activities have been developed. During 2017 about 65 training actions (courses, practical sessions) specifically addressing safety have been carried out (excluding the ad-hoc safety training sessions conducted with each newcomer, student, collaborator or user group). Continuous education and training is seen by ALBA as a key ingredient to improve safety.

By the end of the year, a detailed planning of the activities to be carried out in relation to health and safety during 2018 was elaborated, exposed to the CSS and approved by the director.

International and national collaborations with other facilities and research centres have been present in 2017. Here, we highlight some of them, although other on-going collaborations have also taken place (Elettra Sincrotrone, CIEMAT- IFMIF, SOLARIS, SIRIUS, etc).

INTERNATIONAL ASSOCIATE PARTNER

Institute for Research in Fundamental Sciences (IPM)

The Institute for Research in Fundamental Sciences (IPM, Iran) is the first international associated partner of the ALBA Synchrotron. In 2017 ALBA hosted and trained scientists from Iran with the aim of exchanging knowledge in the area of particle accelerators and synchrotron light applications.

Among the different experiments resulting from this collaboration, it is worth mentioning that scientists from University of Isfahan analysed how were made ancient Iranian glass objects that date back to 2.500 BC. These decorative glass pieces were excavated from the ziggurat of Chogha-Zanbil, a type of stepped pyramidal monument, inscribed on the UNESCO World Heritage List. Scientists determined the chemical composition of these samples at the MSPD beamline in order to know better the glass manufacturing process and reconstruct the technological expertise (know-how) of this ancient civilization.

ONGOING COLLABORATIONS

OPEN SESAME

Project for transferring knowledge to the scientific community emerging around SESAME, the synchrotron facility of the Middle East. The project includes training activities (courses, schools, etc.) and staff exchanges in a wide variety of synchrotron-based topics: accelerators, instrumentation, safety, beamlines, users, outreach, etc.

EuroCirCol

This H2020 project is a conceptual design study for a post-LHC research infrastructure based on an energy-frontier 100 TeV circular hadron collider. ALBA's role is to contribute in managing accelerator developments, organising international events and in the vacuum design.

CLIC-CERN

The Compact Linear Collider (CLIC) study is an international collaboration working on a concept for a machine to collide electrons and positrons (antielectrons) head-on at energies up to several Teraelectronvolts (TeV). ALBA is involved in damping ring technologies, design, prototyping and testing of the final equipment.

ARIES

ARIES is an Integrating Activity project which aims to develop European particle accelerator infrastructures, co-funded under the European Commission's Horizon 2020 Research and Innovation programme. During four years, it will work towards improving the performance, availability and sustainability of particle accelerators, transferring the benefits and applications of accelerator technology to both science and society, and enlarging and integrating the European accelerator community.

LAAAMP grant

Utilization of light source and crystallographic sciences to facilitate the enhancement of knowledge and improve the economic and social conditions in targeter regions of the world, ICSU is a partner with IUPAP and IUCr to enhance advanced light sources (ALS) and crystallographic sciences in Africa, Mexico, the Caribbean, Southeast Asia and the Middle East.

PARTICIPATION IN EUROPEAN PROJECTS IN 2017

As commented previously, ALBA has been involved in different Horizon 2020 projects during 2017. A complete summary list follows.

CODE	OBJECT	COORDINATOR	AWARDED AMOUNT TO CELLS-ALBA €
EUROCIRCOL (654305)	European Circular Energy-Frontier Collider Study	CERN	169.000,00
OPEN SESAME (730943)	Opening Synchrotron Light for Experimental Science and Applications in the Middle East	ESRF	241.318,75
ARIES (730871)	Accelerator Research and Innovation for European Science and Society	CERN	63.000,00
NANOCANCER (748889)	Getting new insights into the radio-sensitization effects of nanoparticles in photon and charged particle therapy	CELLS-ALBA	158.121,60
CALIPSO PLUS (730872)	Convenient Access to LIghtsources OPen to Innovation, Science and to the WOrld	HZDR	394.744,25
DOC-FAM (754397)	Doctoral training programme in Functional Advanced Materials	ICMAB-CSIC	333.900,00

SEMINARS

In 2017, ALBA has been involved in the organisation of 54 events, including a big conference, ICALEPCS 2017. From October 8th to 13th , more than 600 experts from particle accelerators, synchrotron light and laser facilities or telescopes around the world were showcasing in Barcelona the latest developments of hardware and software to control large research facilities. It is also worth mentioning the organisation of the Low Level Radio Frequency Workshop and the VIII AUSE Congress and 3rd ALBA User's Meeting, with more than 100 participants each.

Along the year, ALBA welcomed 28 invited speakers from other synchrotron facilities and research centres. 11 workshops or congresses were organized in the area of accelerators, experiments, computing & control, outreach or industrial applications. 12 internal events were addressed to the ALBA staff, among them the new series of seminars ALBA Talks. Based on a previous series of internal seminars, this new cycle is aimed at sharing knowledge about the activities carried out by the different divisions in the ALBA Synchrotron as well to improve the scientific culture of all the members of the staff.

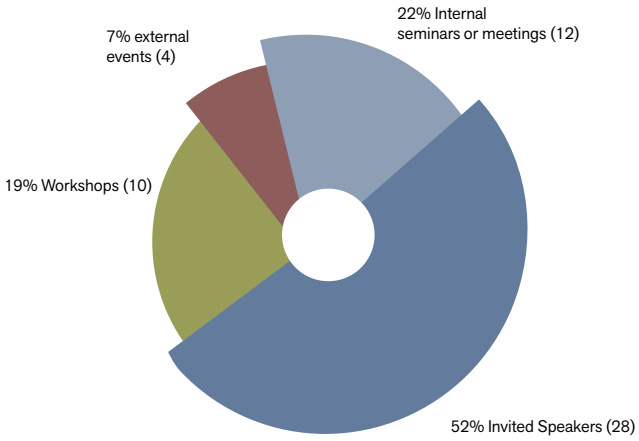

List of workshops, conferences or congresses organised or hosted by ALBA

7/2/2017	F4E Visit & Conference
7-8/3/2017	European Industrial Liaison Offices Meeting
3-4/4/2017	RDA-PanSig Workshop on Interoperability
12/5/2017	Agri-Food and Packaging Synchrotron Industrial Applications
20/5/2017	ALBA Open Day Seminars about particle accelerators - Benefits of synchrotron radiation - How to produce synchrotron light
18/9/2017	Condensed matter theory workshop: overview of ICN2 and ICMAB activities
8-13/10/2017	ICALEPCS 2017
9-11/10/2017	VIII AUSE Congress and the III ALBA User's Meeting
10/10/2017	ALBA Synchrotron Applications to Pharmaceutical, Cosmetics and Biomedical Industries
16-19/10/2017	LLRF 2017 Low Level Radio Frequency Workshop
23/10/2017	Hands-on workshop on Macromolecular Crystallography
23-24/10/2017	ESRF Talks
10-17/11/2017	Specialization Course for High-school Teachers
12/12/2017	STEM Preparades! Science and gender workshops for high school students

Talk of Salvador Ferrer at the ICALEPCS conference.

Opening ceremony of the VIII AUSE Congress and III ALBA User's Meeting.

One of the seminars celebrated in 2017 within the series of ALBA Talks, addressed to staff, students and collaborators.

Check the complete list of events at http://www.albasynchrotron.es/en/media/events

STUDENTS AT ALBA

The ALBA Synchrotron has continued with training activities addressed to students, from undergraduate or vocational training up to PhD candidates.

After launching its Students' Program in 2015, nearly 100 students have widened their knowledge in ALBA's facilities. Internships can last from 3 to 11 months and are applied to many of the activities developed at ALBA, covering areas such as Engineering, Experiments, Accelerators, Health & Safety, Computing and Control, Administration or Communication.

Undergraduate internships

14 university undergraduates were trained in different disciplines in ALBA in 2017: accelerators' technologies, scientific applications of synchrotron light, electronics, computer systems and networks, vacuum technologies, radioprotection service and science communication and outreach.

Vocational training

In 2017, 12 vocational training students have learned a job in ALBA while they have followed their technical studies. They have been trained in areas such as web applications development, design and production of mechanical manufacturing, administration and finance, laboratory and quality control techniques, refrigeration and air conditioning, electrical maintenance and risk prevention.

PhD students

A total of 10 students were doing their PhD at ALBA in 2017: seven in fields related to synchrotron light applications and three in accelerators' technologies. The topics of their projects are the following: radiation effects in molecules, molecular mechanisms involved in plant growth, antibiotic resistance, designing and building a high pressure and temperature cell for the study of cements with synchrotron light, the study of transition metal oxides, the analysis of chemical properties of metal nanoparticles, the development of a solid state amplifier for the 3rd harmonic cavity of the ALBA storage ring, the study of beam induced vacuum effects, the characterization of coated high temperature superconductors (CHTS) and the optimization of remote inductively coupled plasma for cleaning optical surfaces. Half of these projects are in collaboration with other institutions (Wageningen University, University of A Coruña , Institute of Physical Chemistry Rocasolano, Institute of Chemical Technology of the Polytechnic University of Valencia and the company IBSS - which constitued the first industrial PhD done at ALBA-). On Friday 22nd September all the PhD candidates had the opportunity to present their projects in the first Early-Stage Researcher Day celebrated at ALBA.

Teaching activities

Some members of the ALBA Synchrotron also do university teaching activities related to accelerators' physics and scientific applications of synchrotron light: Physics Degree at the Autonomous University of Barcelona (UAB), Master on Nanoscience and Nanotechnology also from the UAB and tutoring final grade projects at the Polytechnic University of Catalonia (UPC).

Participants of the 1st Early-Stage Researcher Day at the ALBA Synchrotron, held on 22nd September 2017.

Vocational training students in their first day at the ALBA Synchrotron.

OUTREACH

In 2017, communication and outreach activities have continued at ALBA, maintaining the most successful programs and initiating new projects, addressed to specific target audiences.

Spreading the word among the general public

The ALBA Open Day has been held once again this year, with the attendance of 2,194 visitors in just one day and the participation of 110 volunteers from the ALBA staff. The event followed a free itinerary where visitors were able to see the devices through which electrons pass or those used for manipulating the synchrotron light, to participate in fun demonstrations to know more about concepts like vacuum or pressure, microscopy or spectroscopy. As a novelty this year, an accelerator mock-up, done with Lego bricks, was very successful among young visitors, as well as the demonstration about infrared, performed with a thermographic camera. This project, together with the series of infographics (see below), was partially funded by the Spanish Foundation for Science and Technology (FECYT) and La Caixa Foundation. The video of the event is available here: https://youtu.be/JaMPCQnQCPs.

The program of guided visits at the facility continued in 2017, receiving 4,775 visitors (47% of them were high school students, 19% university students, 10% researchers (non-users), 11% institutions, 5% cultural and professional associations and 8% private groups).

With the aim of reaching different targets (specially young people), ALBA developed a series of 12 infographics and illustrations to explain its main characteristics and curiosities, using a simple and visual language. This material was distributed through social media during the whole year and it was compiled in a hard-cover book to be offered to high schools and libraries. Infographics are available here in Spanish and Catalan: https://www.albasynchrotron.es/es/divulgacion/recursos-educativos

Stimulating scientific vocations, guaranteeing gender equality and opportunities and avoiding clichés that separate women from scientific and technological environments were the objectives of the *STEMPreparades* project, that counted with the support of the Barcelona city council. It consisted of a series of workshops where women scientists and engineers from ALBA went to the high school classrooms in Barcelona, complemented by a visit where students had the opportunity to know first-hand the job and workplace of the ALBA staff, as well as to do hands-on activities related to synchrotron light.

The ALBA Open Day 2017 was held on 20th May 2017. The event followed an itinerary composed of different areas of exhibition and demonstration, where visitors could stop at their will.

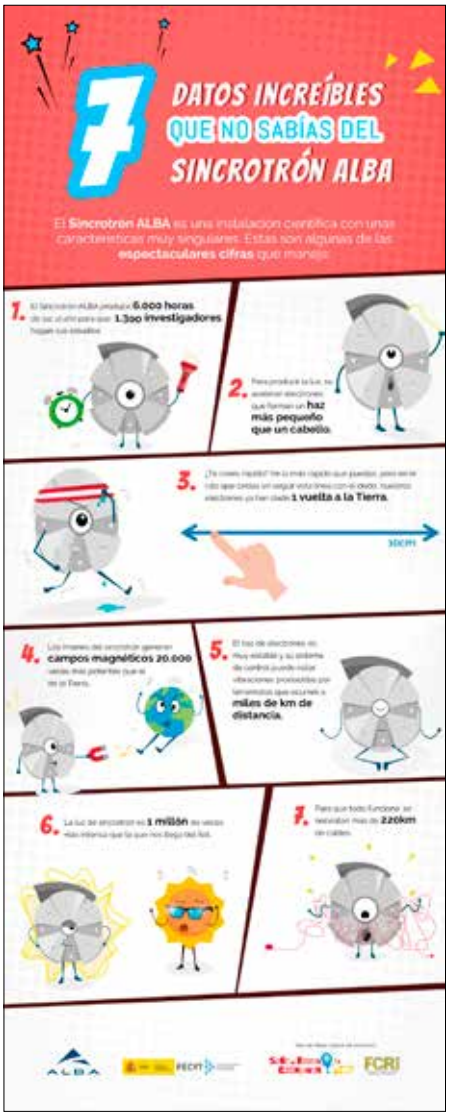

Some of the infographics and illustrations, as well as the book that compiles all of them.

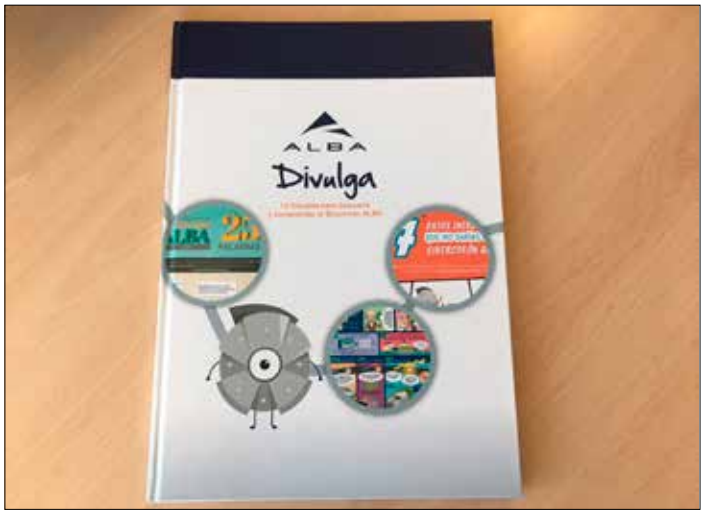

One session developed at different high schools in Barcelona and the final event at ALBA within the STEMPreparades project, aimed at fighting against stereotypes and prejudices linked to research environments.

	2014	2015	2016	2017
Total scheduled beamtime	5092.0 h	5728.0 h	5760.0 h	5912.0 h
Scheduled hours for BLs	3740.0 h	4320.0 h	4368.0 h	4632.0 h
Delivered hours for BLs	3621.2 h	4201.5 h	4261.0 h	4552.0 h
Beam availability	96.8 %	97.3 %	97.6 %	98.3 %
Hours for machine development	1352.0 h	1408.0 h	1392.0 h	1280.0 h
Mean time between failures	33.7 h	51.0 h	58.2 h	96.5 h
Mean time to recovery	1.1 h	1.4 h	1.4 h	1.6 h

MACHINE PERFORMANCE

The ALBA storage ring has run more than 4550 h for users in 2017, out of the maximum of 4632 h foreseen, with a very high beam availability of 98.3%. The storage ring runs on a 24 h a day, 7 days a week basis, for periods that usually are 4 to 5 weeks long. About 1300 h additional time has been dedicated to the optimization of the accelerators for the users as well as to test the new developments of accelerators and beamlines. Figure 67 shows the progression of beam availability since 2012, when users operation started, the dots indicate the mean time between failures (MTBF), which is an indication of the number of beam trips in the machine, the higher the MTBF the lower the number of trips, in 2017 a MTBF of almost 100 h was achieved, i.e. less than a trip every 4 days.

In 2017, the Storage Ring has run at 150 mA until the summer shut down, when the RF upgrade program was completed. Returning from the summer vacation, the storage ring has operated at 200 mA, until a problem with the superconducting wiggler has forced a return to operating with a current of 150 mA.

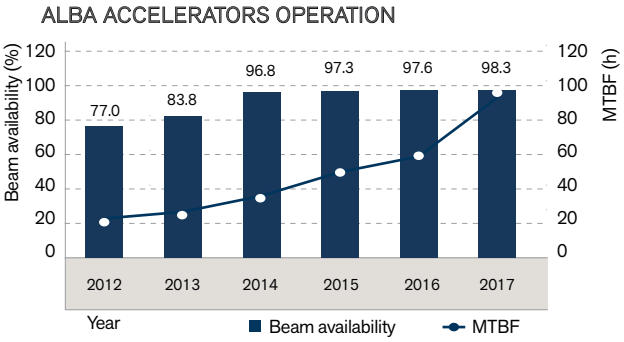

Figure 67: Progression of beam availability and MTBF since the start of users operation.

UNDULATOR AND FRONT END FOR THE LOREA BEAMLINE

The undulator for LOREA, the future 9th beamline of ALBA, has already been installed and undergone a first commissioning campaign with beam [1]. The requirements of the synchrotron light to be delivered to the LOREA beamline were defined to be unique: a wide energetic range of operation (10-

1000 eV) compatible with a variable polarization mode. The polarization switching time was not set as a requirement for the scientific case. Given that a classical APPLE-II design was chosen. The requirement of reaching 10 eV or below leads to a long period undulator (125 mm). One of the drawbacks of this ID is that, because of the highly varying fields produced, the effect on the electron beam dynamics is large, both in terms of tune change and dynamic aperture reduction. Fortunately the second is still larger than the physical aperture, so it should not be a limitation for the injection. However, the first has a strong influence on the whole machine, specially because the dynamic kicks coming from high order harmonics of the ID magnetic field cannot be compensated only by using the usual magic fingers. In order to solve this problem, a dynamic correction scheme has been proposed, based on two thin layers made of copper filaments, placed below and above the vacuum chamber, and fed by independent power supplies. The commissioning of this correction scheme is expected by the end of 2018.

The front end of the LOREA beamline was installed in November 2017. During 2018 the cabling, cooling, vacuum conditioning and commissioning will be finished, and the front end will be ready at the end of 2018 for delivering synchrotron light to the beamline.

Figure 68: APPLE-II undulator for LOREA undergoing magnetic measurements.

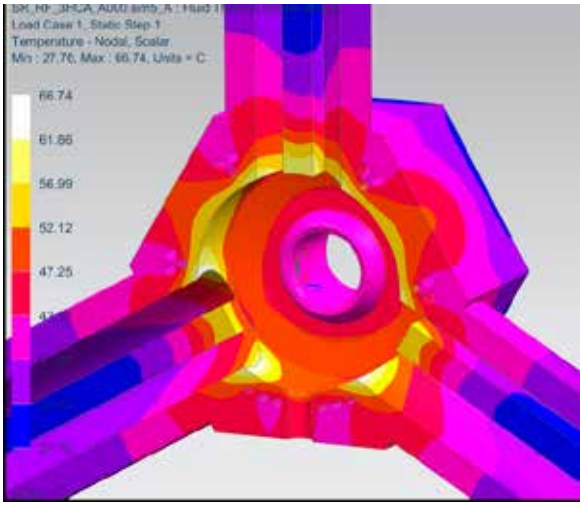

Figure 69: Cavity temperature distribution under nominal working conditions.

1.5 GHz CAVITY DESIGN

In collaboration with the CERN-CLIC project, ALBA has designed a 1.5 GHz HOM damped normal conducting active cavity which could serve as the main RF system for the damping ring of CLIC and as an active third harmonic cavity for the ALBA storage ring [2]. The third harmonic cavity at ALBA will be used to increase the bunch length in order to improve the beam lifetime and increase the threshold for beam instabilities.

The electromagnetic simulations using CST and the detailed mechanical design, including thermal and stress analysis, have been completed. The production of a prototype will start in 2018.

REFERENCES

[1] J.Campmany et al. Proceedings of the IPAC'2017 Conference, Copenhague (Denmark), 2017
[2] B.Bravo et al. Proceedings of the IPAC'2017 Conference, Copenhague (Denmark), 2017

USERS

In 2017 the ALBA Synchrotron has included two allocations periods per year covering the first and second semester. 2017-I call was launched from 4th July to 8th September 2016 and covered the period from January to June 2017 (with the exception of BL13-XALOC which covered the full year, from January to December 2017). 2017-II call was opened from 1st February till 1st March 2017 and covered the period from July to December 2017.

The number of proposals and shifts has been very similar to the previous year. A total of 372 proposals were submitted and 4820 shifts were requested. All the proposals for experiments are peer reviewed. They are evaluated by a panel, composed of international experts from different research areas. As a result of a ranking based on scientific excellence criteria, 225 proposals and 2529 shifts were awarded, representing an oversubscription factor of 1.91.

In 2017, according to the number of proposals and shifts requested, the most demanded beamline was BL24-CIRCE, the photoemission spectroscopy and microscopy beamline. The largest number of granted proposals was for BL04-MSPD, the materials science and powder diffraction beamline. However, the largest number of awarded shifts was also for BL24- CIRCE.

Spanish institutions have been granted 67% of the total beamtime, European institutions represent 30% and there is a 3% of non-European countries, keeping a similar distribution to previous years. The

COMPARISON OF SUBMITTED AND GRANTED PROPOSALS AND SHIFTS

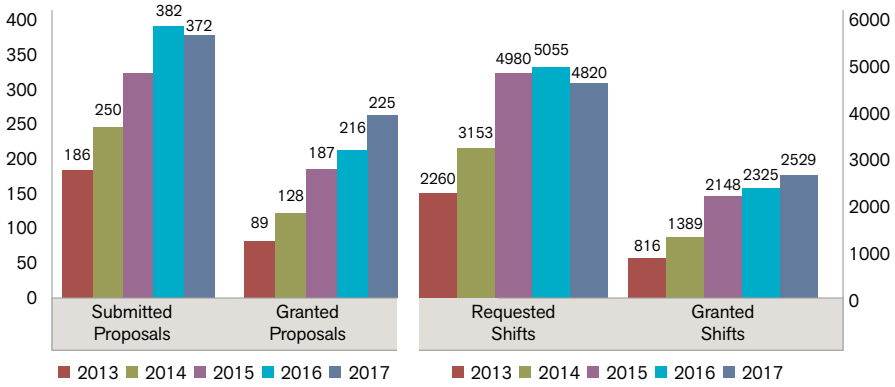

COUNTRY OF ORIGIN OF 2017 PROPOSALS

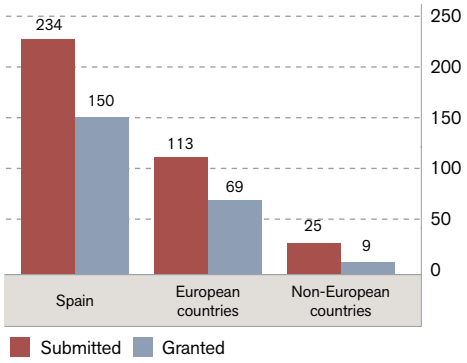

2017 CALL FOR PROPOSALS

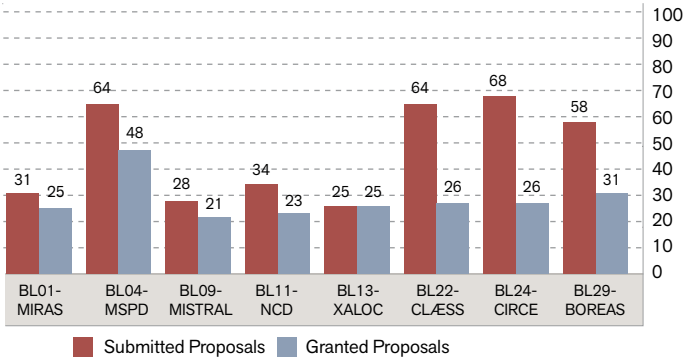

COUNTRY OF ORIGIN OF 2017 SHIFTS

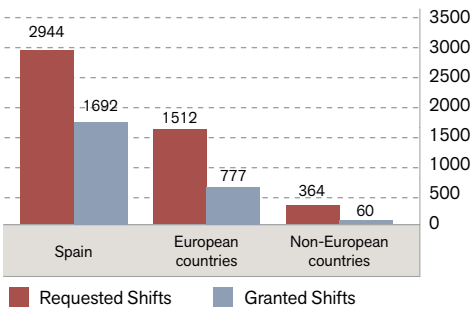

2017 SHIFTS

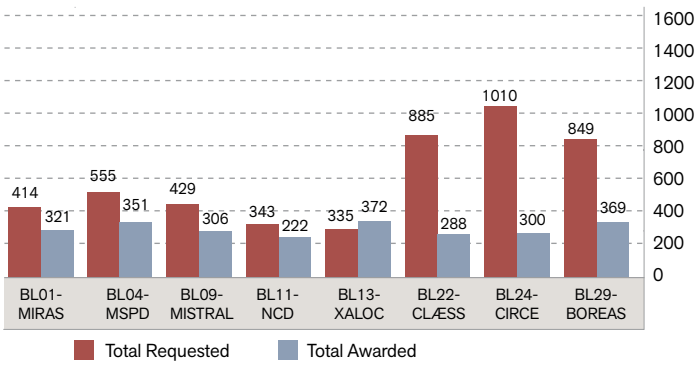

EVOLUTION OF INTERNATIONAL USERS %

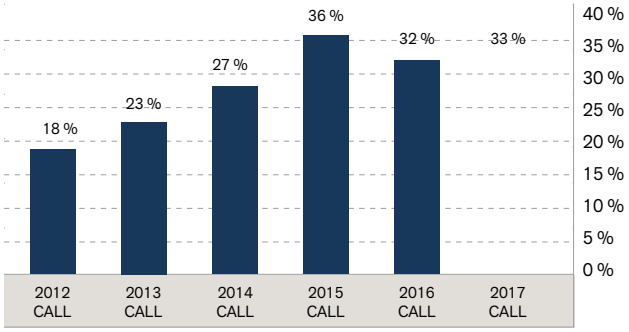

2017 RESEARCH AREAS OF ALL GRANTED SHIFTS

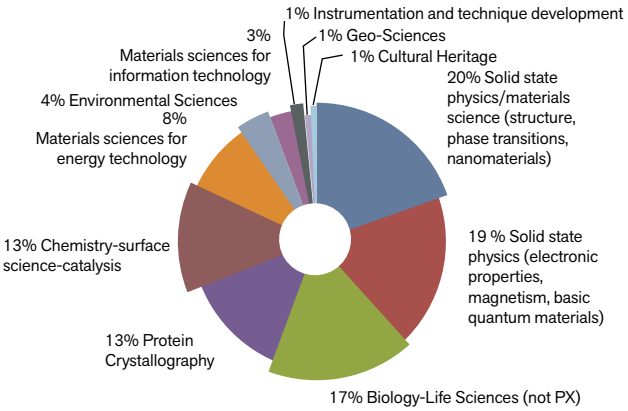

2017 SPANISH GRANTED SHIFTS BY REGION

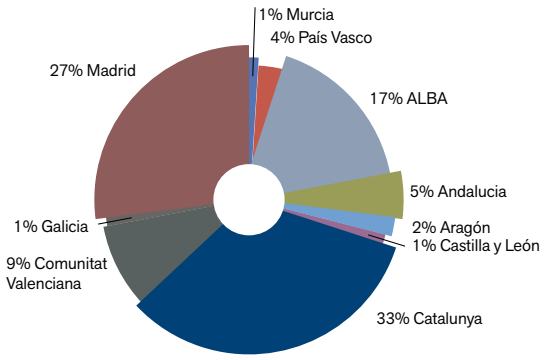

evolution of international users is stable at 33%, instead of continuing its increasing tendency.

BL09-MISTRAL and BL29-BOREAS are the beamlines with more users coming from non-Spanish institutions while BL01-MIRAS and BL13-XALOC are the ones who host more users from Spanish institutions.

Proposals granted to Spanish institutions are distributed as follows: 33% Catalonia, 27% Madrid: 17% ALBA, 9% Comunitat Valenciana, 5% Andalusia, 4% Basque Country and 5% from other regions of Spain.

Regarding the research areas of the granted shifts, 39% belong to Solid State Physics (20% to Materials Science – structure, phase transitions, nanomaterials – and 19% to Electronic properties, Magnetism, Basic Quantum Materials), followed Biology-Life Science (17%), Protein Crystallography (13%), Chemistry-surface science-catalysis (13%), Materials Science for Energy Technology (8%), Environmental Sciences (4%), Materials Science for Information Technology (3%), Cultural Heritage (1%), Geo-Sciences (1%) and Instrumentation and Technique Development (1%).

The number of visits (taking into account experimental visits, not single experiments) in 2017 has continued growing, achieving a total of 533 visits in a year.

EVOLUTION OF NUMBER OF VISITS / EXPERIMENTS

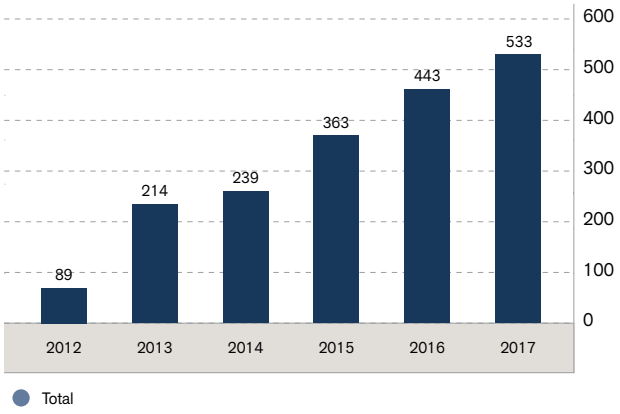

Accordingly, the number of registered home institutions and users in ALBA's database has also increased up to 31% with respect to 2016.

REGISTERED USERS

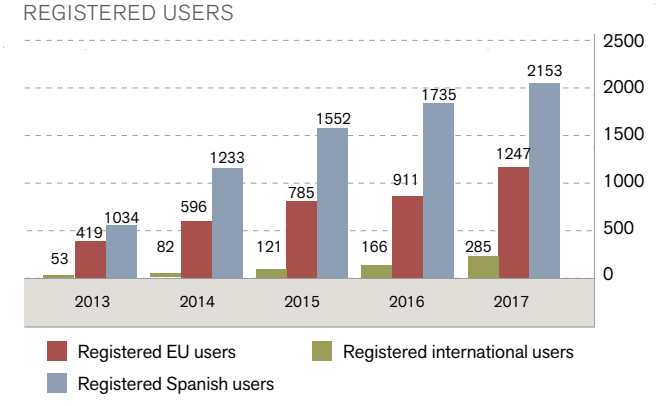

PUBLICATIONS

ALBA contributed to 258 publications in 2017. From these publications, 173 papers were published in peer-reviewed journals, coming from beamtime collected at ALBA (including academic, industrial, in-house and friendly users research). 41 of these publications have an impact factor higher than 7.

* Number of reported publications is constantly being updated. This report includes data that was reviewed on September 2018.

YEARLY EVOLUTION OF PUBLICATIONS

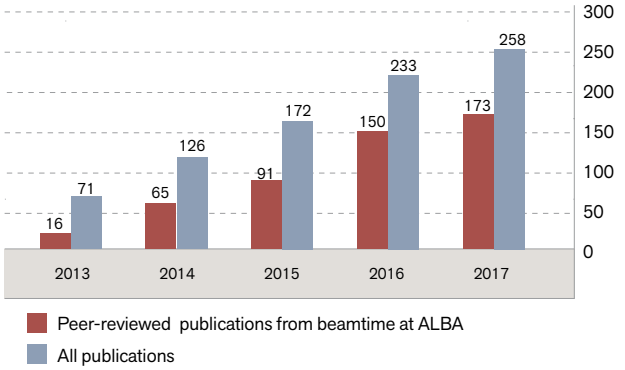

NUMBER OF PUBLICATIONS WITH A HIGH IMPACT FACTOR (I.F. > 7.0)

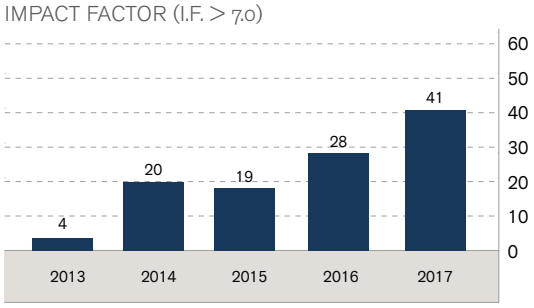

HUMAN RESOURCES

As of 31st December 2017, the staff of the ALBA Synchrotron is composed of 205 members, organized in five different divisions: Accelerators (14%), Administration (7%), Computing & Control (22%), Experiments (32%), and Engineering (17%). In addition, there is a Director's Office (8%), including the following offices: Health & Safety, Industrial Office, Projects and Knowledge Transfer and Communications and Outreach.

34% of ALBA staff are scientists, 30% technologists, 17% technicians, 16% administrative & management staff and 3% health and safety staff.

At ALBA, women represent 25% of ALBA staff. As in previous years, areas like administration or the director's office have more women, while, in technical and scientific divisions, they are underrepresented.

Regarding the nationality of the staff, 78% is Spanish, 19% are from European countries and 3% from foreign countries, with people from Asian, African and American countries.

ALBA STAFF - DISTRIBUTION OF DIVISIONS

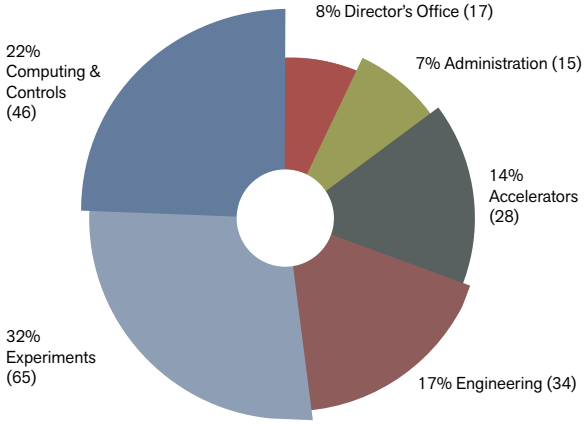

ALBA STAFF - DISTRIBUTION OF CATEGORIES

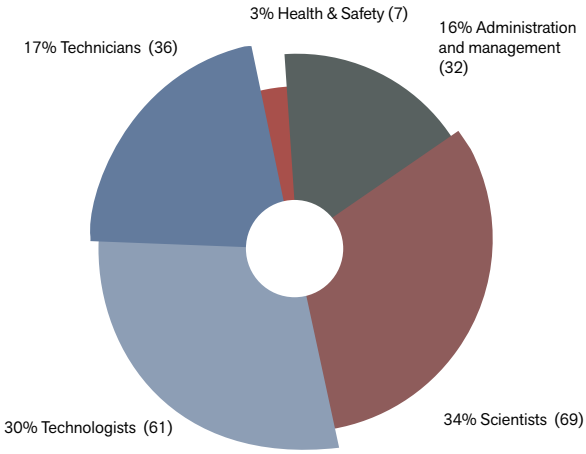

ALBA STAFF - DISTRIBUTION OF NATIONALITIES

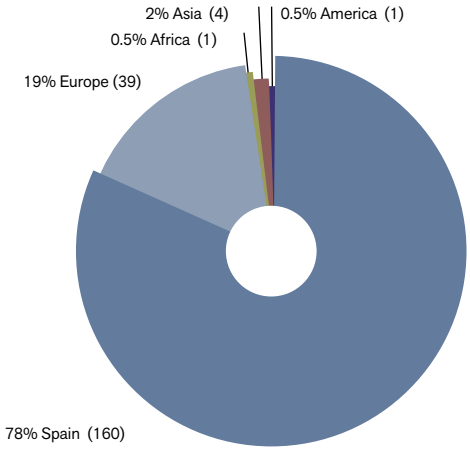

FINANCIAL INFORMATION

INCOME		
Capital funding	19,139,059	90.99%
Service revenue and agreements	866,550	4.12%
National grants	87,400	0.41%
European grants	855,985	4.07%
Other grants	30,000	0.14%
Other income	56,393	0.27%
TOTAL	21,035,387	100.00%
Capital for investments	6,775,863	100.00%
EXPENDITURE		
Staff	10,822,417	52.11%
Equipment and maintenance	1,316,595	6.33%
Facilities	4,333,341	20.87%
Users' support	319,381	1.54%
Student and other grants	47,224	0.23%
Travel and subsistence	270,224	1.30%
Other expenses	1,824,455	8.79%
Replacement investment	1,833,415	8.83%
TOTAL	20,767,054	100.00%
New investments	7,044,196	100.00%